AD-A199 638 ④

The University of Texas at Dallas
Center for Quantum Electronics
The Gamma-Ray Laser Project
Quarterly Report
April–June 1988

^{197}Au

3700 at 2.6 MeV

88 9 30 052

Report GRL/8801

PROOF OF THE FEASIBILITY
OF COHERENT AND INCOHERENT SCHEMES
FOR PUMPING A GAMMA-RAY LASER

Principal Investigator: Carl B. Collins
The University of Texas at Dallas
Center for Quantum Electronics
P. O. Box 830688
Richardson, Texas 75083-0688

July 1988

Quarterly Technical Progress Report
1 April 1988 through 30 June 1988
Contract Number N00014-86-C-2488

This document has been approved
for public release and sale;
its distribution is unlimited.

Prepared for
INNOVATIVE SCIENCE AND TECHNOLOGY DIRECTORATE
OF STRATEGIC DEFENSE INITIATIVE ORGANIZATION

Contracting Officer's Technical Representative
Dr. Paul Kepple, Code 4720
Naval Research Laboratory
4555 Overlook Avenue, SW
Washington, DC 20375-5000

A-1

REPORT DOCUMENTATION PAGE	READ INSTRUCTIONS BEFORE COMPLETING FORM

1. REPORT NUMBER	2 GOVT ACCESSION NO.	3. RECIPIENT'S CATALOG NUMBER
GRL/8801		

4. TITLE (and Subtitle)	5. TYPE OF REPORT & PERIOD COVERED
PROOF OF THE FEASIBILITY OF COHERENT AND INCOHERENT SCHEMES FOR PUMPING A GAMMA-RAY LASER	Quarterly Technical Progress 4/1/88 - 6/30/88
	6. PERFORMING ORG. REPORT NUMBER

7. AUTHOR(s)	8. CONTRACT OR GRANT NUMBER(s)
C. B. Collins	N00014-86-C-2488

9. PERFORMING ORGANIZATION NAME AND ADDRESS	10. PROGRAM ELEMENT, PROJECT, TASK AREA & WORK UNIT NUMBERS
University of Texas at Dallas Center for Quantum Electronics P. O. Box 830688, Richardson, TX 75083-0688	

11. CONTROLLING OFFICE NAME AND ADDRESS	12. REPORT DATE
INNOVATIVE SCIENCE AND TECHNOLOGY DIRECTORATE OF STRATEGIC DEFENSE INITIATIVE ORGANIZATION	July 1988
	13. NUMBER OF PAGES
	118

14. MONITORING AGENCY NAME & ADDRESS(if different from Controlling Office)	15. SECURITY CLASS. (of this report)
Dr. Paul Kepple, Code 4720 Naval Research Laboratory 4555 Overlook Avenue, SW Washington, DC 20375-5000	Unclassified
	15a. DECLASSIFICATION/DOWNGRADING SCHEDULE

16. DISTRIBUTION STATEMENT (of this Report)

This document has been approved for public release and sale; its distribution is unlimited.

17. DISTRIBUTION STATEMENT (of the abstract entered in Block 20, if different from Report)

18. SUPPLEMENTARY NOTES

19. KEY WORDS (Continue on reverse side if necessary and identify by block number)

20. ABSTRACT (Continue on reverse side if necessary and identify by block number)

Recent approaches to the problem of the gamma-ray laser have focused upon upconversion techniques in which metastable nuclei are pumped with long wavelength radiation. At the nuclear level the storage of energy can approach tera-Joules (10^{12}J) per liter for thousands of years. However, any plan to use such a resource for a gamma-ray laser poses problems of a broad interdisciplinary nature requiring the fusion of concepts taken (continued next page)

DD FORM 1473 EDITION OF 1 NOV 65 IS OBSOLETE
1 JAN 73

20. Abstract (continued)

from relatively unrelated fields of physics. Our research group has
described several means through which this energy might be coupled
to the radiation fields with cross sections for stimulated emission that
could reach 10^{-17} cm^2. Such a stimulated release could lead to output
powers as great as 3×10^{21} Watts/liter. Since 1978 we have pursued an
approach for the upconversion of longer wavelength radiation incident
upon isomeric nuclear populations that can avoid many of the difficulties
encountered with traditional concepts of single photon pumping. Recent
experiments have confirmed the general feasibility and have indicated
that a gamma-ray laser is feasible if the right combination of energy levels
and branching ratios exists in some real material. Of the 1886 distin-
guishable nuclear materials, the present state-of-the-art has been ade-
quate to identify 29 first-class candidates, but further evaluation cannot
proceed without remeasurements of nuclear properties with higher precision.
A laser-grade database of nuclear properties does not yet exist, but the
techniques for constructing one have been developed under this contract and
are now being utilized. Resolution of the question of the feasibility of a
gamma-ray laser now rests upon the determination of: 1) the identity of
the best candidate, 2) the threshold level of laser output, and 3) the up-
conversion driver for that material.

This quarter's report focuses upon a variety of new technologies we have
developed to aid in the demonstration of feasibility benefitting from the
strong momentum realized already along the approach to incoherent pumping,
most have continued to advance the development of the nuclear analog of the
ruby laser. A unique type of Compton spectrometer was brought into service
during this reporting period. It was used in a Major Milestone demonstra-
tion that the giant resonances previously used to dump isomeric populations
did consist of individual nuclear structures with discrete excitation
energies. This proves that if the x-ray pump source can be limited in
spectral width the amount of waste heat imparted to the lattice containing
the active nuclei can be greatly reduced. A new analytical study is re-
ported which shows that under these conditions the important Mössbauer
properties can be preserved even at the level of thermal loading necessary
to reach threshold in an ideal material, if the laser host is a thin film
diamond layer. Also reported in this quarter is a major advance in the
technology for preparing such thin films of diamond material and in the
intense x-ray sources needed to pump test quantities.

Possibly, the greatest breakthrough was realized along the more complex
approach of coherent pumping. There it is intended to mix the quantum
properties of long-lived isomeric states with those of freely radiating
nuclear levels. Reported here is the demonstration of large levels of
modulation of the phases of nuclear states with relatively modest input
powers. Now many critical experiments become possible along this secon-
dary path toward a gamma-ray laser.

TABLE OF CONTENTS

PREFACE

This report focuses upon an array of new technologies which have come to fruition during the current reporting period. They make it possible to pursue our fundamental research into the feasibility of a gamma-ray laser with even greater intensity. Benefiting from the scientific momentum already realized along the approach to incoherent pumping, most have continued to advance the nuclear analog of the ruby laser. There have been embodied the very simplest of the concepts for a gamma-ray laser and it is no surprise that the greatest rate of achievement has continued in that direction.

Receiving first emphasis is a unique type of Compton spectrometer which makes it possible to examine the fluorescence yield of nuclei pumped with flash x-rays as a function of the end point energy of the pump spectrum. It was used in a Major Milestone demonstration showing that the giant resonances for dumping isomeric populations, consist of individual nuclear structures having discrete excitation energies. Being discrete, they can be excited with x-ray pump sources of moderately limited bandwidth. This is of paramount importance as it gives the means to control the amount of pump energy degraded to heat in the sensitive layer in which the populations are pumped toward inversion.

Reported here is a new analytic study which shows that under practical conditions the important Mössbauer properties can be preserved when the active nuclei are diluted in a thin film of epitaxical diamond, *even at the level of thermal loading necessary to reach threshold in a reasononable material*. Also reported in this quarter is a major advance we have introduced in the technology for the preparation of the types of thin films of diamond materials that are needed as host lattices; together with the further scaling of a laboratory scaled source of x-rays that can rival synchrotrons in total output.

As has been the case since 1982, there are still no known factors which inhibit the realization of a gamma-ray laser. Neither the level of pump fluence required for laser threshold nor the waste heat to reject present any particular problems in idealized materials. *A gamma-ray laser is feasible if the right combination of energy levels occurs in some real material*. When actually tested, the two poorest of the 29 candidate nuclei did surprisingly well, performing 1,000 to 10,000 times better than expectations. The overriding question in

resolving the feasibility of the nuclear analog to the ruby laser is whether or not one of the better of the 29 has its isomeric level in a position sufficiently near the ideal.

As exciting as has been the progress in the straightforward direction to the pumping of gamma transitions, the most difficult breakthrough was realized along the more complex direction of coherent pumping. Also described in 1982, in that process the intent is to mix the quantum properties of long-lived nuclear states with those able to radiate freely. In this way the metastability of an isomeric state could be "switched off". The critical experiment is to show that some laboratory level of <u>coherent</u> input power can affect the properties of a nuclear level. Reported here is the demonstration that large levels of modulation of the phases of nuclear states can be obtained with relatively modest input powers. Now many critical experiments become possible along this secondary path toward a gamma-ray laser.

Continuing the preparation of this report as an "in-house" journal, this series presents material to reflect the individual contributions of the teams of research faculty and graduate students involved in these phases of the research. In this regard I wish to thank all our staff for their splendid efforts in supporting the preparation of these manuscripts to a rather demanding timetable.

- C. B. Collins
- Director
- Center for Quantum Electronics

THERMAL ECONOMY OF A GAMMA-RAY LASER

by C. B. Collins

One of the most inhibiting factors in the development of a gamma-ray laser has been the heavy load of theoretical dogma[1] which confounds the start of each experiment. Too obvious to warrant proof, these tenents of faith are often believed to frustrate even the more positive modeling we reported[2] in 1982. While sometimes combined in various packagings, the barriers to the realization of a gamma-ray laser are usually purported to be fourfold:

1) The electrons will screen the nuclei so analogs of optical pumping will not work for nuclear states.

2) The absorption widths which nuclei display toward pump photons cannot exceed 1 μeV in any useful cases.

3) The isomeric states which would be the most attractive to pump cannot be dumped by photons because they have angular momenta which are too different from the freely radiating levels.

4) The waste heat associated with any pumping process will lodge in the host lattice and destroy the Mössbauer effect needed for a sharpened cross section for stimulated emission.

The sequence of experimental results we reported in 1987 completely destroyed the first three of these tenents of faith. Achieving a first major milestone, we reported[3] the experimental observation of eleven orders of magnitude of increase in the amount of fluorescence which could be obtained when narrow nuclear levels of ^{79}Br and ^{77}Se were pumped with flash x-rays through broad states able to funnel their populations down to the radiating level. Those results confirmed the existence at the nuclear level of the analogs of the processes of bandwidth funneling which made the first ruby laser possible. Clearly the first barrier had been only an illusion.

The second and third articles of faith were destroyed by our more recent major milestone report of the successful dumping of some of the population of a nuclear isomer, ^{180}Ta^m. Offset by _eight_ quanta of angular momenta from the normal rotational bands, populations of this

1

state were dumped into the freely radiating system of levels through an enormous integrated cross section approaching 10^{-21} cm^2 eV by pumping them with flash x-rays.[4] *This result implies a useful absorption width of about 0.5 eV for the interband transfer of population from isomeric to radiating level systems.* Experimentally, the occurrence of these giant resonances for mixing levels across such great spans of angular momenta was subsequently shown to be a rather common occurrence among nuclides.[5, 6, 7]

At this point we have realized nearly seventeen orders-of-magnitude of increase in feasibility over the pessimistic evaluation[1] from which the current renaissance in this field departed. Present capabilities exceed even the more optimistic projection[2] upon which our project is based. However, the concern for the thermal economy has persisted.

In 1986 we reported a study[8] which showed that the waste heat associated with the pumping of nuclei with flash x-rays presented a manageable problem to the design of a device. However, that work received little attention and even the most recent studies[9] pursued elsewhere admit no domain in parameter space in which a threshold level of inversion could be pumped without the concomitant loss of the recoilless fraction of the output transitions. Of course, without the recoilless fraction the cross section for stimulated emission would be so reduced by broadening as to be impossible to excite.

Perhaps, unrecognized, is the fact that the critical parameter in the thermal economy is the average excess energy, E by which the energies of the dominant nuclear transitions exceeds the K-edge energy of the electrons of the material. In the early stages the waste heat is almost entirely contained in the primary photoelectron population produced either by the pump radiation or by the internal conversion of the various nuclear transitions. To have a hopeless situation one need only to limit studies to the rather few instances in which the kinetic energy, E of the primary photoelectrons is so small that the range of such particles is less than the dimensions of the layer being pumped. Then, they cannot escape and the waste energy will be degraded to heat precisely in the sensitive area in which the population inversion is developed. Just such a failure mode was built into the unfortunate

2

example of the excitation of the 14.4 keV transition of ^{57}Fe in an iron matrix.[9]

It is the purpose of this manuscript to explore the problem of the thermal economy of the ruby-laser analog in systems benefitting from the new discoveries which remove the first three traditional inhibitions to the design of a gamma-ray laser. It will be seen that for a wide margin of material parameters, the problem of the waste heat is readily manageable. As a consequence, the fourth and last of the traditional tenents of dogma is destroyed as a paramount concern. Reduced to the level of an engineering challenge, the solution to the problem of waste heat remains to be tailored to the particular characteristics of the nuclear system finally employed.

Whether or not the initial state to be pumped is isomeric, the principal figure of merit for bandwidth funneling is the partial width for the transfer, $b_a b_o \Gamma$. Constituent parameters are identified in Fig. 1 where it can be seen that the branching ratios b_a and b_o specify the probabilities that a population pumped by absorption into the i-th broad level will decay back into the initial or fluorescent levels, respectively. It is not often that the sum of branching ratios is unity, as channels of decay to other levels are likely. However, the maximum value of partial width for a particular level i occurs when $b_a = b_o = 0.5$.

The actual measurement of partial widths has involved the correlation of fluorescence yields excited by a pulse of x-rays in the scheme of Fig. 1 with those expected from the expression.[4-9]

$$N_f = N_o \sum_i \xi_i \frac{\varphi_i}{A} \qquad , \qquad (1a)$$

where N_o and N_f are the numbers of initial and fluorescent nuclei respectively, (φ_i/A) is the spectral intensity of the pump radiation in keV/keV/cm^2 at the energy E_i of the i-th pump band, and the summation is taken over all of the possible pump bands capable of cascading to the same fluorescence level of interest. The ξ_i is a combination of nuclear parameters including the partial width $b_a b_o \Gamma$ in keV,

3

$$\xi_i = \frac{(\pi b_a b_o \Gamma \sigma_o / 2)_i}{E_i} \quad , \tag{1b}$$

where σ_o is the peak of the Breit-Wigner cross section for the absorption step. The combination of parameters in the numerator of Eq. (1b) is termed the integrated cross section for the transfer of population according to the scheme of Fig. 1.
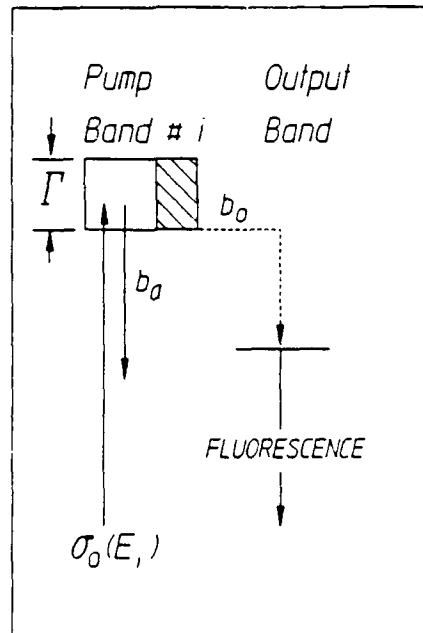
Figure 1: Schematic representation of the decay modes of a gateway state of width Γ sufficiently large to promote bandwidth funneling. The initial state from which population is excited with an absorption cross section σ_o can be either ground or isomeric, in principle.

The Breit-Wigner cross section peaks at

$$\sigma_o = \frac{\lambda^2}{2\pi} \frac{2I_e + 1}{2I_g + 1} \frac{1}{\alpha_p + 1} \quad , \tag{2}$$

where λ is the wavelength in cm of the gamma ray at the resonant energy, E_i; I_e and I_g are the nuclear spins of the excited and initial states.

4

respectively; and α_p is the total internal conversion coefficient for the two-level system comprised by the initial and pump levels. The value of α_p is essentially zero for a transition which is highly allowed; and even were it not, σ_0 would be reduced further and the partial width would become correspondingly larger so that the quantity ξ_i would remain unaffected.

In this development it has been assumed that the width of the pump spectrum is sufficiently greater than Γ that the pump can be considered to be continuous and without structure over the width of the absorption line. Other than this assumption the development, so far, is general. Restrictive assumptions necessary for the management of the thermal economy can be explicitly stated as follows:

1)   The pump band i in Fig. 1 is one of the newly discovered giant pumping resonances with a partial width of $b_a b_0 \Gamma = 1$ eV.

2)   The pump transition is centered on an energy $E_i = 30$ keV.

3)   The initial state is assumed to be isomeric with an excitation energy so high that 2) is possible.

4)   The output transition is around 100 keV.

5)   The nuclei are diluted in a thin film of diamond.

6)   The Borrmann effect contributes a factor of 10 to the enhancement of the ratio of cross sections for resonant to non-resonant transitions.

An immediate issue is the plausibility of these assumptions. While the widths for pumping interband transfer of population to and from isomers have been shown to approach 1 eV in many cases,[4-7] it had not been previously demonstrated that such a width corresponded to a discrete level. Described in the Major Milestone Report for this quarter is the use of a Compton spectrometer to search for a gateway energy, E_i through which the photon pumping reaction, $^{197}Au(\gamma,\gamma')^{197}Au^m$ proceeds. As described elsewhere in this quarterly report the enormous integrated cross section of 3700 in the usual units ($\times 10^{-29}$ cm^2 keV) was found to be localized at an energy 2.6 MeV above the ground state. At

least in this case, the experiment supported the identification of such favorable pumping resonances with a discrete, well-defined pump energy so that Assumption 1) is plausably supported.

Plausibility of the second and third assumptions must be considered together. The range of excitation energies over which isomers can be found is very large, reaching 6 MeV if one considers the shape isomers proposed by Weiss et al.[10] We have already shown that isomers can be dumped into the freely radiating system, even through $\Delta J = 8$, so the only doubt here is a statistical one; whether or not a giant pump resonance can be found within 30 keV of an isomer.

Assumption 4) is quite likely and the feasibility of 5) has been greatly increased by a recent "breakthrough" in the deposition of thin film diamond from laser plasmas. As described in one of the following manuscripts, we have been able to grow very uniform thin films of amorphic diamond from the plasma ablated from a carbon target in an environment especially suited to doping with nuclei of interest to the gamma-ray laser. While proper single crystal substrates have not yet been used to try to organize the growth of single cyrstal diamond, the largest step of fabricating a diamond film has been accomplished. However, until a single lattice is demonstrated the combination of assumptions 5) and 6) remains uncertain. By itself, the anticipation of a factor of ten reduction in the ratio of probabilities for non-resonant to resonant absorption is modest but still questionable for diamond at this time. As a consequence, single crystal Be is also modeled as a second preference. Thus, it can be reasonably asserted that the six assumptions upon which rest the model reported here are plausible and consistent.

Following our development[2] of 1982 under small signal conditions the overall logarithmic amplification, α for a single pass down the length, z of the strip of pumped material shown in Fig. 2, is,

$$\alpha = N_f \sigma_R z - N_o \sigma_{NR}^{(m)} z - N_d \sigma_{NR}^{(d)} z \qquad , \qquad (3)$$

where N_f is the number of nuclei in the fluorescent level which it is desired to pump to threshold, and where σ_R and σ_{NR} denote the cross sections for the resonant emission given by Eq. (2) evaluated at the output wavelength (100 keV) and for the non-resonant absorption in the
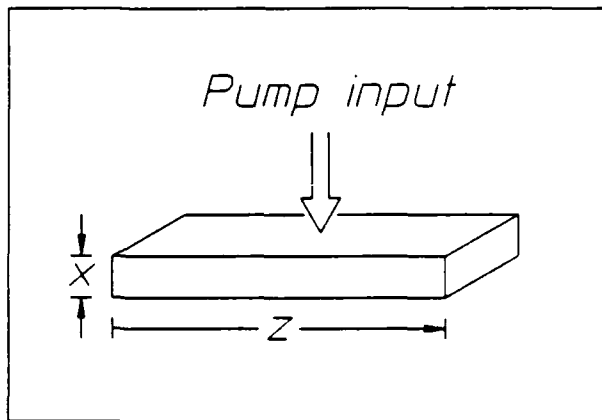
6

Figure 2: *Geometry of the thin strip of diamond doped with the nuclei to be pumped with flash x-rays.*

medium, (m) and diluent, (d), respectively. To reach the threshold for laser output, α must become positive so that the minimal condition is

$$0 \leq N_f \sigma_R z - N_o \sigma_{NR}^{(m)} z - N_d \sigma_{NR}^{(d)} z \qquad , \tag{4}$$

which necessitates,

$$\frac{N_f}{N_o} \geq \frac{\sigma_{NR}^{(m)}}{\sigma_R} \left(1 + \frac{N_d}{N_o} \frac{\sigma_{NR}^{(d)}}{\sigma_{NR}^{(m)}}\right) \qquad . \tag{5}$$

For estimations to within a factor of two the latter term in the parentheses can be neglected for concentrations greater than 3%. At the 100 keV output transition,

$$\sigma_{NR}^{(d)} \text{ (Be)} = 0.13 \text{ cm}^2/\text{gr} \qquad , \tag{6a}$$

$$\sigma_{NR}^{(d)} \text{ (C)} = 0.15 \text{ cm}^2/\text{gr} \qquad , \tag{6b}$$

$$\sigma_{NR}^{(m)} \text{ (Ta)} = 4.3 \text{ cm}^2/\text{gr} \qquad , \tag{6c}$$

where Ta has been arbitrarily selected as representative of the region of nuclides where the better candidates for a gamma-ray laser medium may be found. So it can be seen that at 3% concentration by mass, losses in the diluent increase the right hand side by a factor of 2×.

Simplifying Eq. (5) gives,

$$\frac{N_f}{N_o} \geq \frac{\sigma_{NR}^{(m)}}{\sigma_R} \qquad , \qquad (7)$$

so that the fraction pumped must exceed the ratio of the cross sections for non-resonant loss to resonant stimulated emission. Unfortunately the dependence of the right hand side of Eq. (7) upon nuclear parameters is tedious and structured. Baldwin[1] has presented a convenient review which shows Eq. (7) is optimized for an output energy of 100 keV as assumed here. Values range from 10^{-2} to 10^{-4} and can be assumed to be improved (lowered) by the Borrmann effect. To be consistent with the earlier assumptions, the Borrmann effect is supposed to enhance the mid-range value of 10^{-3} yielding a requirement of 10^{-4} for the pumped fraction,

$$\frac{N_f}{N_o} \geq 10^{-4} \qquad , \qquad (8)$$

This sets the pump intensity needed for threshold, and with it the amount of waste heat to dissipate.

Substituting into Eq. (8) from Eq. (1a) and assuming the single giant resonance dominates so that the sum is unnecessary, gives,

$$\frac{\pi b_a b_o \Gamma \sigma_o F_i}{2} \geq 10^{-4} \qquad , \qquad (9a)$$

where

$$F_i = \frac{\varphi_i}{E_i A} \qquad , \qquad (9b)$$

that is, F_i is the pump flux integrated over the lifetime of the fluorescent level in units of photons/cm^2/eV, if Γ is now in eV. Assuming $I_e = I_g$ in Eq.(2) and $\alpha = 0$, then at 30 keV, $\sigma_o = 2.72 \times 10^{-18}$ cm^2 and letting $\pi b_a b_o \Gamma / 2 = 1$ eV gives

$$F_i \geq 3.7 \times 10^{13} \text{ photons/cm}^2\text{/eV} \qquad , \qquad (10a)$$

or since each photon is 30 keV,

8

$$\Phi_i \geq 177 \ mJ/cm^2/eV \quad . \tag{10b}$$

In the geometry of Fig. 2, it is next important to determine the thickness, x of the pumped layer. At the level of 10% concentration, $N_o = 5.5 \times 10^{21} \ cm^{-3}$ so the extinction coefficient for pumping is,

$$\sigma_o N_o = 1.5 \times 10^4 \ cm^{-1} \quad , \tag{11a}$$

and so,

$$x \simeq (\sigma_o N_o)^{-1} \simeq 0.67 \ \mu m \quad . \tag{11b}$$

At the 30 keV pump energy

$$k_{NR} \ (Be) = 0.332 \ cm^{-1} \quad , \tag{12a}$$

$$k_{NR} \ (diamond) = 0.900 \ cm^{-1} \quad , \tag{12b}$$

$$k_{NR} \ (10\% \ Ta) = 35.4 \ cm^{-1} \quad , \tag{12c}$$

where the k_{NR} are the extinction coefficients for the non-resonant *absorption of the pump x-rays*. It *is important to notice that* this is a typical case in which the pump radiation is not particularly close to an absorption edge. In this case the emerging photoelectrons will have some kinetic energy, and may escape from the region being pumped. Had the example been arranged to be more pathological as in the recently reported case[9] of the ^{57}Fe, Eq. (12c) would have given a much larger absorption coefficient. As it is, the non-resonant absorption by the working medium in the 0.67μm layer is only,

$$f_1 = k_{NR} \ (10\% \ Ta) \ x = 2.4 \times 10^{-3} \quad , \tag{13}$$

where f_1 is the fraction of the incident fluence stopped in the laser medium by non-resonant absorption. However, this fraction is reduced further by the escape of the primary photoelections from the pumped layer.

Figure 3 shows the mean extrapolated ranges, E/(dE/dx) computed by standard techniques[12] for the escape of photoelectrons having the energies shown in the materials indicated. In this case the Ta is considered to be in the normal (100%) concentration. In the 10% concentration being assumed the ranges would be 10× greater and so the

contribution of the working medium to the absorption of the primary photoelectrons would be dominated by the effects of the diluent.
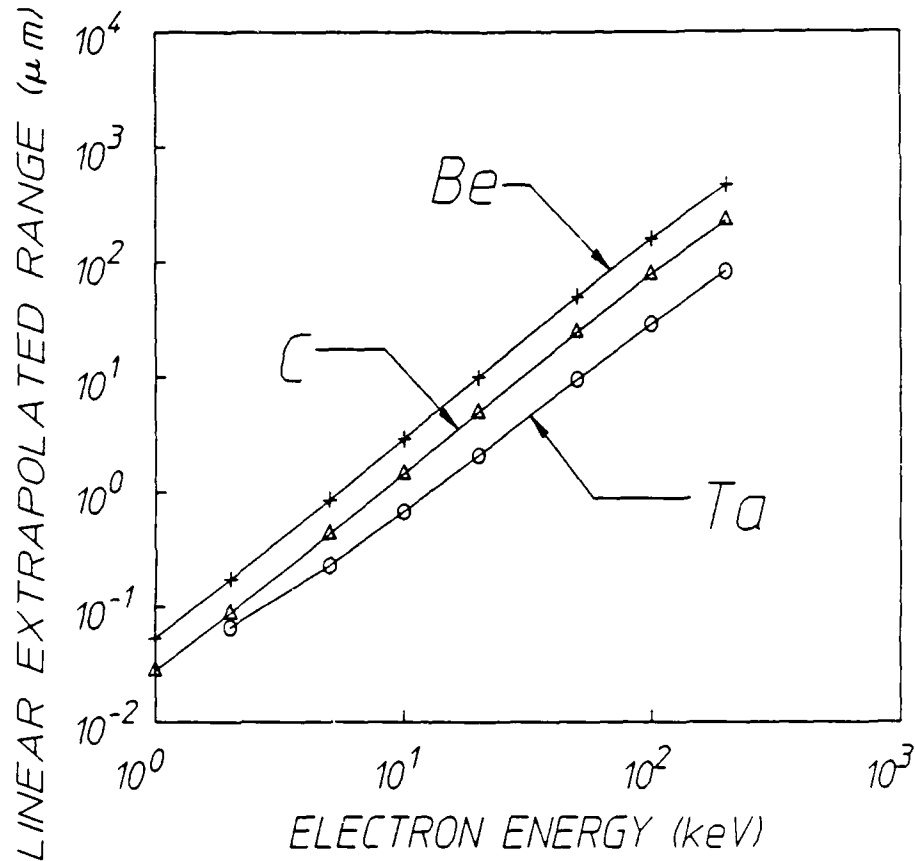
Figure 3: Plot of the linear extrapolated range of electrons in foils of the materials shown.

For the likely cases of rare earth or platinide elements the pump energy we assume lies below the K-edge and about 15 keV above the L-edge. As a result, the primary photoelectrons resulting from the non-resonant absorption in the active medium should have energies of the order of 15 keV and ranges of 6.0 and 3.0μm in Be and C, respectively. Thus, only about 10% and 20% respectively, of the primaries, should be stopped in the 0.67μm thick host films of Be or diamond. Multiplying the fraction of Eq. (13) by these probabilities for collision of the primary in the foil gives the fractions,

10

$$f_2 \ (Be) = 2.4 \times 10^{-4} \quad , \tag{14a}$$

$$f_2 \ (C) = 4.8 \times 10^{-4} \quad , \tag{14b}$$

for the fraction of the energy from the incident pump degraded into heat in the laser film because of non-resonant absorption.

Considering that edge filters or ablation layers could reduce the bandwidth of the pump radiation to 3 keV, before reaching the doped layer of Fig. 2, the incident fluence lying outside the bandwidth for resonant absorption would be 3000× greater than the value of Eq. (10b). However, only the fractions of Eqs. (14a) and (14b) are capable of being degraded into heat in the sensitive layer. The resulting energy balance can then be summarized at threshold:

Lattice	Be	C(diamond)
Resonant input fluence	177mJ/cm^2	177mJ/cm^2
Fluence degraded to heat	127mJ/cm^2	255mJ/cm^2

There is an additional potential for heating in the resonant term as well. Reference to Fig. 1 will show that for each absorption to the giant funneling state, a cascade is started that reaches finally to the level being inverted. Since the isomer may start at several MeV, while the output transition accounts for only 100 keV, there is the possibility of exciting a sequence of radiative transitions emitting a total of several MeV for each nuclei inverted. Were this to occur in a sequence of many soft transitions of a few keV these could be internally converted to give low energy electrons which would then be unable to escape the 0.67μm layer being pumped. They would deposit their energies in the layer as heat.

For a number of reasons a significant contribution to the heating from cascades following resonant absorption is unlikely. The most probable spontaneous transitions are those spanning larger gaps of energy and those are seldom converted internally. The ones that are converted will give electrons of higher energies which Fig. 3 shows to have higher probabilities of escape from the layer. It is most reasonable to expect the dominant source of heat to be the energy lying in the broader bandwidth of the pump continuum as discussed above.

11

The elements of the energy economy tabulated above are the fluences stopped in the thin working layer in which the nuclear populations are being inverted. Dividing those fluences by the $0.67\mu m$ thickness gives the energy loading of the laser film,

Lattice	Be	C(diamond)
Resonant energy density	$2.6KJ/cm^3$	$2.6KJ/cm^3$
Thermal loading	$1.9KJ/cm^3$	$3.8KJ/cm^3$

These values are quite significantly <u>below</u> the levels of heating required to degrade the recoil free fractions in the case of the diamond lattice. Baldwin has summarized[13] the involved dependence of the recoil free fraction of gamma transitions upon recoil energy, lattice parameters and temperature. He shows that even at a temperature, T equal to the Debeye temperature, Θ_D the recoil free fraction is not significantly degraded (by more than a factor of 2) for a transition even as energetic as to give a classical recoil energy of $0.14\ \Theta_D$. In diamond with $\Theta_D -$ 2230° K this means a transition of 100 keV is little affected by a temperature increase up to $T - \Theta_D$.

It is a textbook computation[14] to estimate that the energy content of the phonons of a material with $\Theta_D - 2230°$ K at a temperature of $T - \Theta_D$ is about $11KJ/cm^3$. Comparing this with the estimated loading of $3.8KJ/cm^3$ gives a "safety factor" of almost 3x. A comparable margin is obtained for the Be.

To summarize, it is convenient to recast the threshold fluence of Eq. (10b) into more tangible terms. The spectral fluence of $177mJ/cm^2/eV$ corresponds to 530 J/cm^2 if the bandwidth of the pump x-rays is arranged to be 3 keV, a practical separation which might be filtered between K-edges. Even if pumped instantaneously, so that no waste heat were transported away, the thermal loading would reach only 1/3 of the way to the limit for retaining the Mössbauer effect. If derived from an x-ray line of 30 eV width, the threshold fluence would be only 5.3 J/cm^2. In that case the thermal loading would reach only 1/300 of the critical limit for a diamond lattice.

Even beyond this point much can be done to reduce heating further. All calculations so far were done for the instantaneous generation of the waste heat. The time for the transport of a phonon across the $0.67\mu m$ thickness of the working layer is of the order of only 100 psec so that the transport of significant amounts of heat from that layer into a diamond heat sink is possible on a nanosecond time scale. Yet the lifetimes of most of the fluorescent levels of interest for inversion[2] have lifetimes of tens of nsec to tens of μsec. This is many times the period for the transport of phonons out of the inverting layer so that more orders of magnitude can be realized in reducing the thermal loading further below the limits specified so far. However, all these techniques require precise knowledge about the energy levels and absorption edges of the materials involved. Until the identity of the best candidate for a gamma-ray laser is known, the exact specifications of the solution to the disposal of the waste heat cannot be generally articulated. The examples considered here show that there are many orders of magnitude in the safety margin between likely amounts of heating and the much larger amounts which can be tolerated in stiff lattices such as Be and diamond.

The greatest significance is that the fourth and last of the tenents of theoretical dogma inhibiting the development of a gamma-ray laser is eliminated by these arguments. There is no need to melt the host lattice in order to pump a nuclear system to the laser threshold. *There are no a priori obstacles to the realization of a gamma-ray laser.* A gamma-ray laser is feasible if the right combination of energy levels occurs in some real material. The overriding question to resolve is whether or not one of the better of the 29 candidates has its isomeric level within a few tens or even hundreds of keV of one of the giant resonances for dumping angular momenta, such as found in $^{180}Ta^m$ and $^{123}Te^m$.

REFERENCES

1. G. C. Baldwin, J. C. Solem, and V. I. Goldanskii, Rev. Mod. Phys. 53, 687 (1981).

2. C. B. Collins, F. W. Lee, D. M. Shemwell, and B. D. DePaola, J. Appl. Phys. 53, 4645 (1982).

3. J. A. Anderson and C. B. Collins, Rev. Sci. Instrum. 58, 2157 (1987).

4. C. B. Collins, C. D. Eberhard, J. W. Glesener, and J. A. Anderson, Phys. Rev. C 37, 2267 (1988).

5. C. D. Eberhard, J. W. Glesener, Y. Paiss, J. A. Anderson, C. B. Collins, W. L. Hodge, E. C. Scarbrough, and P. O. Antich, Phys. Rev. C (pending).

6. C. B. Collins, J. A. Anderson, C. D. Eberhard, J. F. McCoy, J. J. Carroll, E. C. Scarbrough, and P. P. Antich, in Center for Quantum Electronics Report #GRL 8703, University of Texas at Dallas, 1987 (unpublished) pp 35-53.

7. J. A. Anderson, C. D. Eberhard, J. F. McCoy, K. N. Taylor, J. J. Carroll, M. J. Byrd, C. B. Collins, E. C. Scarbrough and P. P. Antich, in Center for Quantum Electronics Report #GRL 8704, University of Texas at Dallas, 1988 (unpublished) pp 11-35.

8. C. B. Collins in Center for Quantum Electronics Report #GRL 8601, University of Texas at Dallas, 1986 (unpublished) pp 1-14.

9. D. A. Swallow, Bull. Am. Phys. Soc. 33, 1017 (1988), Presentation GC3.

10. M. S. Weiss, Bull. Am. Phys. Soc. 33, 1017 (1988), Presentation GC4.

11. S. S. Wagal, E. M. Juengerman and C. B. Collins, Appl. Phys. Lett. 53, 187 (1988).

12. G. Knop and W. Paul, in: Alpha, Beta and Gamma-Ray Spectroscopy (ed. Kai Siegbahn, North-Hollard Co., Amsterdam, 1965), p 1-25.

13. See Ref 1, Fig. 14.

14. C. Kittel, Introduction to Solid State Physics, 6th ed. (Wiley, New York, 1986), p. 106.

14

DETERMINATION OF GATEWAY STATES IN ^{197}Au WITH A COMPTON γ-RAY SPECTROMETER

by C. D. Eberhard, J. A. Anderson, M. J. Byrd, J. J. Carroll
and C. B. Collins
Center for Quantum Electronics, University of Texas at Dallas
and E. Scarbrough and P. P. Antich
University of Texas Southwestern Medical Center

Introduction

Recent experiments[1,2,3,4] have shown that cross sections for (γ, γ') reactions that populate nuclear isomers can be orders of magnitude larger than previously expected at excitation energies above about 2 MeV. These results were obtained by pumping nuclear populations with the bremsstrahlung radiation from a Varian CLINAC 1800 linear accelerator normally employed for radiation therapy treatments. Unfortunately, such bremsstrahlung sources are inherently continuous and cannot be used to selectively probe for the intermediate gateway states through which the isomeric excitation occurs. Moreover, not even the endpoint energy of this particular device can be varied around its operating point of 6 MeV. Thus, in this previous work there was no direct way of identifying the 'gateway levels which mediated the population of the observed isomeric states. To facilitate this identification process, a technique has been developed in which Compton scattering is used to progressively modify the energy endpoint and spectral distribution of the incident radiation. The current work describes this method and discusses its application to the study of the gateway states through which the reaction ^{197}Au$(\gamma, \gamma')^{197}$Au^m is excited.

The Compton Effect

The Compton effect[5] describes the collision of a primary photon of energy E_0 with an essentially unbound atomic electron assumed to be initially at rest. The process is named for A. H. Compton, who established it quantitatively in 1923 after careful spectroscopic measurements of x-rays scattered through various angles by light elements. In the collision, the incident momentum and energy must be conserved between the scattered photon and the struck electron, which recoils. The scattered photon has less momentum and energy than the primary photon, with the remaining momentum and energy being imparted to the electron. The consequences of this phenomena can be quantitatively described by a rather straightforward approach.
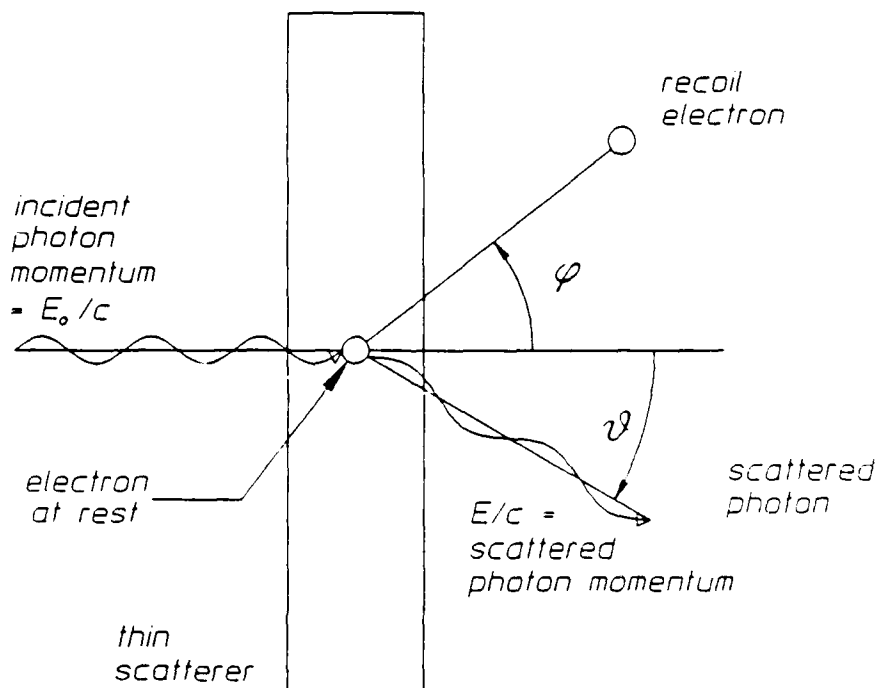

Figure 1: Diagram of the initial and final momenta for Compton scattering.

Let the angle between the propagation vectors of the primary and scattered photons be denoted by θ as shown in Fig. 1. From the relativistic energy-momentum relation and the conservation of energy and momentum, the energy of the scattered photon is found to be given by

$$E = \frac{E_0}{[1 + (E_0/mc^2)(1 - \cos \theta)]} \qquad (1)$$

where mc^2 is the rest mass of the electron. There is a one-to-one correlation between the energy of the scattered photon and the angle θ for a given primary photon energy E_0. Therefore, photons from a monochromatic source which are scattered into a given angle from a point scatterer will be monochromatic. This leads to the possibility of performing nuclear spectroscopy with Compton scattered radiation having a known spectral distribution. A configuration for a Compton spectrometer to be used in the study of the activation of short lived isomers is shown in Fig. 2.
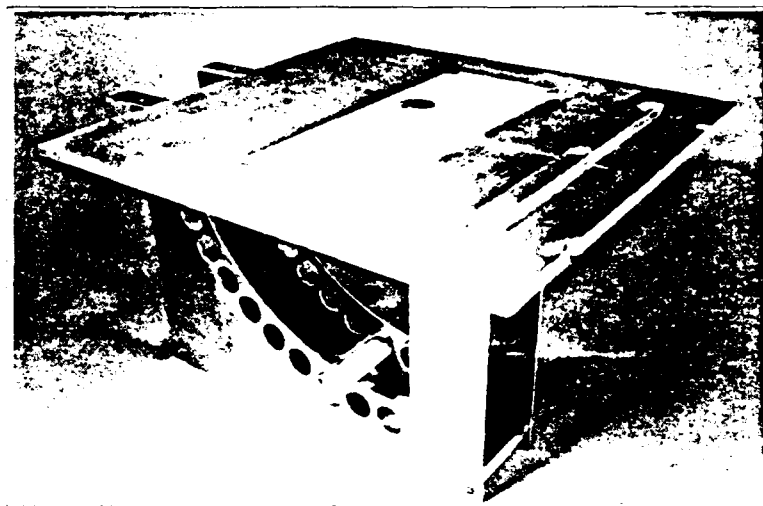

Figure 2: Irradiation fixture of the Compton spectrometer showing a sample in the $\theta = 8°$ position. The pneumatic tubing of the transport system passed through the holes in the sample holder so that the sample was positioned as shown. The tubing was moved from site to site manually.

In the theory of the Compton effect, the struck electron is considered to be free or unbound. This limits the theory to cases for which the atomic binding energy of the electron is small compared with E_0, which is the case for the primary photon spectrum considered here. Also, the electron is assumed to be at rest. Although the general case of non-zero electron momentum can be obtained from this special case by a Lorentz transformation, this refinement is generally not considered necessary. In 1928 the complete theory for the effect was worked out by Klein and Nishina using Dirac's relativistic theory of the electron. The differential cross section obtained for the scattering of unpolarized incident photons of energy E_0 into the solid angle $d\Omega$ at the polar angle ϑ is given by

$$\frac{d\sigma}{d\Omega} = r_o^2 \left(\frac{1}{1 + \alpha_i (1 - \cos \theta)} \right)^2 \left(\frac{1 + \cos^2 \theta}{2} \right) \times \qquad (2)$$

$$\left(1 + \frac{\alpha_i^2 (1 - \cos \theta)^2}{(1 + \cos^2 \theta)[1 + \alpha_i(1 - \cos \theta)]} \right) \quad .$$

where $\alpha_i = E_0/mc^2$ is the incident photon energy in units of mc^2 and $r_0 = e^2/mc^2$ is the classical radius of the electron. The differential scattering cross section is defined through the relationship

$$dR(\vartheta, E_0) = dI_i(E_0) N_{sc} \frac{d\sigma}{d\Omega} (E_0, \vartheta) \; d\Omega(\vartheta) \qquad , \qquad (3)$$

where

dR = number of photons per second scattered into

solid angle $d\Omega$ at θ,

N_{sc} = number of electrons per cm^3 in the scatterer, and

$dI_i(E_0)$ = incident photon flux with energy E_0 in

photons per cm^2 per s.

After substitutions for the solid angle,

18

$$d\Omega = 2\pi \sin \theta \ d\theta \qquad , \tag{4}$$

and the area at the target location at radius r intersected by the conical fan described by $d\Omega$,

$$dA = 2\pi r^2 \sin \theta \ d\theta \qquad , \tag{5}$$

Eq. (3) may be rewritten for the scattered flux as

$$dI_f = \frac{dR}{dA} = dI_i \ \frac{d\sigma}{d\Omega} \ \frac{1}{r^2} \qquad . \tag{6}$$

A real experimental source is not monochromatic, but a small portion of the spectrum can be represented by

$$dI_i = \frac{dI_i}{dE} \ dE_i \qquad , \tag{7}$$

where dI_i/dE is the spectral density of the incident flux. Written in terms of the spectral density, Eq. (6) becomes

$$dI_f = \frac{dI_i}{dE_i} \ \frac{d\sigma}{d\Omega} \ \frac{1}{r^2} \ dE_i \qquad . \tag{8}$$

The energy spread of the scattered photons relative to the energy spread of the incident photons is found by differentiating equation (1),

$$dE = dE_i \ \left[1 + \alpha_i(1 - \cos \theta)\right]^{-2} \qquad . \tag{9}$$

Equation (8) becomes

19

$$\frac{dI_f}{dE} = \frac{dI_i}{dE_i} \frac{d\sigma}{d\Omega} (\theta, E_o) \frac{[1 + \alpha_i(1 - \cos\theta)]^2}{r^2} \qquad (10)$$

The quantity dI_f/dE is the output spectral density, a function of θ and E, the scattered photon energy. Thus for a non-monochromatic incident spectrum, the output spectral density can be calculated on a point-by point basis.

The preceding discussion assumed a point scatterer and a point absorber at which one could calculate the spectral density of the scattered radiation. As shown in Fig. 2, both scatterer and absorber have finite volumes which must be accommodated in the calculation of the output spectral density. Since the scattering target must in practice be chosen large enough to produce a significant scattered photon flux, it cannot be considered to be thin in comparison to the mean free path of a photon. Therefore there will be significant multiple scattering in a real target. Although the correct solution of this problem requires a full radiation transport calculation, a first approximation has been made in this work by treating the scattering target as a collection of individual point scatterers and using a simple attenuation calculation to adjust the incident and scattered intensities from each point. This in effect assumes that all secondary scattering events result in absorption. The output spectral density at a given point in the absorber is then the summation of the contributions from all the volume elements in the scatterer. Since the output spectrum is sensitive to position within the absorber, it is necessary to average this output spectral density over the volume of the absorbing sample. A more complete, Monte Carlo based calculation is in progress.

The source of primary photons used in this work was a Varian Clinac 1800 linear accelerator designed for medical applications. Electrons accelerated to an energy of 6 MeV impact a copper target to produce a photon beam with a well characterized bremsstrahlung spectrum[6]. The spatial variation of this bremsstrahlung spectrum over the area of the scatterer has been measured and is negligible[7].

The output spectral density for the Compton spectrometer was calculated using Eq. (10). For every pair of volume elements in the scatterer and absorber, the geometrical factors r and $\cos\theta$ were determined. Then, for each value of the output energy to be considered,

20

the corresponding E_0 was found, and the input spectral density was obtained from a piecewise-continuous fit generated from the results of Mohan et al. This spectrum was adjusted for exponential attenuation of the incident radiation by applying the factor $\exp(-\mu(E_0)z)$, where z is the vertical distance of the scattering point from the top of the scattering target and $\mu(E_0)$ is the mass attenuation coefficient at incident photon energy E_0. After the application of Eq. (10) to obtain the spectrum dI_f/dE of the Compton scattered radiation, a second attenuation correction of $\exp(-\mu(E)d)$ was made. Here, d is the path-length the scattered photon of energy E travels as it exits the scattering target. These results were summed over the scatterer volume and averaged over the absorber volume to produce the spectral density seen by the absorber. In order to test the sensitivity of the model to the geometrical assumptions, the output spectral density at $\theta = 16°$ was calculated for the following four possible geometrical cases:

1. Point scatterer/point absorber: the masses of the scatterer and absorber were considered to be concentrated at the respective geometrical centers. Attenuation in the scatterer was calculated using the appropriate path lengths from the boundary of the scatterer to its center.

2. Extended scatterer/point absorber: the scatterer was divided into volume elements but only the central point of the absorber was considered.

3. Point scatterer/extended absorber: the scatterer was concentrated at its center but the absorber was considered to have an extended volume. Attenuation in the scatterer was calculated using the appropriate path lengths from the boundary of the scatterer to its center.

4. Extended scatterer/extended absorber: the finite dimensions of both scatterer and absorber were considered in this model.
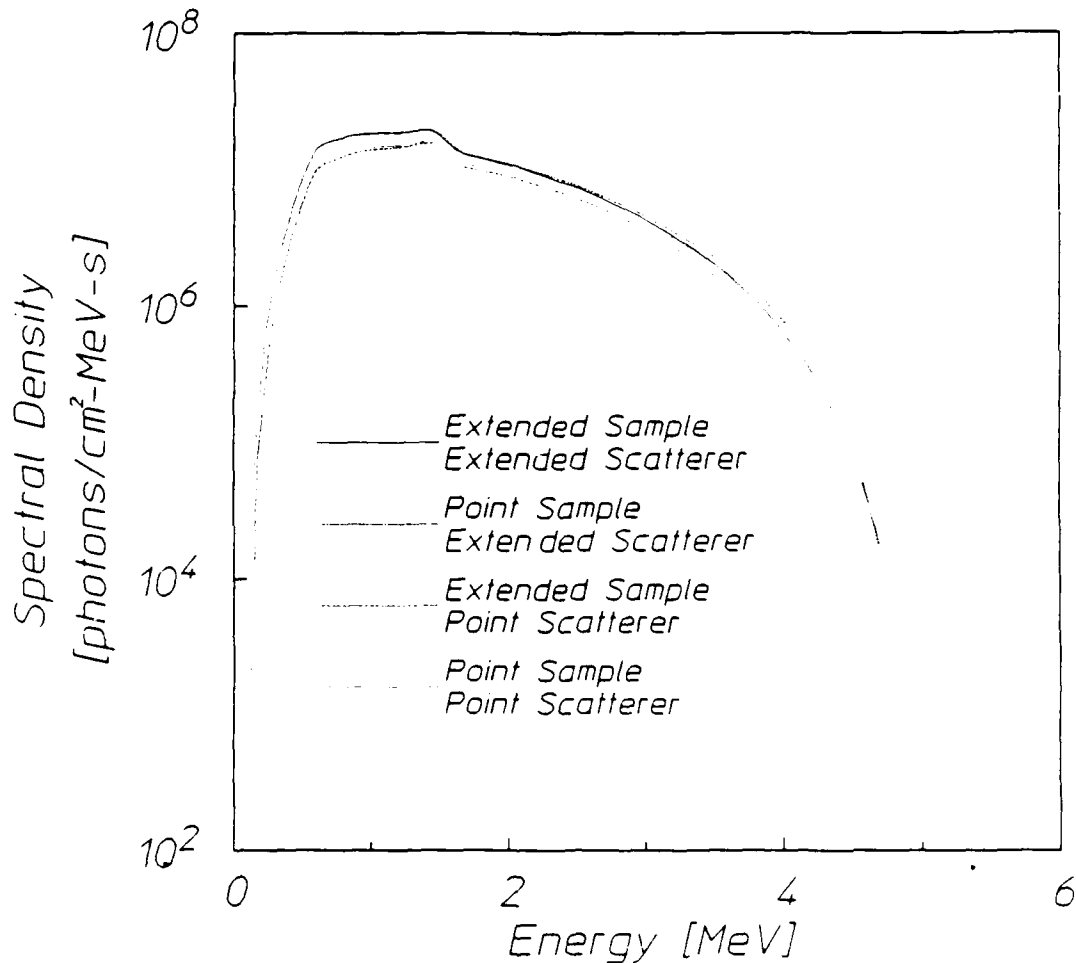
Figure 3: Modelled output spectral densities at the position of the absorber at the 16° spectrometer position for the four geometrical assumptions.

The results of these calculations are shown in Fig. 3. It should be noted that the single-point scatterer models underestimate the low energy portion of the spectrum because of the relatively long absorption path from the center of the scattering target to its boundary. Inclusion of the finite extent of the absorber sample increased the maximum photon energy incident on the absorber because it allowed contributions from lower scattering angles in the Compton process to be made for a given central angle θ. The extended source/extended scatterer model was used throughout the remainder of the work. These extended geometry calculations were performed for scattering angles of 0°, 16°, 24°, 32°

and 40°. The Compton scattered spectral densities are shown plotted in Fig. 4.
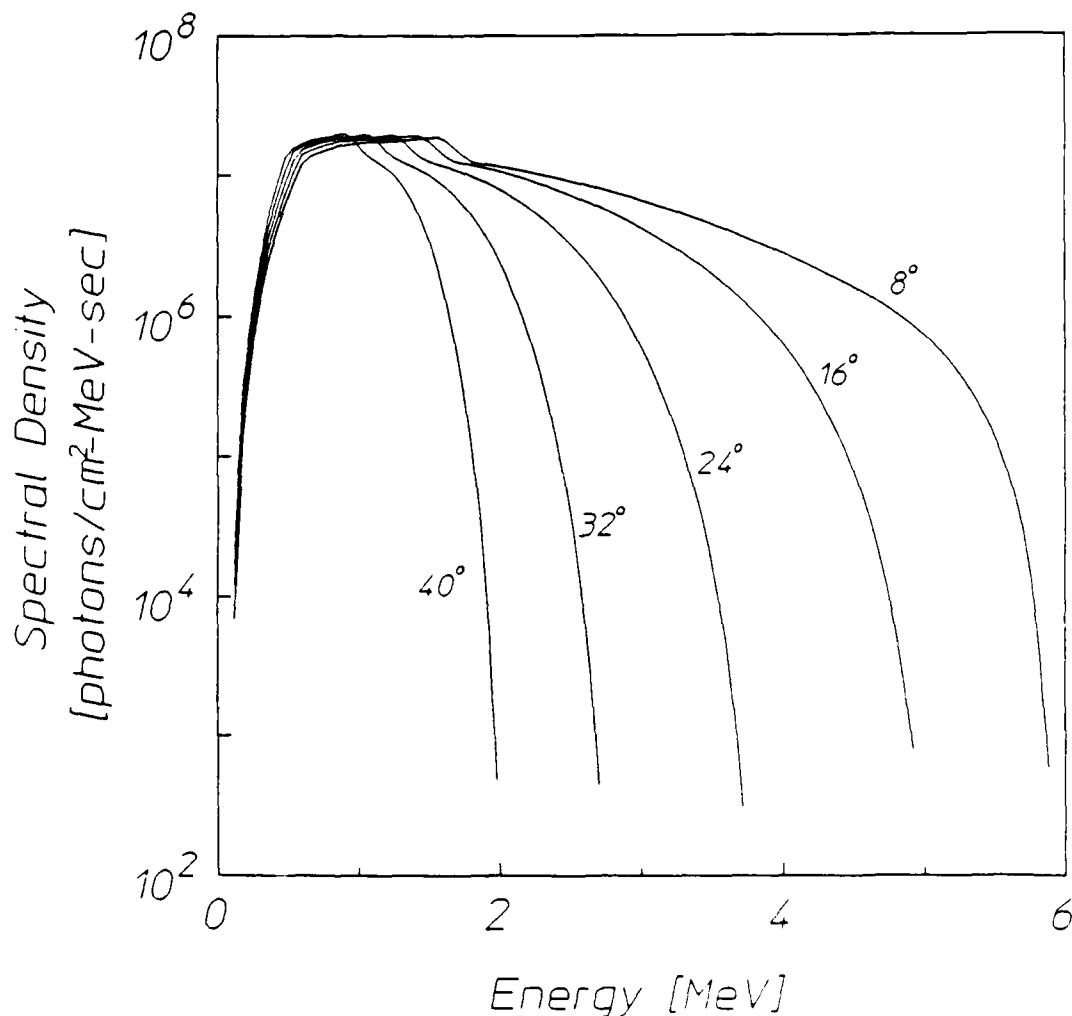
Figure 4. Modelled output spectral densities of the extended scatterer/extended absorber geometry for the scattering angles of 0°, 8°, 16°, 24°, and 32°.

A point of interest concerning the output spectrum is the end-point energy, or that point above which there is no spectral density. By the point-to-point model, the end-point energy, E_{max}, is given by Eq. (1). However, due to the extended geometry of the scatterer and target, lower angles are encountered which contribute energies higher than the

point-to-point value, increasing the maximum energy of the radiation illuminating the sample. A comparison of the calculated E_{max} for the point-to-point case and the extended geometry model is shown in Table I.

Table I

End-point energies for extended and point-to-point and geometry calculations.

Angle	E_{max} Extended Geometry	E_{max} Point-to-Point Geometry
0°	6.00	6.00
8°	5.88	5.38
16°	4.92	4.12
24°	3.72	2.98
32°	2.70	2.16
40°	1.98	1.60

Long lived isomeric states can be activated either directly or through one or more gateway[8] states as shown in Fig. 5. The long halflife of the isomeric state leads to a very narrow linewidth. Since the excitation of a particular state is proportional to the linewidth, direct activation of the isomer is considered to be negligible. A gateway state must be excited from the ground state by the absorption of a single photon. Some fraction of the decays from the gateway state then leads to the isomeric state either directly or through a multi-step cascade.

If the activation of the metastable state is assumed to proceed through one gateway state, then the total number of activations is given by

24

$$N_m = b_o N_t T \int_o^\infty \sigma(E) dI(E) = b_o N_t T \int_o^\infty \sigma(E) \frac{dI(E)}{dE} dE \qquad , \qquad (11)$$
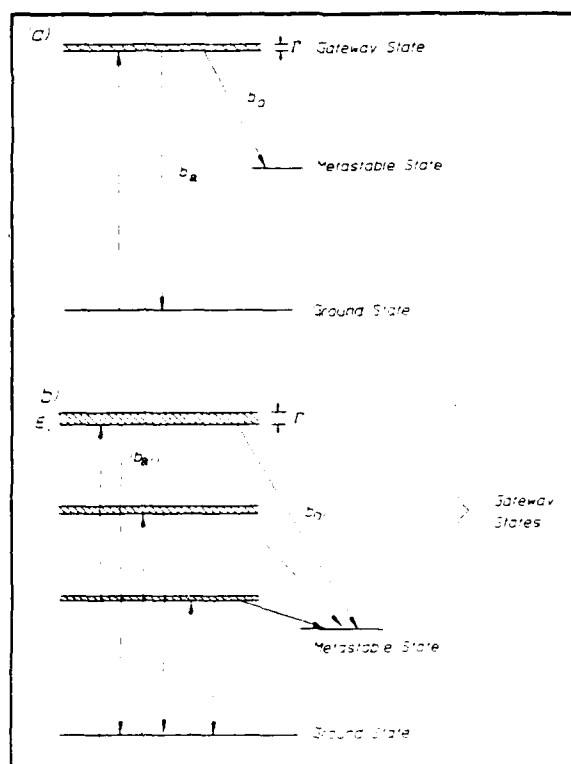
Figure 5(a): Energy level diagram of a single gateway isotope. (b): Energy level diagram of a multiple gateway isotope.

where b_o is the branching ratio of the decay of the gateway state into the metastable state, T is the irradiation time, and $dI(E)$ is the differential increment of flux with energy between E and E + dE. The Breit-Wigner cross section $\sigma(E)$ for the absorption of a photon when the resonant transition energy is E_r is given by

$$\sigma(E) = \frac{\lambda^2}{8\pi} \frac{2I_f + 1}{2I_i + 1} \frac{\Gamma_a \Gamma}{[(E - E_r)^2 + (\Gamma/2)^2]} \qquad , \qquad (12A)$$

25

$$
= \frac{\sigma_o}{4} \frac{b_a \Gamma^2}{[(E - E_r)^2 + (\Gamma/2)^2]} \quad , \tag{12B}
$$

where the symbols are defined as follows:

λ — photon wavelength,

I_i, I_f — initial and final angular momenta of the nucleus,

Γ — total level width of the gateway state,

$\Gamma_a = b_a \Gamma/(1 + \alpha_p)$ — partial width of the gateway state for electromagnetic transitions to the ground state,

α_p — total internal conversion coefficient for the absorption transition, and

$$
\sigma_o = \frac{\lambda^2}{2\pi} \frac{2I_f + 1}{2I_i + 1} \frac{1}{(\alpha_p + 1)} \quad .
$$

This nomenclature is consistent with that used in the Mossbauer spectroscopy community.

If the spectral density (dI/dE) can be considered to be constant in the vicinity of the absorption line, the integral in Eq. (11) becomes

$$
N_m = N_t b_o \left. \frac{dI}{dE} \right|_{E_r} T \int_o^\infty \sigma(E) dE \tag{13}
$$

$$
= N_t (\pi \sigma_o b_a b_o \Gamma/2) \left. \frac{dI}{dE} \right|_{E_r} T \quad ,
$$

where $(dI/dE)|_{E_r}$ is the spectral density evaluated at the resonance energy, E_r. Thus the effective cross section for this activation is given by

$$\sigma_{eff} = \pi b_a b_o \sigma_o \Gamma/2 \quad cm^2\text{-}keV \quad , \tag{14}$$

and the activation A may be written

$$A = (N_m/N_t) = \sigma_{eff} \left. \frac{dI}{dE} \right|_{E_r} T \quad . \tag{15}$$

When there are two or more gateway states which may decay into the metastable level, the integral in Eq. (11) is replaced by a summation of integrals, one for each of the i gateway states, and it must be rewritten as

$$N_m = N_t T \sum_i \left[\sigma_{eff}(E_i) \left. \frac{dI}{dE} \right|_{E_i} \right] \quad . \tag{16}$$

While some gateway energies have been found through the use of variable end-point devices[9,10], in many cases the gateways have not been identified. The spectra shown in Fig. 4 indicate that by using a Compton spectrometer one may achieve results similar to those obtained with a variable end-point device, provided that the scattered radiation has adequate intensity. That is, although the scattered intensity will be substantially reduced from that in the primary beam, it must still be sufficient to produce statistically significant activation within the lifetime of the fluorescent level. As an example of this potential application, the spectra of Fig. 4 were used to generate sample activation results for several configurations of gateway states. These numbers correspond to the time corrected activations which would be observed in the samples after irradiation at the appropriate Compton angle. Based on the output spectral density dI/dE of the spectrometer as a function of angle, the effective cross section is obtained from Eq. (15) as

$$\sigma_{eff} = \frac{N_m}{N_t \dfrac{dI}{dE} T} = \frac{A}{\dfrac{dI}{dE} T} \quad . \tag{17}$$

A family of these curves based on the assumption that there is only one gateway state producing the isomer is shown in Fig. 6. These

curves are seen to intersect at the one energy corresponding to that of
the gateway state. When there are two possible gateways, the family of
curves similar to those seen in Fig. 7 is generated. This hypothetical
case has one gateway at 2 MeV having a cross section of 10^{-26} cm^2-keV and
a second gateway at 4 MeV with a corresponding cross section of 10^{-25}
cm^2-keV. The family of curves obtained demonstrates considerably more
complexity and the contributing gateways cannot be visually identified
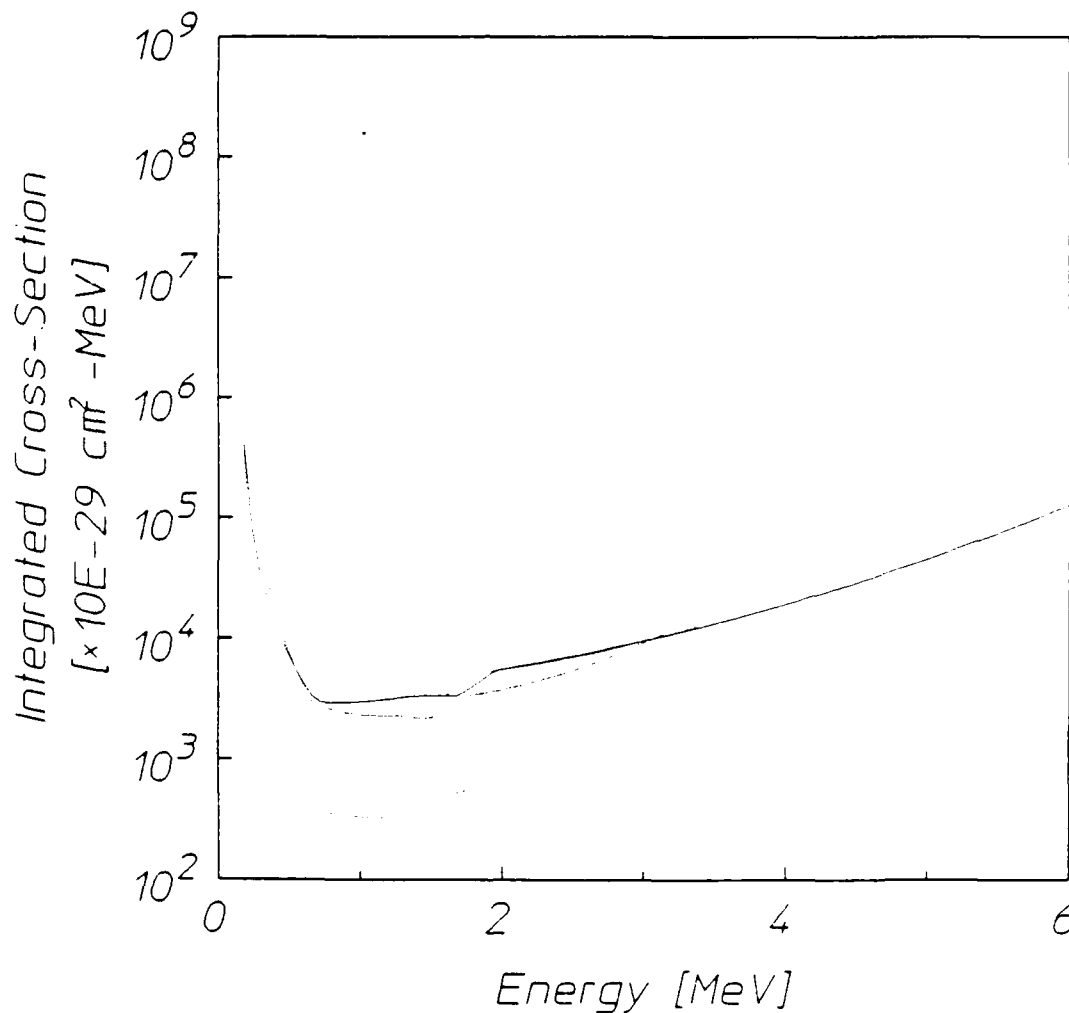as they were in Fig. 6.

Figure 6: Synthetic curves of the cross section in units of 10^{-29}
cm^2-keV as a function of gateway energy for the case of a single gateway
state. The assumed spectral densities were those shown in Figure 4.

28
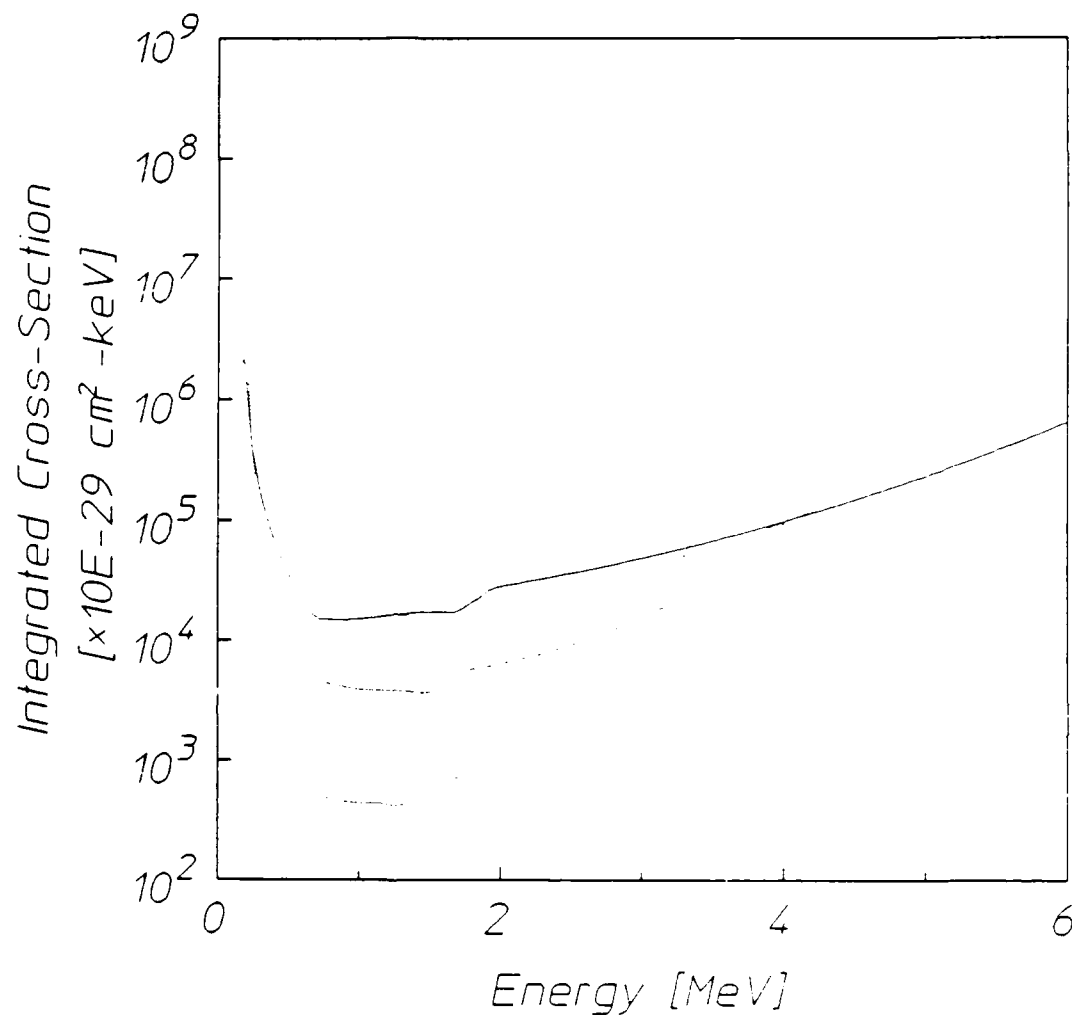
Figure 7: Synthetic curves of the cross section in units of 10^{-29} cm^2-keV as a function of gateway energy for the case of two gateway states.

Experimental Details

The irradiation fixture pictured in Fig. 2 was constructed to hold the samples during exposure. This jig was mounted at the filter tray position of the Varian Clinac 1800 linac employed for this work, thus holding the scattering center 65 cm from the x-ray converter target. The total incident photon flux at this position is $2.2 \cdot 10^{10}$ pho-

29

tons/cm^2-sec. A layer of 5 cm of lead shielding was placed in the plane of the Compton target to prevent radiation scattered off the Clinac collimators from reaching the sample positions and contaminating the experiment. The 2.54 cm diameter by 2.54 cm long stainless steel cylinder used as the scattering element nested in an aperture through this secondary shield. Bremsstrahlung radiation from the linac was restricted by the machine collimators until it illuminated only the scattering center.

The fixture had provisions for placing samples at angles corresponding to integral multiples of 8°. Samples were held inside a pneumatic transfer tube at a radial distance of 20.3 cm from the center of the scattering target. The wall thickness of the aluminum transfer tube was only 0.025 cm, presenting a negligible attenuation in the energy range of interest (>1 MeV) in this experiment. A valve on the pneumatic system also allowed the sample to be transferred back to the irradiation site. This was a great convenience, since entry into the CLINAC cell to relocate the sample for exposure would have otherwise required an additional 2 minutes per irradiation.

30
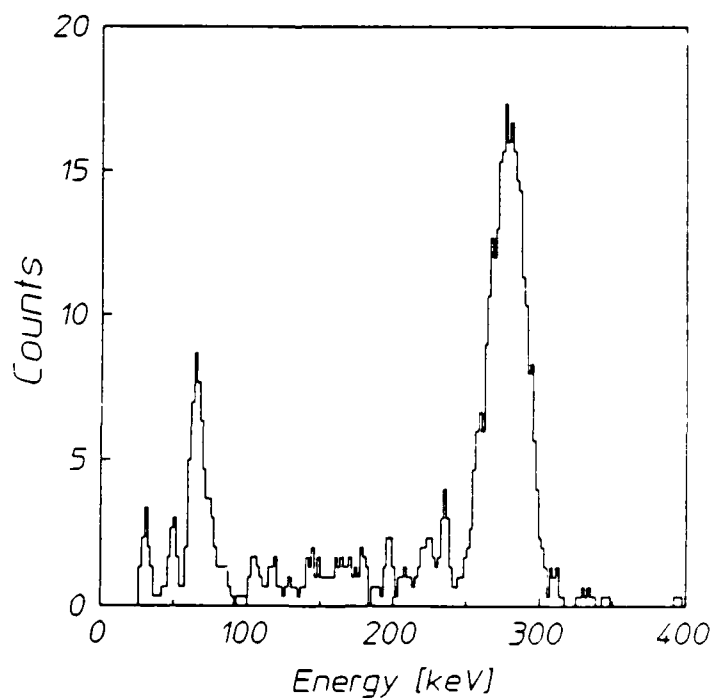
Figure 9: Time decay spectrum of the decay
of the $^{197}Au^m$ produced by the exposure to
the Compton scattered spectrum of the
LINAC.

In each trial, the sample was exposed for 60 s. Immediately after
the irradiation, the sample was automatically transferred from the
exposure position to the detector, where it was counted for 20 s. A
timer was started at the end of the exposure and stopped by the arrival
of the sample at the detector. This timing information was used to
correct the observed number of counts for losses during the transit
interval.

The detector used in this work was a 7.62 cm x 7.62 cm NaI(Tl)
detector with a 2.54 diameter well 5.08 cm deep. Data acquisition began
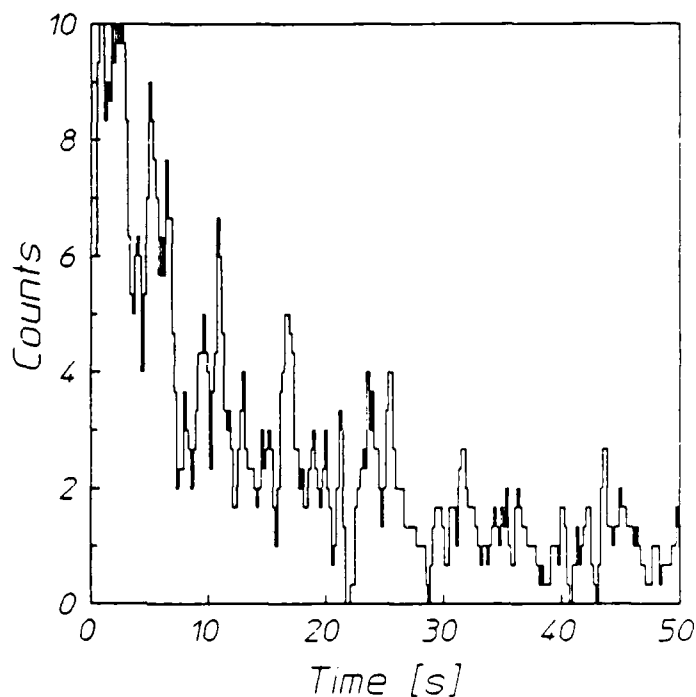automatically upon arrival of the sample at the detector. A pulse

Figure 8 (Opposite): Pulse height spectrum of the decay of the $^{197}Au^m$
produced by the exposure of the Compton scattered spectrum of the LINAC.

31

automatically upon arrival of the sample at the detector. A pulse height spectrum and a time decay spectrum were simultaneously obtained for each case. Examples of these spectra are shown in Figs. 8 and 9. The pulse height spectra were used to obtain the results discussed here. Absolute counting efficiencies for this system were obtained by calibration against standardized sources. The observed counts in the 279 keV peak of $^{197}Au^m$ were corrected for absolute efficiency, self-absorption of the emitted gamma-rays, counting losses during irradiation and transit, and for the gamma-ray intensity to obtain the total number of excitations occurring during the exposure. Table II contains the number of trials made at each angle, the transit time for each trial, the number of photopeak counts observed, and the number of excitations produced. Table III lists the characteristic parameters for the gold sample used in this work. From the measured values, the product

$$\sigma_{eff} \times \frac{dI}{dE} = \frac{N_m}{N_t\, T} \tag{18}$$

was calculated for each observed angle for use in the analysis that has been previously described.

Table II

Summary of data from the Compton spectrometer experiments. Corrections
to the observed photopeaks were made as described in the text. Photo-
peak areas were obtained using the commercial peak analysis program GDR
Version 4.0

Angle (deg)	Number of Trials	Transit Time(s)	Total Photopeak	Average Isomeric
0*	1	1.87	19374	$1.08 \times 10^6 \pm 7.3 \times 10^3$
8	1	1.90	244	$3.51 \times 10^3 \pm 2.2 \times 10^2$
16	2	1.82	84	$6.00 \times 10^2 \pm 6.6 \times 10^1$
24	4	1.82	78	$2.86 \times 10^2 \pm 3.2 \times 10^1$
32	4	1.87	40	$1.44 \times 10^2 \pm 2.3 \times 10^1$
40	4	1.80	45	$1.57 \times 10^2 \pm 2.4 \times 10^1$

* No scatterer, exposed to primary beam. [4]

Table III

Sample parameters for this work.

Sample Composition	99+	% Au
Sample Mass	31.6	g
Isotopic Abundance	100	%
Number of Target Nuclei	9.52×10^{22}	
Gamma-ray energy	279	keV
Gamma-ray intensity @ 279 keV	73.11	%
Self-absorption factor	0.305	

Data Analysis

The spectral intensity was calculated using the techniques de-
scribed above for each of the sample positions used in the experiment.
As previously discussed, the input spectrum used in this work was a
piecewise-continuous curve fitted to the results of Mohan et al.[6]
Expected uncertainties associated with the spectral intensity calcula-
tion were obtained by fitting a second piece-wise continuous curve to
the reported uncertainties in Mohan's work. The two curves representing
the envelope of the input model spectrum plus and minus these fitted
uncertainties are plotted in Fig. 10 with the original results from
Mohan. The envelope curves bound the Monte Carlo results and are
consistent with their error bars. Uncertainties in the Compton scat-
tered intensities were obtained by repeating the extended geometry
calculations with the envelope curves of Fig. 10 as input data. The
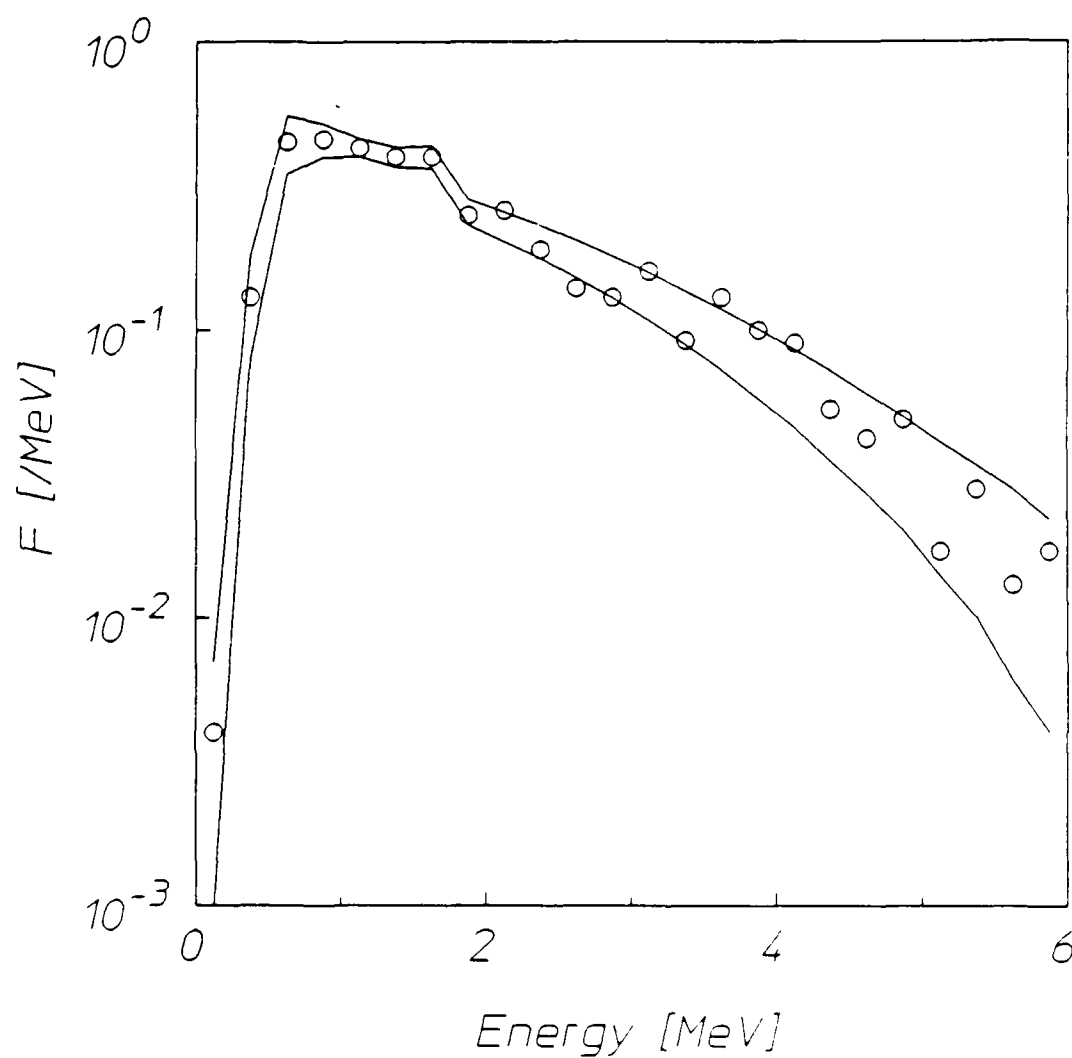results for the case $\theta = 16°$ are shown in Fig. 11.

34

Figure 10: Curves representing the envelope of uncertainty of the input spectral density. This was obtained by fiting piece-wise continuous curves to the uncertainties of the spectrum generated by Mohan. The open circles represent the most porbable values of the spectral density as generated by Mohan.
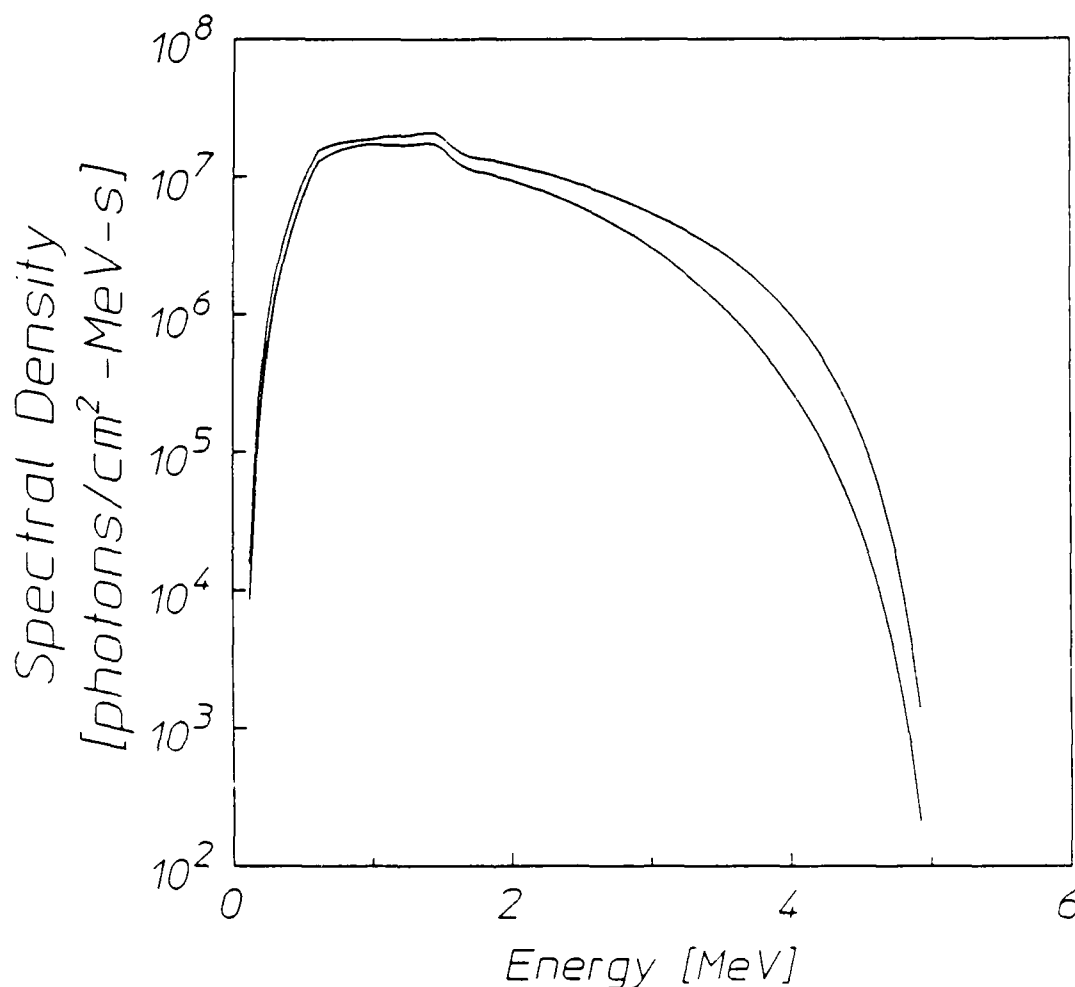
Figure 11: The uncertainty envelope of the compton scattered spectral density at 16° calculated with the extended scatterer/extened absorber geometry.

From the activation data of Table II, the product of cross section and spectral intensity was calculated using Eq. 18. Based on the assumption of a single gateway, a plot of σ_{eff} versus the gateway energy was made for each value of θ by utilizing the modeled spectral intensities and Eq. 17. The family of curves obtained by the employing this procedure for Compton spectrometer angles of 8°, 16°, and 24° is shown in Fig. 12. Also included in this figure is the curve obtained by a similar analysis of the activation due to the direct exposure of the gold sample to the primary beam of the linac.

36
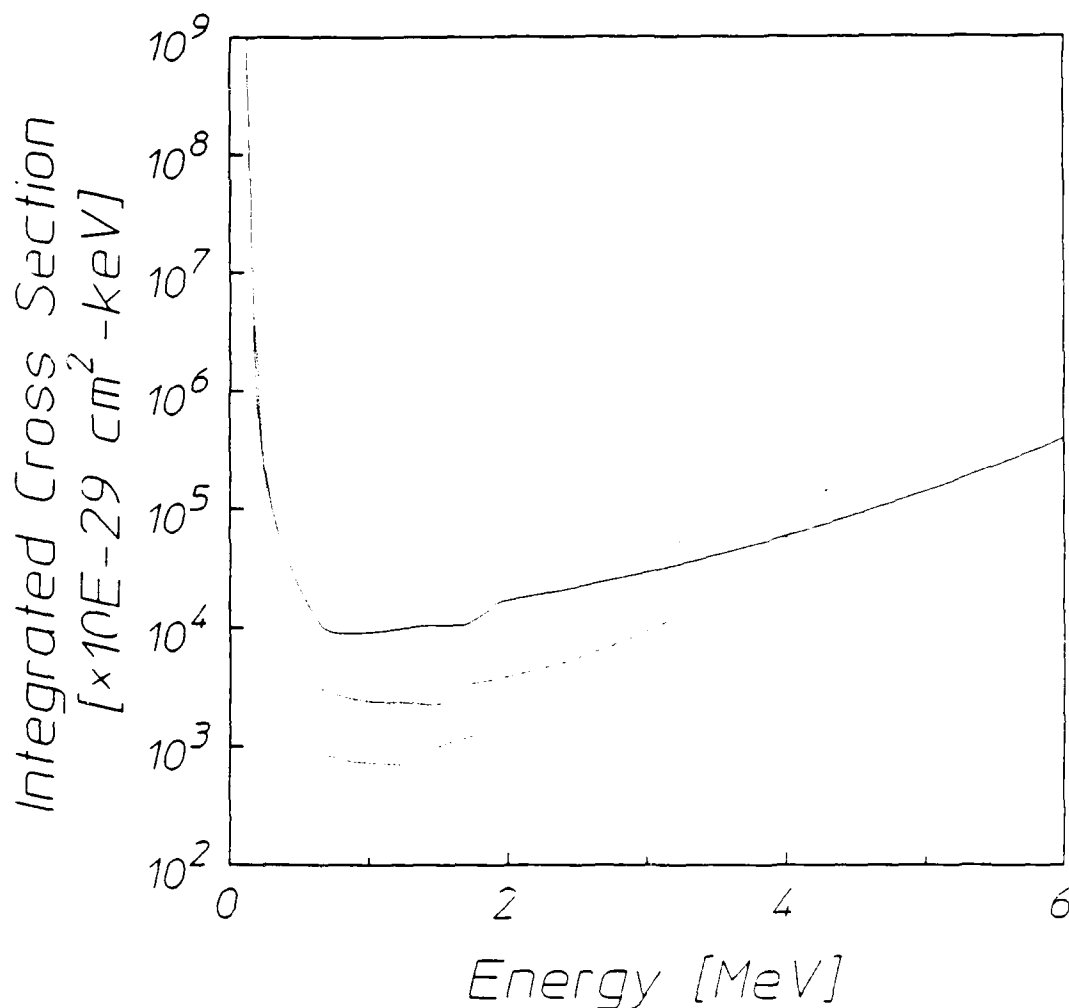
Figure 12: Cross section curves generated from the data taken with the Compton spectrometer and the modelled output spectral densities as shown in Figure 4.

The marked difference between these results and the synthetic curves of Fig. 6 suggests the presence of more than one gateway state, but may be due to experimental uncertainties. The data were analyzed using models incorporating both one and two gateways. In the case of one gateway, there are two unknowns -- the energy E_g and cross section σ for the single gateway -- and four simultaneous non-linear equations of the form

37

$$A_i' = \phi_i(E_g)\sigma \quad , \tag{19}$$

where the A_i' are the activation values of Eq. 15 normalized to the exposure time and the $\phi_i(E_g)$ are the spectral intensities (dI/dE) at the gateway energy E_g. This set of equations was solved using an iterated Marquardt procedure[11], yielding the values $E_g = 3.57 \pm 0.14$ MeV and $\sigma = 42000 \pm 4000 \cdot 10^{-29}$ cm^2-keV.

If two gateway states are assumed to exist, then there are four unknown parameters to be found. These are the energies E_1 and E_2 and cross sections σ_1 and σ_2 associated with the lower and upper gateways. Again, a series of four simultaneous non-linear equations can be written relating these parameters to the observed levels of activation. A set of N simultaneous nonlinear equations in N unknowns may have no real solutions, a single solution, or a degenerate set of solutions. Unfortunately, when a solution was sought using the same Marquardt technique described above, successive iterations did not converge to a set of unique values, but instead produced results that were strong functions of the input estimates for the parameter values. Thus, experimental data at additional values of angle θ would be required to obtain an unique solution for the multi-gateway model.

Conclusions

The Compton spectrometer can be used to determine gateway energies and nuclear photo-activation cross sections when used with a linear accelerator producing a well-characterized continuous spectrum. The complexity of the model which can be used to analyze a given system is limited by the number of angles in the Compton spectrometer for which data are available. Models incorporating more gateway states require data at additional angles.

In the present work, a rudimentary analysis was made of the spectrum produced by the Compton spectrometer. This analysis would tend to underestimate the spectral intensity at lower energies, since it does not properly account for multiple Compton scattering in the spectrometer. Thus, the curves of Fig. 12 should lie lower than shown at the

38

lower photon energies. A comprehensive Monte Carlo transport calcula-
tion is planned to realistically estimate the total scattered spectral
intensity at each of the sample positions.

Preliminary results from this work indicated that if a single
gateway were responsible for the observed activation, the gateway would
lie near 3.6 MeV and have a cross section of 4.2 · 10^{-25} cm²-keV.
Although this is not inconsistent with the results of several other
investigators[12,13], previous work in this Center[14] and by Lukens[15] also
indicates the presence of at least one more gateway in the range between
1 and 3 MeV. Additional experiments with better angular resolution,
statistical accuracy, and spectral characterization should further
improve the understanding of the photoactivation mechanism in ^{197}Au.

While mathematical rigor cannot be maintained at any higher level
of analysis, some further arguments can be presented based on physical
insight. In the first place it must be recalled that the model error is
not estimated by the Marquardt procedure. It was shown above that if
there were only a single gateway within the interval between 1 and 6
MeV, then it would lie near 3.6 MeV. However, if there are two gate-
ways, then neither is constrained to be near that energy.

Since the observation of any large gateways at all below the onset
of the continuum of states was initially surprising, it is reasonable to
propose a model with only a minimal number of them at lower energies.
Lukens[16] reported the excitation of ^{197}Au with bremsstrahlung having an
endpoint energy of 3 MeV. If this activation observed by Lukens is
assumed to be due to a single gateway below 3 MeV, several interesting
conclusions may be drawn.

The intensities for energies above 3 MeV are relatively small for
scattering at θ = 24°, and therefore the corresponding curve for σ in
Fig. 12 approaches the vertical near this energy. Under the assumption
made above, this curve represents the cross section of the single
gateway observed by Lukens as a function of the energy at which it might
lie. The correct choice of the energy can be approximated by consider-
ing the intersection of this curve with those obtained at other angles,
in analogy to the situation shown in Fig. 6.

Wherever the higher energy gateways may lie, the data obtained at
θ = 16° will be that which is least affected by their presence. There-
fore, the intersection near 2.6 MeV of the θ = 16° and θ = 24° curves[16]

39

in Fig. 1/ should give the best approximation to the location of the gateway observed by Lukens. Consistent with this conclusion is the observation that the $\theta = 8°$ curve, which shows elevated cross section values due to activation at higher energies, intersects the $\theta = 24°$ curve near 3 MeV. If the $\theta = 8°$ curve were corrected by removing the contributions of the higher gateways, the shape of the curve would be preserved, but its location would be translated downward on the plot of Fig. 12. This would shift the intersection down from 3 MeV toward the 2.6 MeV value noted above.

Of course, the $\theta = 16°$ curve may also carry some contamination from higher gateways and thus require a similar downward correction if the effects of the upper gateways were to be removed. The extent of this correction cannot be determined, but its presence insures that 2.6 MeV is an upper limit for the energy of the assumed single gateway. Moreover, reference to Fig. 12 shows that below 1.5 MeV the cross section required by the $\theta = 24°$ curve is $1000 \cdot 10^{-29}$ cm^2-keV or more, which is much greater than the values[15] obtained using the PITHON bremsstrahlung source operated with a 1.5 MeV endpoint energy. Thus, the gateway must be bracketed by these two points.

While the rigorous resolution of the merits of this interpretation must await additional data, there seems to be a strong argument that the gateway originally observed by Lukens lies near 2.6 MeV. This result has an interesting precedent in the literature[17] that has largely been ignored as an anomaly. This is the discrete gateway for the reaction $^{87}Sr(\gamma,\gamma')^{87}Sr^m$, having an integrated cross section of $430 \cdot 10^{-29}$ cm^2-keV at 2.66 MeV. This cross section was about one and a half orders of magnitude greater than any other reported for a discrete gateway and has remained unexplained for 20 years. Now it appears that there is a second such example in $^{197}Au(\gamma,\gamma')^{197}Au^m$.

Acknowledgements

References

1. C. B. Collins, C. D. Eberhard, J. W. Glesner, and J. A. Anderson, Phys Rev C $\underline{37}$, 2267 (1988).

2. C. D. Eberhard, J. W. Glesener, Y. Paiss, J. A. Anderson, C. B. Collins, W. L. Hodge, E. C. Scarbrough, and P. P. Antich, Report GRL/8702, 89 (1987).

3. C. B. Collins, J. A. Anderson, C. D. Eberhard, J. F. McCoy, J. J. Carroll, E. C. Scarbrough, and P. P. Antich, Report GRL/8703, 37 (1988).

4. J. A. Anderson, C. D. Eberhard, J. F. McCoy, K. N. Taylor, J. J. Carroll, M. J. Byrd, C. B. Collins, E. C. Scarbrough, and P. P. Antich, Report GRL/8704, 11 (1988).

5. R. D. Evans, "Gamma Rays" in American Institute of Physics Handbook, ed. D. E. Gray (McGraw-Hill, New York, 1963).

6. R. Mohan, C. Chui, and L. Lidofsky, Med. Phys. $\underline{12}$, 592 (1985).

7. N. C. Ikoro, D. A. Johnson, and P. P. Antich, Med. Phys. $\underline{14}$, 93 (1987).

8. Y. Paiss, C. D. Eberhard, and C. B. Collins, Report GRL/8702, 71 (1987).

9. C. B. Collins, J. A. Anderson, Y. Paiss, C. D. Eberhard, R. J. Peterson, W. L. Hodge, Phys. Rev. C (accepted for publication).

10. J. A. Anderson, M. J. Byrd, and C. B. Collins, Phys. Rev. C (accepted for publication).

11. W. H. Press, B. P. Flannery, S. A. Teukolsky, and W. T. Vettering, Numerical Recipes, (Cambridge University Press, Cambridge, 1986).

12. W. T. K. Johnson and C. E. Dick, Nucl. Instr. and Meth. $\underline{99}$, 221 (1972).

13. Zs. Nemeth, L. Lakosi, I. Pavlicsek, and A. Veres, Appl. Radiat. Isot. $\underline{37}$, 1155 (1986).

14. C. B. Collins and J. A. Anderson, Report GRL/8701, 35 (1987).

15. H. R. Lukens, Jr., J. W. Otvos and C. D. Wagner, Int. J. Appl. Radiat. and Isot. 11, 30 (1961).

16. The results shown in Fig. 12 and discussed in this chapter are the current values at press time, and are somewhat larger than preliminary values used elsewhere in this report.

17. E. C. Booth and J. Brownson, Nucl. Phys. A 98, 529 (1967).

LIMITS ON NEUTRON ACTIVATION INTERFERENCES IN PHOTOACTIVATION CROSS-SECTION MEASUREMENTS IN THE 1.5-6 MeV RANGE

by J. A. Anderson, C. D. Eberhard, J. J. Carroll, M. J. Byrd,
and C. B. Collins
Center for Quantum Electronics, University of Texas at Dallas
and E. Scarbrough and P. P. Antich
University of Texas Southwestern Medical Center

Introduction

Recent measurements[1-4] have indicated that (γ,γ') cross sections at energies between 1.5 and 6 MeV may be three orders of magnitude or more greater than corresponding cross sections at lower energies. Since the high-energy photons used in these experiments can also produce neutrons through (γ,n) reactions, it is necessary to rule out contamination of the (γ,γ') cross section results by this incidental neutron field. This study establishes limits on the contributions of neutron reactions in previous experiments. Two basic approaches can be made toward this end: quantifying contributions from known neutron sources and making independent measurements of the neutron flux. Both approaches have been taken in this work and have been compared for mutual agreement. On the basis of this study, neutron-induced interferences are at least two to three orders of magnitude less than the observed isomeric activity due to photoexcitation.

Neutron Interference in Photoactivation Measurements

Two types of interfering neutron reactions can affect nuclear photoactivation studies on isomeric nuclei. The first is excitation of the isomer through (n,n') processes that populate the isomer either directly or through cascades from higher lying states. This, of course, requires neutrons with energies greater than the energy separation between the ground and isomeric states. All isomers can be excited

43

through the (n,n') process. which typically has a cross section on the order of several hundreds of millibarns. A summary of the isomers studied in references 1-4 is given in Table I. Note that $^{77}Se^m$, the lowest lying isomer which was excited from the ground state, requires a minimum neutron energy of 162 keV to initiate an (n,n') reaction. Measured integrated cross sections for isomeric photoactivation have been included in Table I. These values have been updated from previous reports to include additional trials and improved instrumental parameters. Because the earlier technique does not permit identification of a unique photoactivation gateway, a hypothetical single gateway at 2.125 MeV has been used to calculate the cross section values listed here. These values can be adjusted to other assumed gateway energies by using the spectrum of the bremsstrahlung source employed in these experiments[5,6] which is shown in Fig. 1. If the relative intensity of the source at 2.125 MeV is $\phi(2.125)$ and if the intensity at the desired energy E is $\phi(E)$, then the adjusted value for the cross section is given by

$$\sigma(E) = \sigma(2.125 \text{ MeV}) \times [\phi(2.125)/\phi(E)] \qquad (1)$$

Values for the ratio $\phi(2.125)/\phi(E)$ are tabulated in Table II.

Isomeric states can also be populated by neutron capture in the isotope having one less neutron than the isomer. This can occur through capture in either the resonance or thermal regions. For example, when neutron capture occurs in the 1.46 eV resonance of ^{115}In, there is an 79.5% probability of populating the 127 keV ($T_{1/2}$ = 54.1 min) isomer in ^{116}In. The remainder of the capture products populate[8] the ground state ($T_{1/2}$ = 14.1 s) of ^{116}In. In contrast, thermal neutron capture in ^{115}In can produce not only the $T_{1/2}$ = 54.1 min and $T_{1/2}$ = 14.1 s activities. but also $T_{1/2}$ = 2.16 s activity[9] from the 290 keV isomer in ^{116}In. This second, short-lived isomer decays to the 127 keV isomeric level through emission of a 162 keV photon.

44

Table I

Isomers studied in current investigations. Values for the nuclear parameters are taken from reference 7. Values for $\sigma\Gamma(2.125)$, the integrated cross section for an assumed gateway state at 2.125 MeV, are taken from the work of references 1-4. In some cases, the cross sections have been updated from the previous values to reflect new data. When multiple trials or sample counts were available, the standard deviation of the mean has been given for the $\sigma\Gamma$ value.

Isomer	Ground State Abundance (%)	Energy (MeV)	Isomeric Halflife		J_g	J_i	$\sigma\Gamma(2.125)$ $(10^{-29}$ cm^2-keV)
^{77}Se^m	7.6	0.162	17.45	s	1/2-	7/2+	7810
^{79}Br^m	50.69	0.207	4.864	s	3/2-	9/2+	2180
^{87}Sr^m	7.0	0.388	2.81	h	9/2+	1/2-	1004 ± 6
^{89}Y^m	100.0	0.909	16.06	s	1/2-	9/2+	296
^{111}Cd^m	12.8	0.396	48.6	m	1/2+	11/2-	3300 ± 480
^{113}In^m	4.3	0.392	1.658	h	9/2+	1/2-	5000 ± 260
^{115}In^m	95.7	0.336	4.486	h	9/2+	1/2-	6700 ± 620
^{117}Sn^m	7.68	0.315	13.61	d	1/2+	11/2-	1050 ± 70
^{123}Te^m	0.91	0.247	119.7	d	1/2+	11/2-	8100 ± 200
^{135}Ba^m	6.59	0.268	28.7	h	3/2+	11/2-	6520 ± 110
^{137}Ba^m	11.74	0.662	2.5513	m	3/2+	11/2-	2120
^{167}Er^m	22.95	0.208	2.28	s	7/2+	1/2-	43200
^{179}Hf^m	13.63	0.375	18.68	s	9/2+	1/2-	31000 ± 500
^{180}Ta^m	0.00	0.032	1.2×10^{15}	y	1+	9-	49000
^{183}W^m	14.3	0.309	5.15	s	1/2-	11/2+	2220
^{191}Ir^m	37.3	0.171	4.94	s	3/2+	11/2-	41400
^{195}Pt^m	33.8	0.259	4.02	d	1/2-	13/2+	20900 ± 1200
^{197}Au^m	100.0	0.409	7.8	s	3/2+	11/2-	15300 ± 1100
^{199}Hg^m	16.84	0.532	42.6	m	1/2-	13.5+	1849 ± 45
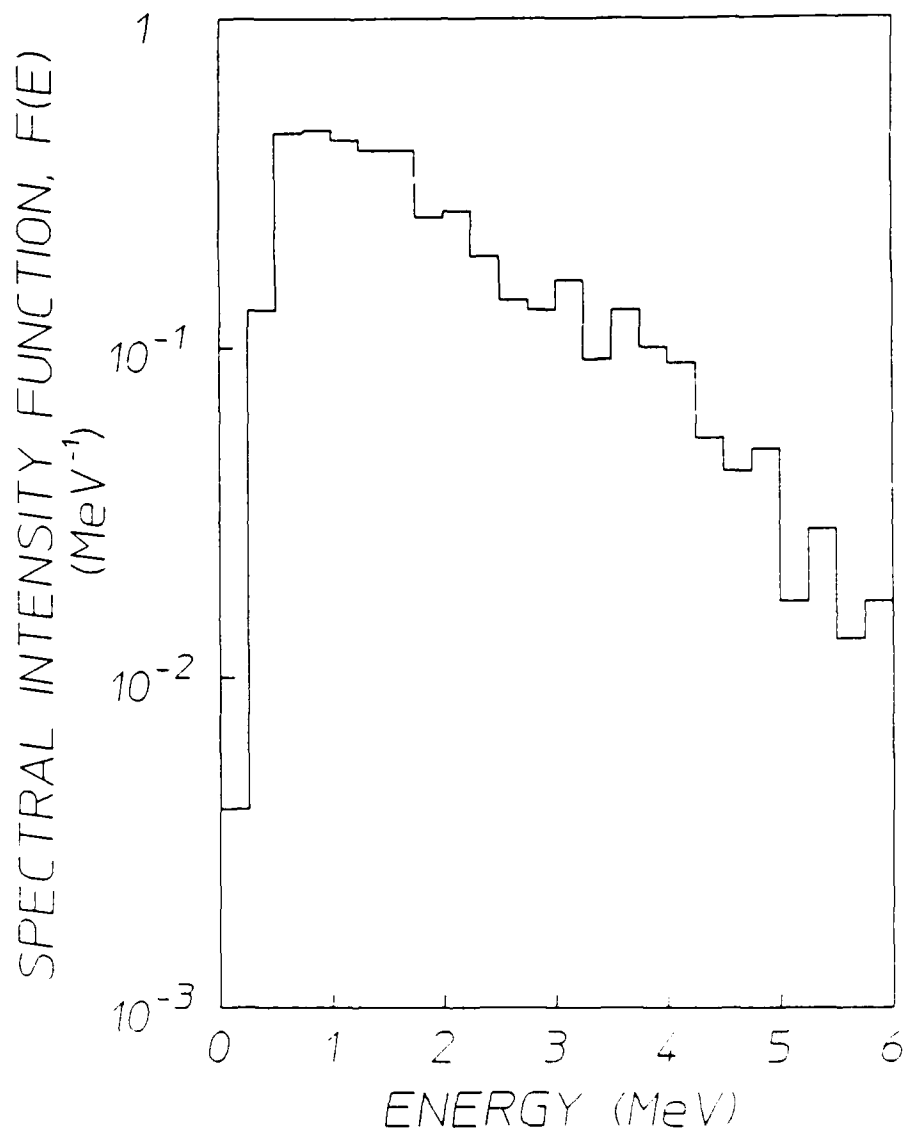
Figure 1: Relative spectral intensity for the bremsstrahlung used in the experiments of references 1-4. The values have been normalized so that the integral under the curve is unity.

Table II

Ratios of the photon intensities at energies E to that at 2.125 MeV for the spectrum shown in Fig. 1.

Energy	$\phi(2.125)/\phi(E)$ [MeV]
0.125	0.015
0.375	0.500
0.625	1.731
0.875	1.769
1.125	1.654
1.375	1.538
1.625	1.538
1.875	0.962
2.125	1.000
2.375	0.731
2.625	0.538
2.875	0.500
3.125	0.615
3.375	0.354
3.625	0.500
3.875	0.385
4.125	0.346
4.375	0.204
4.625	0.162
4.875	0.188
5.125	0.065
5.375	0.108
5.625	0.050
5.875	0.065

Capture cross sections are quite small at high energy, but can be thousands of barns in the resonance and thermal energy regimes. However, in the experiments described in references 1-4, interference from this process requires that both the isotope undergoing capture and the ground state of the isomer be naturally occurring nuclides. A list of isomers from Table I satisfying this criterion and their appropriate capture cross sections is given in Table III.

Table III

Isomers susceptible to (n,γ) interferences and the isotopes which would produce them through neutron capture. The natural abundances of the capturing species are shown. Cross sections for total thermal capture (σ_T), thermal capture to the isomer $(\sigma_{T,I})$, total resonance capture (σ_R), and resonance capture to the isomer $(\sigma_{R,I})$ are listed.[9]

Isomer	Isotope	Natural Abundance[7] (%)	σ_T (b)	$\sigma_{T,I}$ (b)	σ_R (b)	$\sigma_{R,I}$ (b)
$^{77}Se^m$	^{76}Se	9.00	85	21.00	42	17
$^{87}Sr^m$	^{86}Sr	9.86	0.84	0.84	5	5
$^{111}Cd^m$	^{110}Cd	12.49	11.1	0.10	42	2
$^{117}Sn^m$	^{116}Sn	14.53	0.11	0.01	11.5	0.5
$^{123}Te^m$	^{122}Te	2.60	3		80	
$^{135}Ba^m$	^{134}Ba	2.42	2.16	0.16	20	
$^{137}Ba^m$	^{136}Ba	7.85	0.41	0.01	1.6	
$^{167}Er^m$	^{166}Er	33.60	20	15.00	100	
$^{179}Hf^m$	^{178}Hf	27.30	80	50.00	1900	
$^{183}W^m$	^{182}W	26.30	21		600	
$^{195}Pt^m$	^{194}Pt	32.90	1.2	0.10	4	
$^{199}Hg^m$	^{198}Hg	10.02	1.92	0.02	70	

Photoneutron Sources

The approximate threshold energy E_t for a (γ,n) reaction can be calculated from

$$E_t = \delta n + \delta(A-1,Z) - \delta(A,Z) \quad , \quad (2)$$

where $\delta(A,Z)$ is the mass excess for the nuclide characterized by atomic number Z and mass number A, and δn is the mass excess for the neutron. The value calculated in this way does not include the correction necessitated by the recoil of the absorbing nucleus, but this is insignificant ($\ll 1\%$) in practice.

For monochromatic incident photons, neutrons produced by a (γ,n) reaction will also be nearly monochromatic because the momentum of the incident photon is very much less than that of the target nucleus. Part of the decay energy of the compound nucleus will be carried away by the recoil nucleus, resulting in the neutron energy, $E_n(\theta)$, being given[10] approximately by

$$E_n \approx \frac{M(E_\gamma - E_t)}{m + M} + \frac{E_\gamma[(2mM)(m + M)(E_\gamma - E_t)]^{1/2}}{(m + M)^2} \cos \theta \quad , \quad (3)$$

where

θ = angle between the momentum vectors of the incident photon and emitted neutron,

E_γ = incident photon energy,

M = rest mass of recoil nucleus in energy units, and

m = rest mass of neutron in energy units = 938 MeV.

The second term, which contains the angular dependence of Eq. 3, is no more than 10% of the first term for the cases considered here and will be neglected in the following analysis.

Fast Neutron Contributions from Known Sources

The approximate neutron source spectrum and integrated neutron production rate for a given (γ,n) reaction can be calculated from the

incident photon spectrum using Eq. 3. Assuming that the target material is optically thin, the number N_n of neutrons produced in the range E_n to $E_n + \delta E_n$ from a sample of N_T target nuclei will be given by

$$N_n(E_n) = N_T \phi(E_\gamma)\phi(E_\gamma) \ T \ \delta E_\gamma \qquad \qquad (4)$$

where $\sigma(E_\gamma)$ is the (γ,n) cross section, $\phi(E_\gamma)$ is the spectral intensity in units of photons/cm^2-keV, T is the irradiation time, and $\delta E_n = \delta E_\gamma \times [M/(M + m)]$. The integrated production rate for all neutrons above a given energy E_n' is then simply

$$R_n(E_n') = N_n(E_n')/T = N_T \times \int_{E_{\gamma 0}}^{E_{max}} \sigma(E_\gamma)\phi(E_\gamma)dE_\gamma \qquad \qquad (5)$$

where $E_{\gamma 0} = E_t + (1 + m/M)E_n'$.

High energy photons for the previous photoactivation studies were obtained from the bremsstrahlung output of a Varian CLINAC 1800 linac normally used for medical therapy. This source has been well character-ized,[5,6] and its spectrum is shown in Fig. 1. The intensity reaches a maximum near 1 MeV and then drops by a factor of about thirty as it approaches its cut-off at 6 MeV. Therefore, the only neutron production mechanisms that are relevant are (γ,n) reactions with thresholds less than 6 MeV. A list of naturally occurring materials meeting this criterion is given in Table IV. Only these materials could serve as neutron sources in the experiments considered here. Several of them are rare and are not present in the linac construction or in its environ-ment. The exceptions are ^{2}H, ^{9}Be, ^{13}C, and ^{17}O. Deuterium occurs as coolant water in the machine and as bound water in the concrete shield-ing of the irradiation cell. Beryllium is present in the beam exit window in the linac head. The other two possible contributors, ^{13}C and ^{17}O, occur in the atmosphere and in the shield walls of the linac cell. The cross sections[11] for ^{2}H and ^{9}Be are on the order of a few millibarns in the range between their reaction thresholds, near 2 MeV, and the maximum photon energy at 6 MeV. The thresholds for ^{13}C and ^{17}O are both above 4 MeV. The cross sections for these two nuclides are poorly known at such low energies, but may safely be assumed to be considerably less than a millibarn.[12,13]

Table IV

Naturally occurring materials with (γ,n) thresholds less than 6 MeV.
The neutron energies, $E_{n,max}$, for neutrons ejected by 6 MeV photons were
calculated neglecting the angular term in Eq. (3). The neutron binding
energy, B_n, has been taken from reference 14.

Material	Natural Abundance (%)	B_n (keV)	$E_{n,max}$ (keV)
^2H	0.015	2224.6	1886.764
^6Li	7.5	5662	281.3626
^9Be	100	1665.1	3849.664
^{13}C	1.1	4946.5	971.7887
^{17}O	0.038	4142.5	1747.277
^{145}Nd	8.3	5760.4	237.9317
^{149}Sm	13.8	5846.2	152.7579
^{235}U	0.72	5307	690.0251

In the linac head itself, Be in the 0.025 cm thick beam window will
be the dominant contributor to the neutron field. This is true because
Be occurs monoisotopically as ^9Be, and has both a lower threshold energy
(1.665 MeV vs 2.224 MeV) and a larger (γ,n) cross section averaged over
the bremsstrahlung spectrum than ^2H. The beam window is located approxi-
mately 6 cm from the converter target and is illuminated over a diameter
of about 3 cm. It comprises about 2.4×10^{22} ^9Be nuclei. Under equiva-
lent irradiation conditions, almost 3 liters of normal water would be
required to produce the same number of neutrons from the $^2H(\gamma,n)H$
reaction. This is far in excess of the several milliliters of water
actually in the target cooling loop at any one time. Thus, for neutrons
originating in the linac head, only those from the Be window are
significant.

51

Under the assumptions that the photoneutrons are emitted isotropi-
cally from the Be foil[15] and that the foil dimensions are small compared
to r, the source-sample distance, one obtains

$$\phi_n(E_n') = R_n(E_n')/(4\pi r^2) \qquad\qquad (6)$$

for $\phi_n(E_n')$, the intensity at the sample position of neutrons with $E_n \geq E_n'$. The results for a sample located at the position normally used for
the work in references 1-4 are shown in Fig. 2. Note that the neutron
intensity at the sample location due to this source is only 1000
$n/(cm^2\text{-s})$, about 7 orders of magnitude less than the corresponding
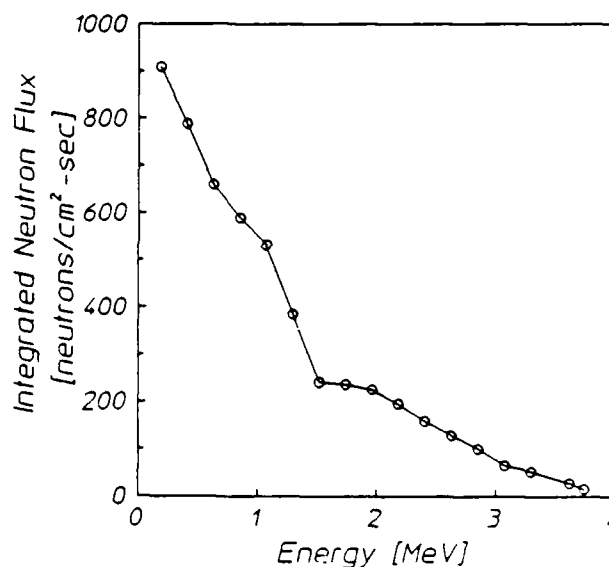integrated pnoton flux.

Figure 2: Calculated net neutron flux
above the neutron energy E_n' at a distance
of 65 cm from the bremsstrahlung source
used for the work of references 1-4.

Neutron production due to (γ,n) reactions with ^2H, ^{13}C, and ^{17}O in
the air is limited by the low density of the target nuclei, and, in the
case of the last two materials, by small (γ,n) cross sections. If the
x-ray output is assumed to pass through a conical volume with semi-angle
$\theta_c = 8.75°$ --corresponding to the typical conditions of a field width of
20 cm at a sample distance of 65 cm -- then the volume of irradiated air

52

between the converter target and the floor is about 2.99×10^5 cm^3. The standard atmosphere[16] comprises 20.95% oxygen and 0.0314% carbon dioxide by volume. Using natural abundances of 0.038% and 1.1%, one obtains about 1.3×10^{21} atoms of ^{17}O and 2.8×10^{19} atoms of ^{13}C in the irradiated volume. A similar calculation for deuterium in the case of 100% relative humidity (T = 300 K) yields a result of 7.71×10^{19} ^{2}H atoms in the volume. Therefore, there are at least ten times more (γ,n) targets in the Be exit window on the linac than there are in the entire irradiated volume in the atmosphere. Moreover, most of the atmospheric targets occupy the bottom half of the cone, where the $1/r^2$ decrease in the photon beam intensity will have reduced the irradiation level by more than two orders of magnitude. As a result of these two conditions and the small cross sections for ^{17}O and ^{13}C, the atmospheric contribution to neutron production through the (γ,n) process is negligible compared to neutron production in the linac head itself.

The final possible source of neutrons in the linac environment is the concrete floor of the irradiation cell. Because an exact analysis of the concrete in place was not available, the typical composition[17,18] of concretes used in standard construction practice in this area was used to estimate the neutron production from this source. For a bulk density of 2.62 g/cm^3, atomic concentrations for the materials of interest were found to be as follows:

$$N(^2H) = 1.59 \times 10^{18} \text{ cm}^{-3} \quad ,$$

$$N(^{13}C) = 8.16 \times 10^{19} \text{ cm}^{-3} \quad , \text{ and}$$

$$N(^{17}O) = 1.91 \times 10^{19} \text{ cm}^{-3} \quad .$$

Since the mass attenuation coefficient for a 6 MeV photon in concrete is about[19] 0.027 cm^2/g, the relaxation length for photons entering the floor slab is 14 cm. The neutrons created in the concrete obviously must escape the floor before being captured if they are to participate in (n,n') or (n,γ) processes in the sample, and therefore it is required that that contributing targets must lie within about 1 neutron migration length from the surface of the floor.[20] The neutron migration length is the sum, in quadrature, of the neutron slowing down length and the thermal diffusion length, and it can be considered to be the average straight line distance traveled between emission and thermalization of the neutron. For the composition model being used, the migration length for a 2 MeV neutron is 14 cm.[21] Thus, it is reasonable for the purposes of estimating the neutron flux from interac-

tions in the floor to assume that the neutrons originate in a cylindrical slab which is 15 cm thick and has the same diameter (d = 50.6 cm) as the beam envelope at floor level. Using Eq. 6, the estimated neutron flux at the sample position can be calculated for each of the species in the slab. The (γ,n) cross sections for ^{13}C and ^{17}O were assumed to have a constant value of 1 mb above the threshold energies; this represents a substantial overestimation. Measured cross sections[13] for ^{2}H were used. The results for the neutron fluxes produced by the different target nuclides are as follows:

$$\phi_n(^2H) = 0.08 \text{ n/cm}^2\text{-sec} \quad ,$$

$$\phi_n(^{13}C) = 0.8 \text{ n/cm}^2\text{-sec} \quad , \text{ and}$$

$$\phi_n(^{17}O) = 0.5 \text{ n/cm}^2\text{-sec} \quad .$$

As in the case of the atmospheric contributions, the contributions from the irradiation cell floor are insignificant compared to those from the Be beam window. Only the neutron flux produced by the Be window will be considered in the following analysis of contamination limits.

Contamination limits for the integrated cross sections listed in Table I could be directly determined from the integrated neutron flux shown in Fig. 2 and the appropriate cross sections for the (n,n') processes. Unfortunately, not all of the cross sections are known. To present the results of this study in a usable form even when the cross section data is not available, an alternate approach was chosen. For each of the materials in Table I, the (n,n') cross section that would be required to produce an arbitrary fraction f of the observed activation was calculated. A value of 100% was used for f in this work. The resulting cross sections have been compared with known (n,n') cross sections or other limiting cross sections, such as the total neutron cross section, when possible.

The (n,n') cross section necessary to produce the observed isomeric activation, $\sigma_{n,100\%}$, was obtained using the expression

$$\sigma_{n,100\%} = \frac{N_m}{N_T \, \phi_n(E_n') \, T} \quad , \tag{7}$$

which follows from the assumption of negligible self-absorption effects. In this equation, N_m is the total number of isomers activated in the course of the irradiation, T is the time of the irradiation, and N_T is the number of ground state nuclei of the material of interest. A value

54

of $E_n' = 0$ was employed to evaluate Eq. 7, thus insuring that the minimum cross section value required would be obtained. Note that since the photoactivation cross section is obtained[1-4] from

$$(\sigma\Gamma)_\gamma = \frac{N_m}{N_T\phi_\gamma(E_\gamma)T} \qquad , \qquad (8)$$

the hypothetical neutron cross section required to produce the observed activation is related to the reported photon cross section by

$$\sigma_{n,100\%} = \frac{(\sigma\Gamma)_\gamma\phi_\gamma(E_\gamma)}{\phi_n(E_n')} \qquad . \qquad (9)$$

The (n,n') reaction cross sections which would have been necessary to produce the observed activations were calculated using Eq. (7) and have been tabulated as $\sigma_{n,100\%}$ in Table V. The actual total neutron cross sections and, where available, the non-elastic cross sections are also listed in Table V for the elements studied in references 1-4. Literature values for the true (n,n') cross sections for the selected isotopes are listed for those cases in which they are available. The actual (n,n') cross sections are on the order of several hundreds of millibarns or less. Some of the (n,n') cross sections listed in Table V are averages weighted against a fission spectrum. Although the fission spectrum is peaked at lower energies than the Be photoneutron spectrum whose integrated intensity is shown in Fig. 2, it still has significant intensity ($\approx 1/3 \ I_{max}$) near 1 MeV, the point below which about half of the Be photoneutron intensity lies. Comparison of the (n,n') cross sections which would have been required account for the observed amounts of activation with the sizes of cross sections actually prevailing indicates that in all cases the neutron contamination is substantially less than 10%. The parameter Ω shown in Table V is the ratio of the best observed limiting cross section to $\sigma_{n,100\%}$. If the (n,n') cross section was available, then Ω was calculated using it; if not, then the non-elastic or total cross section was used. Thus, Ω always either equals or overestimates the ratio of the amount of true (n,n') induced activity to 100% of the observed activity in the photoactivation experiments, and thus it represents the fraction of fast neutron contamination expected in the photoactivation results. As can be seen from the table, Ω ranges from 0.0002 to about 0.06, corresponding to contamination limits for the photoexcitation results of between 0.02% and 6%. The maximum value of 6% occurs in the case of ^{79}Br, for which

55

only the total neutron cross section, rather than the smaller (n,n′) cross section, was available. For the materials for which realistic values of the (n,n′) cross section were available, the maximum fast neutron contribution to the observed isomeric activation is much less than 1%, based on an examination of all potential sources of fast neutrons in the experimental environment. This indicates that activation via the (n,n′) reaction is not a significant process in the photoactivation studies being considered here.

Fast Neutron Flux Measurements

Measurement of such low neutron fluxes as the analysis above yielded at the sample position is difficult in the presence of an intense photon field. Although neutron counters based on the ^{10}B(n,α) reaction or on the ^{3}He(n,p) reaction have some gamma-ray rejection capabilities, they are inadequate for the experimental situation encountered in this work. Boron counters are more robust than ^{3}He proportional tubes and can operate in gamma fields up to about 1000 R/hr, but the gamma field at the sample position in these experiments is about 60 times higher than this. Moreover, these counters are principally sensitive to thermal neutrons, and a moderator must be used to thermalize incident fast neutrons. Since the two most common and effective moderators are H and C, both potential sources of photoneutrons, there is also the possibility of creating a considerable perturbation in the neutron flux by introducing the detector.

56

Table V

Neutron cross sections required to produce 100% of the observed activation in previous photoexcitation studies[1-4]. Maximum values for the true total neutron cross section of the element of interest, σ_{el}, are shown for the energy range 0.1-6 MeV. When available, the non-elastic cross section for the element has been shown in parentheses following the total cross section. The most restrictive additional cross section, σ_{lim}, for the particular isotope or element is given with its type and E_{max}, the energy up to which it was determined. Cross section types are as follows: ie - inelastic in element; i - inelastic in isotope; n - non-elastic in isotope; fi - inelastic in isotope, average for fission spectrum. The factor Ω is the ratio of the most specific observed cross section to the cross section required for a 100% contamination effect, and thus represents an upper limit for contamination of the reported photoactivation cross section by neutron effects.

Isomer	$\sigma_{n,100\%}$ (b)	σ_{el} (b)	σ_{lim} (b)		Type	E_{max} (MeV)	Ω (%)
^{77}Se	490	8.3(2.4)	0.73	24	fi	-	0.15
^{79}Br	140	7.5					5.4
^{87}Sr	60	10	0.11	24	fi	-	0.18
^{89}Y	20	11.5	0.2	25	i	4.0	1.0
^{111}Cd	210	8	0.23	24	fi	-	0.11
^{113}In	320	6.3	0.047	26	i	1.0	2.0
^{115}In	430	6.3	0.38	27	i	5.3	0.088
^{117}Sn	70	6.8(2)					2.8
^{123}Te	530	6					1.1
^{135}Ba	420	7.3(2)					0.48
^{137}Ba	130	7.3(2)	0.66	28	i	3	0.51
^{167}Er	2700	9					0.33
^{179}Hf	1940	20	0.4	29	i	1.6	0.02
^{180}Ta	3016	8.5(2.9)	1.8	30	ie	1.8	0.06
^{183}W	140	9.3(2.4)	0.93	30	ie	1.7	0.66
^{191}Ir	2590	10.3					0.40
^{195}Pt	1350	10	0.68	30	ie	1.0	0.05
^{197}Au	95	10	1.3	30	i	5.3	0.14
^{199}Hg	120	10(2.6)	0.14	31	i	2.1	0.12

Another common approach to making fast neutron measurements is the use of neutron activation foils. Unfortunately, some of the most sensitive threshold reactions[33,34], are either (n,n') inelastic scattering reactions or (n,f) fission reactions, which can suffer from (γ,γ') or (γ,f) reaction interferences. However, other foils can be selected that have lower sensitivities but which are relatively free of photon induced interferences. A foil activation experiment was conducted to corroborate the results in the previous section and to verify that no significant neutron sources had been omitted from that analysis. Although the sensitivity of the experiment was inadequate to detect neutrons at the very low levels expected, it demonstrated that there were no unexpected neutron sources of significance in the environment.

Threshold detectors, commonly in the form of activation foils, have long been employed in the determination of neutron spectra. The techniques necessary for such measurements are well documented.[35] The practice is to expose a set of thin foils to the neutron flux in question. The materials of these foils are chosen to be sensitive to neutrons through a variety of reactions, such as (n,n'), (n,p), (n,2n) and (n,np). When the products of these reactions are sufficiently long-lived the activation due to each reaction can be easily measured. The number of activated nuclei produced, N_e, is given by

$$N_e = NT \int_0^\infty \sigma(E)\phi_n(E)dE \quad , \quad (10)$$

where N is the number of target nuclei, T is the irradiation time, $\sigma(E)$ is the reaction cross section, and $\phi_n(E)$ is the neutron spectral density at energy E. For a given material, each reaction occurs only when incident neutrons possess a kinetic energy greater than a particular threshold value. Thus each reaction can be thought of as sampling only the part of the total neutron spectrum which lies above the reaction's threshold, E_t. For this reason, Eq. 10 is often written as

$$N_e = NT\sigma_{eff} \int_{E_t}^\infty \phi_n(E)dE \quad , \quad (11)$$

58

where σ_{eff} is the effective reaction cross section[35] and E_t is the threshold for the reaction. To determine a complete neutron spectrum, it is necessary to use a number of materials with different thresholds and to deconvolve the effects on all of these materials of neutrons in successively lower energy groups. The numerical procedure which used to accomplish this is called an unfolding.[36]

The experiment performed to determine the neutron flux present in the vicinity of the CLINAC 1800 operating in the 6 MeV photon mode employed Ti and Ni as foil materials. These were chosen for a variety of reasons. First, no naturally occurring isotopes of these elements possess isomeric states, so no (γ,γ') activation could occur. Next, (γ,n) and $(n,2n)$ reactions were not accessible since the threshold energy required for each exceeded that available from the linac. For those processes which were energetically possible, many had long lifetimes, important in our experiment. Finally, the thresholds of these reactions occurred at energies well suited for examining the energy range of interest. A summary of relevant properties of the reactions considered is given in Table VI.

Table VI

Accessible reaction properties for naturally abundant isotopes present in the chosen materials.[37]

Reaction	Daughter Halflife (d)	Signature Photon Energy (keV)
$^{46}Ti(n,p)^{46}Sc$	83.83	889.25
		1120.51
$^{47}Ti(n,p)^{47}Sc$	3.34	159.38
$^{58}Ni(n,p)^{58}Co$	70.92	810.79

The Ti and Ni foils were in the form of disks having radii of 2.54 cm and 0.65 cm and thicknesses of 0.005 cm and 0.025 cm. Two disks of each element were employed, with one disk of each encased in a Cd cover

to suppress activation due to thermal neutrons. All four disks were irradiated simultaneously at a distance of 65 cm from the bremsstrahlung converter and were oriented with their axes parallel to the direction of the beam. At the conclusion of a one hour irradiation, the samples were counted individually with a high purity germanium spectrometer system to determine the activation of the foils.

In general, for any peaks evident in the measured gamma-ray spectra which correspond to signature photons of reaction products, it is possible to determine the number of excited nuclei in each foil according to

$$N_e = \frac{C}{\eta f D A} \quad . \tag{12}$$

Here, C is the total number of counts observed within a peak, and η, f, D and A are the corrections for detector efficiency at the energy of interest, gamma ray intensity, finite duration of both irradiation and counting intervals, and self-absorption. This information can then be used in the unfolding process described above to make a determination of the neutron spectrum.

However, in the spectra obtained in this experiment no peaks were detectable above the level of the background, and a direct deconvolution could not be made. Instead, an upper bound for the neutron flux was determined by calculating the maximum number of counts in the signature photon peak which could have been hidden by the statistical variation of the background. The maximum number of excited nuclei was then found from Eq. 12. An upper bound for the neutron flux was then found with Eq. 11 for each reaction. These results are shown in Table VII, together with values of σ_o and E_t.

Table VII indicates that the (n,p) reaction on ^{58}Ni in the Cd covered foil provides the least upper bound for the neutron flux above 2.8 MeV, 9.72×10^3 n/cm^2-sec. Consideration of the spectrum of Fig. 2 implies the total neutron flux can be estimated from that above 2.8 MeV by increasing the value by a factor of 8. The neutron flux at the sample position must then be less than or equal to the maximum level of undetected neutrons in this experiment, 6.98×10^4 n/cm^2-sec. This is about two orders of magnitude greater than the limits obtained in the previous section; thus the experiment has inadequate sensitivity to

60

closely verify the preceding neutron source analysis, but does rule out the presence of significantly large sources which had not been included in that analysis. It should be noted that even the worst case neutron flux derived from this experiment would have only a small effect on the production of isomeric states through (n,n′) reactions. For the case of $^{115}In^m$, a value for $(\sigma\Gamma)$ at 2.125 MeV of 6700×10^{-29} cm²-keV can be taken from Table I. With a photon flux incident on a sample at a distance of 65 cm of 5.7×10^6 photons/cm²-keV-sec at 2.125 MeV and the maximum neutron flux taken from above, Eq. 9 indicates that an inelastic neutron scattering cross section of 5470 mb would be required to produce the observed amount of activation. Since the literature value from Table V is 380 mb, in this worst case scenario less than 10% of the observed isomeric activation could have been due to inelastic neutron processes.

Table VII

Calculated upper bounds for the neutron flux incident on the activation foils both with and without Cd covers. The values employed for σ_0 and E_t^{23} are also given.

Foil	Reaction Daughter	σ_0 (mb)	E_t (MeV)	ϕ_0 (10^3 n/cm²-sec) wo/Cd	w/Cd
Ti	^{46}Sc	275	3.0	34.13	287.27
	^{47}Sc	21.4	2.2	29.91	107.48
Ni	^{58}Co	109	2.8	13.76	8.72

Thermal Neutron Measurements

Thermal and epithermal components of the neutron flux can be measured by a similar activation method. Samples in the form of foils are exposed to the unknown neutron flux, and the resulting activation

present in each foil is determined by standard counting techniques.
Sample materials are chosen to be sensitive to (n,γ) neutron capture
reactions in the thermal and resonance regions, rather than the (n,n')
and (n,p) reactions considered previously. The foils are irradiated in
pairs, one foil being fully exposed to the neutron flux, the other being
enclosed in a cadmium cover. Because cadmium possesses a large thermal
neutron capture cross section, a cover of about 0.076 cm thickness
serves to remove almost all thermal neutrons from the flux seen by the
shielded foil. Thus, the two foils will exhibit different activities,
making it possible to calculate the separate thermal and epithermal
neutron fluxes. This requires more than taking the simple difference of
the foil activities, however, since a number of correction factors
relating to neutron interactions in both the foils and the cadmium
covers must be included. The approach used in this work is outlined in
ASTM Standard E 262-86, "Standard Method for Determining Thermal Neutron
Reaction and Fluence Rates by Radioactivation Techniques",[38] which
includes numerous references to the literature. In this formalism, the
thermal neutron flux, ϕ_{th}, is related to the saturated activities of the
bare foil, A_s, and the cadmium covered foil, $A_{s,Cd}$, by

$$\phi_{th} = \frac{A_s}{g\sigma_o G_{th}} - \frac{A_{s,Cd} F_{Cd}}{g\sigma_o G_{th}} \left(1 + \frac{g\sigma_o}{G_{res} I_o} f_1 + \frac{\sigma_o w'}{G_{res} I_o} \right) \quad , \quad (13)$$

where the σ_o is the cross section for thermal neutron capture and I_o is
the resonance integral. The two saturation activities A_x for the bare
and cadmium covered foils are obtained directly from experiment as

$$A_x = \frac{N}{N_T T} \qquad . \qquad (14)$$

where N is the total number of excited nuclei produced, N_T is the number
of target nuclei, and T is the irradiation period. Finally, the
epithermal flux, ϕ_e, can be determined from

$$\phi_e = \frac{A_{s,Cd} F_{Cd}}{I_o} \qquad . \qquad (15)$$

The factors g, w', f_1, G_{res}, G_{th}, and F_{Cd} occurring in Eq. 13 represent corrections[38] required by neutron interactions in both foils and in

62

the cadmium covers used with the epithermal neutron detector. Determi-
nation of thermal and epithermal neutron fluxes in the general case
would require a detailed knowledge of the spectral distribution of the
neutrons, which is typically not available. The problem is simplified
if the detector material exhibits a cross section that varies inversely
with its velocity, since then the reaction rates are proportional to the
neutron density and are insensitive to the shape of the spectrum. In
practice, the problem is formulated assuming that the detector material
has a 1/v cross section behavior and the factor g appearing in Eq. 13 is
introduced to correct for deviations from this ideal behavior. The
correction factors f_1 and w' are required to account for epithermal
activation of the detector material that occurs between the lower bound
of the epithermal range (about 0.13 eV at room temperature) and the
cutoff energy of the cadmium filter (about 0.5 eV). Again, a 1/v cross
section is assumed for the purpose of calculating the principal correc-
tion f_1; deviations from 1/v behavior are corrected with factor w'. For
both thermal and resonance reactions, if the foil is thick compared to
the mean free path of a neutron, then corrections G_{th} and G_{res} for
self-absorption of the neutrons must be made. Finally, in the case of
indium the additional correction factor F_{Cd} is required.[39] The principal
resonance in indium occurs at an energy of 1.44 eV, and the low energy
wing of this resonance is affected by the presence of the cadmium cutoff
filter. As a consequence, the observed number of counts from the
epithermal detector must be increased by the factor F_{Cd} to account for
the resulting reduction in activation.

An experiment was performed to investigate the thermal and epither-
mal flux produced in the environment of the CLINAC 1800 operating in the
6 MeV mode. Because more than one experimental objective was being
pursued in this work, the linac was not operated in the vertical
orientation used for the photoactivation measurements, but was operated
horizontally. The principal difference resulting from this change in
configuration was that the beam was stopped by the cell wall at a
distance of about 4 m from the bremsstrahlung converter instead of the
floor at a corresponding distance of 2.29 m. Two 0.0254 cm thick indium
disks with diameters of 5.08 cm were simultaneously irradiated for 40
minutes at a distance of 100 cm from the photon source, with the axes of
the disks parallel to the beam axis. The 0.076 cm thick cadmium cover
used with the epithermal detector was formed of two 6.35 cm diameter
disks stamped to create a recess for the indium sample to occupy. This

recess was slightly larger than that of the indium foil to insure its complete enclosure. After irradiation, the 54.15 minute half-life activity of the neutron capture product, $^{116}In^m$, was counted with a NaI(Tl) spectrometer system. Standard corrections for detection efficiency, finite transit and counting times, gamma ray intensity, and photon self-absorption were made.

The saturation activities for each foil were calculated from the ratio $N/N_T T$ and were found to be $A_s = (27.58 \pm .16) \times 10^{-20}$ min^{-1}, and $A_{s,Cd} = (11.82 \pm .13) \times 10^{-20}$ min^{-1}. Under the assumptions that the cadmium cutoff energy was 0.5 eV and that the neutrons were thermalized to room temperature (293.4 °K), f_1 was found to be 0.445 using the methods of ASTM E 262 . Values of σ_o, I_o, g, w', G_{th}, and G_{res} may also be found in that reference. Indium of the thickness used in this work presents an areal density of 177 mg/cm^2 to the neutron flux. Because relatively large cross sections are involved ($\sigma_o = 161$ b, $I_o = 2593$ b), these foils cannot be considered to be thin in comparison to the mean free path of a neutron, and the values of G_{th} and G_{res} differ substantially from 1. The cross section σ_o given above is for the activation of the 127 keV, 51.15 minute isomer $^{116}In^{m1}$ either directly or through the intermediate 290 keV, 2.18 s isomer $^{116}In^{m2}$. For the thickness of cadmium used in this experiment, the value of F_{Cd} was estimated[39] to be 1.15. The thermal and epithermal fluxes were then calculated to be

$$\phi_{th} = 12 \text{ n/cm}^2\text{-sec} \quad ,$$

and

$$\phi_e = 6 \text{ n/cm}^2\text{-sec} \quad .$$

It is possible to use these fluxes to estimate the interference effects that thermal and epithermal neutron activation might have on the photonuclear cross sections listed in Table I. The maximum activities that could be produced by the thermal flux, $A_{n,th}$, and by the epithermal flux, $A_{n,R}$, can be calculated with the cross sections listed in Table III by using

$$A_{n,T} = \sigma_{T,I}\phi_{th} \quad , \tag{16}$$

and

$$A_{n,R} = \sigma_{R,I}\phi_e \quad . \tag{17}$$

64

The activities A_p corresponding to the photoactivation cross sections in Table I can be obtained in a similar fashion for any arbitrary sample position from

$$A_p = \sigma(2.125)\phi(2.125) \quad , \qquad (18)$$

where $\sigma(2.125)$ is the single state cross section for a hypothetical state at 2.125 MeV and $\phi(2.125)$ is the spectral intensity at that energy in the sample position. Most of the photoactivation data previously obtained in this effort has been acquired with a sample distance of 65 cm ($\phi(2.125) = 5.7 \times 10^6$ photons/cm^2-sec).

Because the linac was used in a different geometrical configuration for the thermal and epithermal activation measurements than for the photoactivation studies, an estimated correction factor must be employed to obtain values for the neutron flux at the sample position in the correct geometry. This estimate was obtained from the consideration that the thermal neutrons must originate either in the cell floor or the linac head. Of these two possible sources, the cell floor is much more probable because of its substantial hydrogen content. Since the low energy neutrons are formed by what is effectively a secondary emission process, the functional dependence of the neutron flux on the position of the secondary source is analogous to the classic radar signal problem. If the sample and the photon source were at the same position, then the thermal neutron flux would depend on the inverse fourth power of the distance to the cell floor. Because the sample and the photon source are separated in this case, the flux should instead vary as the product of the inverse squares of the source-wall distance and the wall-sample distance. Using this approximation, the ratio of expected low energy neutron fluxes for the vertical and horizontal configurations described above was found to be about 10. It should be noted that for the less likely case in which the low energy neutrons originate in the linac head, the variation of the flux with sample position will depend only on the inverse square of the separation between the neutron source and the sample. Thus for the geometry existing in the experiments described here, the chosen correction factor will also form a comfortable upper bound in this second, less likely, case.

For the purpose of estimating potential neutron activation interferences with Eqs. 16 and 17, the neutron fluxes obtained by the foil activation experiment were multiplied by the geometrical factor dis-

cussed above. The expected isomeric activities due to neutron capture were then calculated for all materials from Table III for which the neutron activation cross sections for the isomeric states were available. These values and the experimentally observed activations calculated from Eq. 18 are tubulated in Table VII, which also lists Ω, the fraction of the observed activation that could be ascribed to neutron capture processes.

For those cases for which the neutron activation cross sections for populating isomeric states are not available, the upper bound for neutron contamination can be estimated by assuming that 100% of the neutron captures that occur lead to the isomeric state. The values for these upper limits were obtained by using the appropriate total neutron capture cross sections from Table III and are listed within parentheses in Table VIII. Note that even these cases, the degree of contamination of the photoactivation results is less than 6 percent except in the instance of $^{183}W^m$. For this nuclide, use of the total neutron capture cross section to estimate the interference with the (γ,γ') reaction indicates that the upper limit for contamination is about 30%. This may, of course, greatly overestimate the true amount of neutron interference since it represents only the limiting value.

In conclusion, for all cases in which the neutron cross sections are available, the neutron activation resulting from the measured thermal and epithermal neutron fluxes is less than 1% of the observed activation and thus represents a minimal contamination of the photoactivation measurement. Where the appropriate cross sections are not available and the total neutron capture cross section must be used to estimate the degree of neutron capture interference, only the case of $^{183}W^m$ presents the possiblity of significant contamination. Further resolution of the interference issue for this isotope will require additional information on the neutron activation cross section for ^{182}W associated with the production of the isomer $^{183}W^m$.

66

Table VIII

Interfering activities due to neutron capture processes calculated from measured thermal and epithermal neutron fluxes. Capture cross sections have been taken from Table III. The observed activites A_p attributed to photoactivation, the calculated thermal neutron activation $A_{n,T}$, and the calculated resonance neutron activation $A_{n,R}$ have been tabulated. The parameters Ω_T and Ω_R are the contamination limits, in percent, of the observed activation by neutron capture processes.

Isomer	A_p (sec^{-1})	$A_{n,T}$ (sec^{-1})	Ω_T (%)	$A_{n,R}$ (sec^{-1})	Ω_R (%)
^{77}Se^m	4.37×10^{-19}	2.5×10^{-21}	0.6	1.0×10^{-21}	0.2
^{87}Sr^m	5.62×10^{-20}	1.0×10^{-22}	0.2	3.0×10^{-22}	0.5
^{111}Cd^m	1.85×10^{-19}	1.2×10^{-23}	0.006	1.2×10^{-22}	0.06
^{117}Sn^m	5.88×10^{-20}	1.2×10^{-24}	0.002	3.0×10^{-23}	0.05
^{123}Te^m	4.54×10^{-19}	(3.6×10^{-22})	(0.08)	(4.8×10^{-21})	(1.0)
^{135}Ba^m	3.65×10^{-19}	1.9×10^{-23}	0.005	(1.2×10^{-21})	(0.3)
^{137}Ba^m	1.19×10^{-19}	1.2×10^{-24}	0.001	(9.6×10^{-23})	(0.08)
^{167}Er^m	2.42×10^{-18}	1.8×10^{-21}	0.07	(6.0×10^{-21})	(0.2)
^{179}Hf^m	1.74×10^{-18}	6.0×10^{-21}	0.3	(1.1×10^{-19})	(6.0)
^{183}W^m	1.24×10^{-19}	(2.5×10^{-21})	(2.0)	(3.6×10^{-20})	(29)
^{195}Pt^m	1.17×10^{-18}	1.2×10^{-23}	0.001	(2.4×10^{-22})	(0.02)
^{199}Hg^m	1.04×10^{-19}	2.4×10^{-24}	0.002	(4.2×10^{-21})	(4.0)

Conclusions

On the basis of this work, the previously reported results for photoactivation cross sections are substantially free of any contamination by neutron capture or neutron scattering processes. The upper limit for contamination by neutron induced activation of the observed isomeric states is less than 6% in all cases for which the appropriate neutron cross sections are available and significantly less than 1% in many instances. These conclusions are based on a consideration of both fast and slow neutron sources and the corresponding (n,n') and (n,γ) interference reactions. The major source of fast neutrons in the experimental environment when the CLINAC 1800 is operated in the 6 MeV bremsstrahlung mode is the beryllium beam window in the linac head. The total neutron flux at the sample position due to this source is about 1000 n/cm^2-sec. Direct measurement of the thermal and epithermal fluxes indicates that at the sample position there are about 120 n/cm^2-sec in the thermal range and 60 n/cm^2-sec in the epithermal region. Using these values for the incident neutron flux and appropriate literature values for the neutron cross sections for isomeric activation leads to the conclusion that neutron activation effects are about two orders of magnitude less than the observed photoactivation effects.

References

1. C. B. Collins, C. D. Eberhard, J. W. Glesener, and J. A. Anderson, Rapid Communications, Phys. Rev. C, $\underline{37}$, 2267 (1988).

2. C. B. Collins, J. M. Carroll, and J. A. Anderson, Center for Quantum Electronics Report #GRL/8702, University of Texas at Dallas, 1987 (unpublished), pp. 13-44.

3. C. B. Collins, J. A. Anderson, C. D. Eberhard, J. F. McCoy, J. J. Carroll, E. C. Scarbrough, and P. P. Antich, Center for Quantum Electronics Report #GRL/8703, University of Texas at Dallas, 1988 (unpublished), pp. 37-56.

4. J. A. Anderson, C. D. Eberhard, J. F. McCoy, K. N. Taylor, J. J. Carroll, M. J. Byrd, C. B. Collins, E. C. Scarbrough, and P. P. Antich, Center for Quantum Electronics Report #GRL/8704, University of Texas at Dallas, 1988 (unpublished), pp. 11-35.

5. R. Mohan, C. Chui, and L. Lidofsky, Med. Phys. $\underline{12}$, 595 (1985).

6. N. C. Ikoro, D. A. Johnson, and P. P. Antich, Med. Phys. $\underline{14}$, 93 (1987).

7. J. K. Tuli, Nuclear Wallet Cards (National Nuclear Data Center, Brookhaven National Laboratory, 1985).

8. K. H. Beckurts and K. Wirtz, Neutron Physics, Trans. by L. Dresner (Springer-Verlag, New York, 1964), p. 266.

9. F. W. Walker, D. G. Miller, and F. Feiner, Eds., Chart of the Nuclides, Thirteenth Edition (General Electric Company, San Jose, Calif. 1983).

10. G. F. Knoll, Radiation Detection and Measurement (John Wiley & Sons, New York, 1979) p. 34.

11. B. Bulow and B. Forkman, "Photonuclear Cross Sections," in Handbook on Nuclear Activation cross sections, International Atomic Energy Agency Technical Report Series No. 156 (IAEA, Vienna, 1974) pp 475-558.

12. K. Fukuda, Nucl. Phys. A156, 10 (1970).

13. J. W. Jury, B. L. Berman, D. D. Faul, P. Meyer, and J. G. Woodworth, Phys. Rev. C 21, 503 (1980).

14. J. A. Harvey and D. J. Hughes, "Neutrons,", in American Institute of Physics Handbook, Ed. D. E. Gray, (McGraw-Hill, New York, 1963).

15. T. Lauritsen and F. Ajzenberg-Selove, Nucl. Phys. 78, 1 (1966).

16. M. F. Harris, "Meteorological Information," in American Institute of Physics Handbook, ed. D. E. Gray (McGraw-Hill, New York, 1972).

17. Southwestern Laboratories of Dallas, TX, kindly provided us with information relating to typical concrete mixtures.

18. G. S. Brady, Materials Handbook, 9th Edition (McGraw-Hill, New York, 1963).

19. Radiological Health Handbook, U.S. Department of Health, Education, and Welfare (U.S. Government Printing Office, Washington, D.C., 1970).

20. S. Glasstone and A. Sesonske, Nuclear Reactor Engineering, Third Edition (Van Nostrand, New York, 1981), p. 180.

21. G. D. Myers, private communication. Calculated using SNUPAR V2A Schlumberger Nuclear Parameters Code written by D. C. McKeon and H. D. Scott, 1988.

22. S. Glasstone and A. Sesonske, Nuclear Reactor Engineering, Third Edition, (Van Nostrand, New York, 1981), p. 13.

23. D. I. Garber and R. R. Kinsey, Eds., Neutron Cross Sections, Volume II, Curves, National Neutron Cross Section Center, Brookhaven National Laboratory publication BNL 325, 1976.

24. A. Calamand, "Cross Sections for Fission Neutron Spectrum Induced Reactions" in Handbook on Nuclear Activation cross sections, International Atomic Energy Agency Technical Report Series No. 156 (IAEA, Vienna, 1974) pp 273-324.

25. E. Ramstrm, Nucl. Phys. A315, 143 (1979).

26. H. A. Grench and H. O. Menlove, Phys. Rev. 165, 165 (1968).

70

27. H. C. Martin, B. C. Diven, and R. F. Taschek, Phys. Rev. 93, 199 (1954).

28. C. P. Swann and F. R. Metzger, Phys., Rev. 100, 1329 (1955).

29. G. L. Sherwood, A. B. Smith, and J. F. Whalen, Nucl. Sci. & Eng. 39, 67 (1970).

30. J. B Guernsey and A. Wattenberg, Phys. Rev. 101, 1516 (1956).

31. K. Sakurai and I. Kondo, Nucl. Inst. and Meth. 187, 649 (1981).

32. G. F. Knoll, Radiation Detection and Measurement (John Wiley & Sons, New York, 1979), p. 529.

33. Activation Foil Manual, distributed by Reactor Experiments Inc., 1965, and the references cited there.

34. ASTM Standard Method for Determining Neutron Flux, Fluence, and Spectra by Radioactivation Techniques, Publication E 261-77, (American Society for Testing and Materials, Philadelphia, 1987) and references cited there.

35. K. H. Beckurts and K. Wirtz, Neutron Physics, Trans. by L. Dresner (Springer-Verlag, New York, 1964), p. 286.

36. Foil Activation Data Unfolding Code (FATDUD), from the RSIC Computer Code Collection, Radiation Shielding Information Center, Oak Ridge National Laboratory.

37. E. Browne & R. B. Firestone, Table of Radioactive Isotopes, Ed. by V. S. Shirley (John Wiley & Sons, New York, 1986).

38. ASTM Standard Method for Determining Thermal Neutron Reaction and Fluence Rates by Radioactivation Techniques, Publication E 262-86, (American Society for Testing and Materials, Philadelphia, 1987) and references cited there.

39. C. W. Tittle, Nucleonics 8, 6 (1951).

A FLASH X-RAY SOURCE EXCITED BY STACKED BLUMLEIN GENERATORS
by F. Davanloo, J. J. Coogan, T. S. Bowen, R. K. Krause and C. B. Collins

Introduction

Recently we described[1-3] a flash x-ray source producing intense nanosecond pulses at high repetition rates. The principal innovation lay in the development of an x-ray diode of such low geometric profile that it could be matched to Blumlein pulsers having impedances as low as 1 Ω. Output pulses were found to have durations comparable to the transit times of the lines, and the combination of pulse duration and line impedance represented entry into a new region of parameter space.[4]

Despite the successes of these x-ray sources, one aspect differed little from devices we had developed earlier for short pulse nitrogen ion[5] and XeF lasers.[6] Each was driven by a Blumlein charged by a resonantly pulse charged power supply, and each line was tightly coupled to a diode load adapted to the application.[2] *Commutation was effected by a fast, low inductance thyratron; and ringing periods of the order of 100 ns could be realized in the switching cycle.* Operating parameters were most strongly constrained by the limitations on peak currents and the voltage tolerances of existing commercial thyratrons. At present the limits are 20 kA and 150 kV, respectively.

Reported here is a next step in scaling such impulsive devices to potentials greatly exceeding 100 kV, while retaining the capabilities for operation at high repetition rates. The example we describe is a pulsed x-ray generator, driven by stacked Blumleins that could be charged in parallel at the opposite end and commuted with a single thyratron. The output diode was matched to the series stack so that the end point energy of the bremsstrahlung approached the sum of the voltages launched on each individual line. No output switches were needed, and x-ray pulse durations were comparable to the transit time of the lines. The only breakdown device was the single thyratron providing the primary commutation. In these aspects, the device we report here offers some synthesis of individual advantages optimized in prior efforts.

Pulse-forming lines have long been used in the production of high power electron beams in accelerators and e-beam discharges.[7,8] Their

73

specific function is to provide impedance transformation between a power source and a diode load. To do this they must generally be isolated with fast-closing switches at one or both ends. These lines commonly consist of coaxial or triaxial Blumleins with dielectrics composed of water, oil, mylar, or a combination of these. In the archetype pulse power system, they are generally not required to provide voltage multiplication as well.

If very high voltages are required, Marx generators with several spark gaps are often used to charge the pulse-forming lines. Examples are found in accelerators and large e-beam machines. It has been reported that the number of spark gaps can be reduced somewhat by using a high-voltage transformer pulsed from a capacitor bank.[7] In either case, inputs to the lines typically consist of voltage pulses of the order of several MV from impedances high enough to require durations of 0.1 to 1.0 μs for charging.

In attempts to combine the functions of voltage multiplication and impedance transformation, Blumlein pulse-forming networks constructed from capacitors and inductors have been used; and in this case the lines themselves have successfully multiplied the charging voltages. Ivers et al.[9] designed a pulse generator that utilized seven artificial Blumlein pulse-forming networks, which were charged in parallel by a 30-50 kV power supply and discharged in a series configuration, avoiding conventional high-voltage Marx generators as a power source. However, the use of this type of artificial Blumlein led to triggering problems. Short commutation time between the load and trigger circuit prevented operation with a single switch. As a consequence Marx triggering columns had to be used, which inevitably limited repetition rates by reintroducing the Marx concepts.

In the work reported here, an array of eight triaxial Blumleins were successfully stacked to add voltage pulses for tens of nanoseconds in a configuration which could be switched with a single hydrogen thyratron without impedance transformation. Operation of a prototype device produced discharge voltages to 200 kV in an x-ray diode at peak currents of 0.5 kA for a 60 kV charging voltage. At 100 Hz an average x-ray dose of 5.8 R/s was obtained from x-ray pulses of 20 ns duration each. Developed here to excite nuclear fluorescence for the study of (γ,γ') reactions, the ultimate signal-to-noise ratio will depend only upon the total radiation that can be delivered to an extended absorber

74

in a working period. This laboratory-scaled alternative to either synchrotron radiation or to bremsstrahlung from large e-beam machines may be useful in a more general class of experiments that require access to an extended source of radiation with wavelengths below 0.1 A.

Device Design and Construction

Being described here is a prototype device consisting of three basic sections that comprised a pulse-forming system, which was then matched to a diode load. The essential sections of the pulse-forming system were: 1) the commutation assembly, 2) the transmission lines, and 3) the pulse stacking module. When integrated, the system with load extended over a nominal length of 4 m. This basic organization is shown schematically in Fig. 1. It was immersed in a closely fitting pan filled with transformer oil. The outer surface of the diode load was sealed with a gasket into the wall of the pan so the output could emerge without passage through the insulating oil.
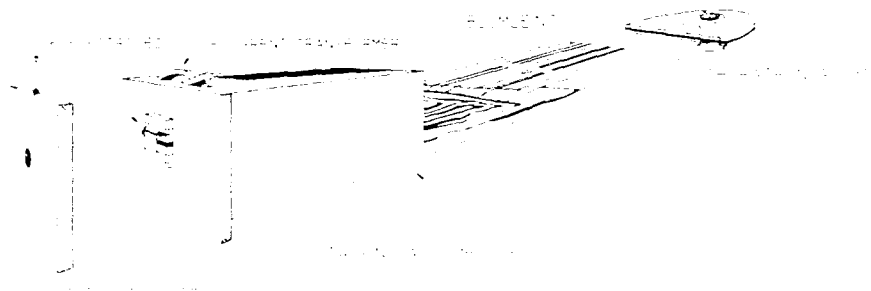
Figure 1. Schematic drawing of the flash x-ray device characterized in this work.

The commutation assembly is shown in Fig. 2. As usual, the thyratron provided the impulsive connection of two massive copper plates constructed from 3.2 mm stock with rounded edges. Their purpose was to distribute the switching current to each of the Blumleins in a manner designed to avoid both transit time inequalities and path constrictions which could bias the distribution. As shown in Fig. 2, the plates were

separated by layered Kapton dielectrics and were connected to the Blumleins with a closely lapped joint.
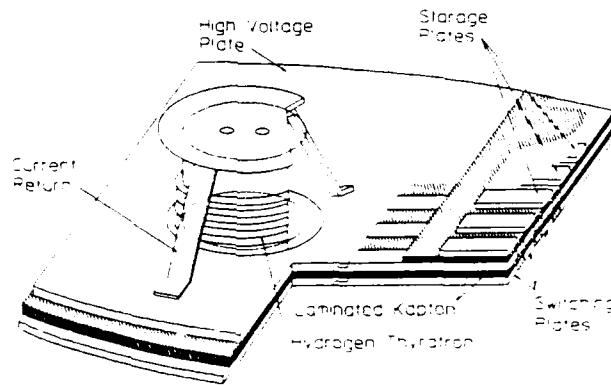

Figure 2: Layered configuration of the thyratron assembly is presented in a cut-away scheme. The lap joints of the lines to the thyratron plates are shown. The shaded portion of the figure consists of laminated Kapton film.

Both plates and dielectric were pierced to permit insertion of a thyratron. Edges of the lower plate were insulated by finger-like extensions of the Kapton dielectric layer. Connection from the lower plate to the anode well of the thyratron was accomplished with one of several low inductance cans, each designed for a different one of three possible thyratrons.

Details of the construction of the Blumleins are seen in Fig. 2. The eight individual Blumleins consisted of top and bottom (switching and storage) copper plates 3.8 cm in width. The center high voltage plates was similar, but only 2.5 cm wide to reduce field stresses at the edges and to increase dielectric lifetimes. All lines were made of copper 3.2 mm thick and 3.1 m long with rounded edges.

A laminated Kapton (polyimide) dielectric consisting of thirteen 0.127 mm thick layers separated the plates. These insulators were manufactured using an in-house lamination process. Alternate layers of Kapton and high dielectic epoxy were pulled through a press consisting of heavy steel rollers. The finished sheet had an average thickness of . 3 mm giving a line impedance of 26 Ω.

74.

The plates and the Kapton were lapped to 'plug-in" at both the thyratron and series ends, as seen in Fig. 3. These plates were completely sheathed in dielectric. In addition to the layer between the plates, 3.2 mm thick Lexan (polycarbonate) sheets enclosed the copper on the sides; and the Kapton walls were placed between each line to prevent interline flashover.
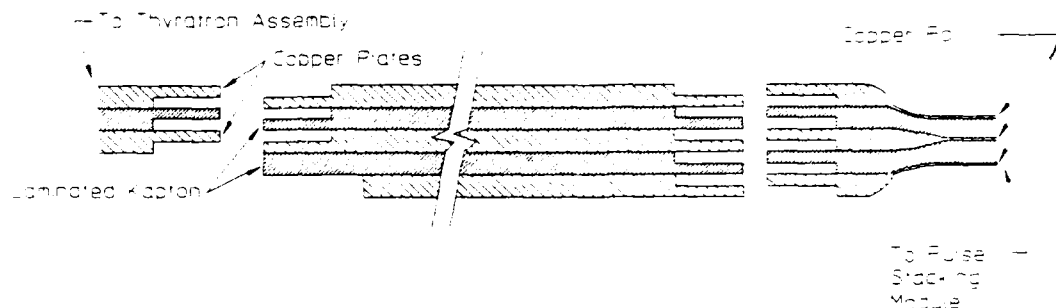

Figure 3: Side view of each transmission line connecting the commutation assembly and the pulse stacking module.

The Blumleins were switched from parallel to series with the rather complex structure shown in Fig. 4. The conductive lines were lapped to lengths of copper foil cut into curves in the plane of the foil so that the conductors from successive lines could be displaced toward the center where they would lie one above the other. Dielectric sheets were curved along the same lines to isolate the foils and to try to maintain a reasonably constant transmission line impedance of each Blumlein section being stacked. The resulting series section at the head of the lines was then cast to minimize corona. Figure 4 depicts this in a cut-away view.

Also incorporated into the pulse stacking module were a current transformer and an anode cooling system. Accommodations were made for a water-resistor voltage divider, as well. The top and bottom foils leading to the electrodes were conveyed through high temperature ceramic directly set into the cast material which formed the base wall of the diode load specific to the particular application.

It is well known that the line and continuous x-ray emission intensities are angularly distributed with respect to incident electron direction. The bremsstrahlung becomes more peaked in forward directions

as the incident electron energy increases.[10] Thus, in the high voltage
pulsing of x-ray diodes, the most energetic photons of the continuum of
x-rays are observed in the direction of the discharge electrons.
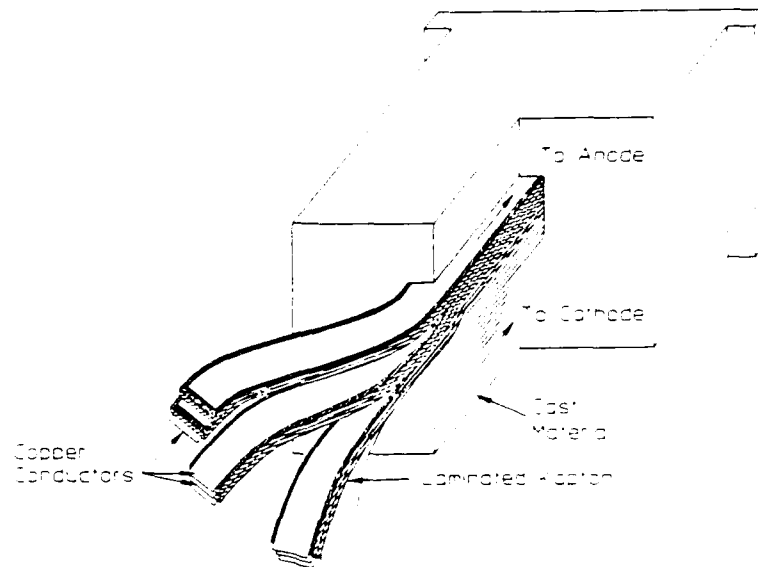

Figure 4:   Three full sets out of a total of eight Blumleins are shown
as   they are stacked in series when entering the casting material at
the base of the x-ray diode.   The top set shows the layering of the
conductor and dielectric components.   The laminated Kapton layers have
been shaded for clarity.

     In this work, the load matched to the voltage-multiplying lines was
an x-ray diode configured with two different electrode assemblies, as
shown in Fig. 5.   In the high voltage configuration, electrodes were
connected to the foils emerging from the base wall from the series part
of the lines.   A 2.5 cm wide graphite blade of 0.38 mm thickness was
connected to the cathode foil, while the anode foil emerged from the
ceramic inset in the wall to connect to an assembly for interchanging
anodes.   The useful part of the x-rays emerged from the output window in
the direction of the incident electron beams colliding with the anode
foil.   The spacing between the anode and cathode was adjusted by varying
the ceramic shim under the anode.   An alternative electrode assembly
similar to the one described in earlier works[1-3] is shown in Fig. 5. This
configuration was used in the low voltage operation of the device, and

useful x-rays were observed from an output window perpendicular to the direction of the discharge electrons.
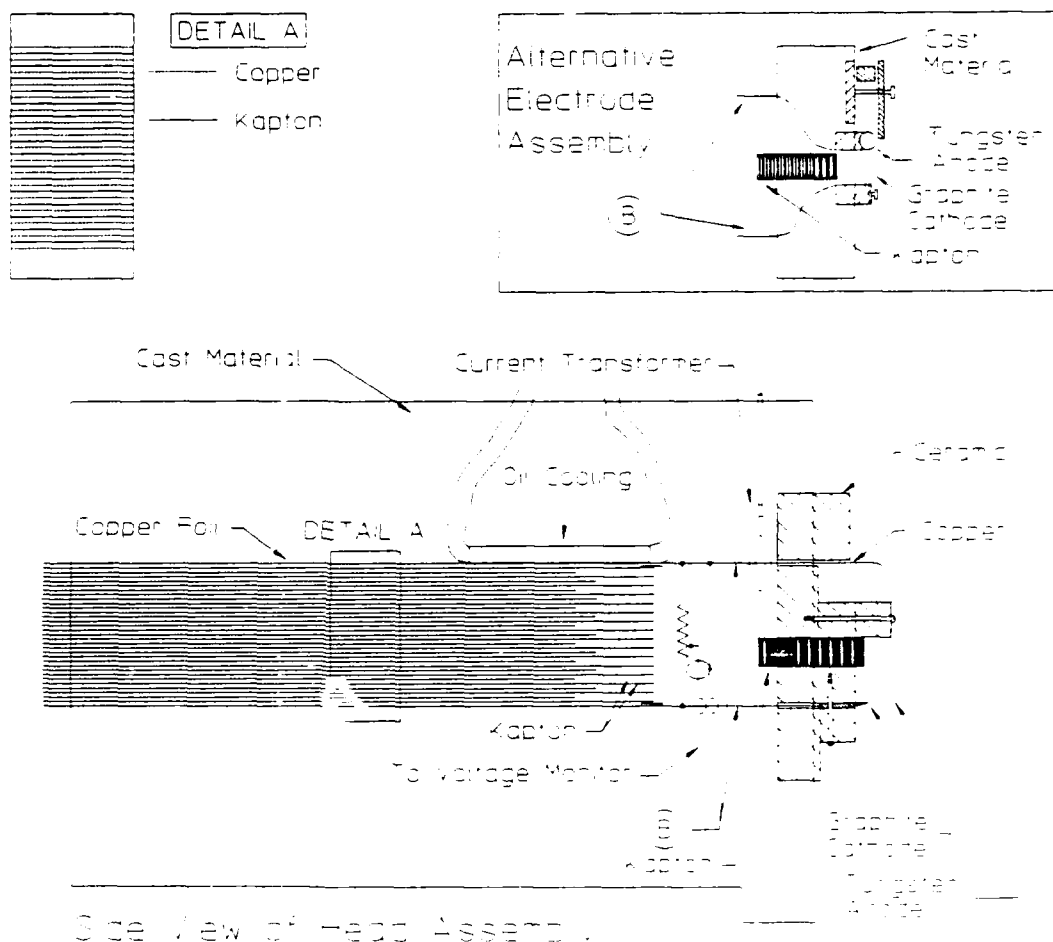

Figure 5: Schematic drawing of a cross section of the pulse stacking module used in this work. An alternative electrode assembly for low voltage pulsing is shown.

A vacuum cover was sealed to the particular head being used by an O-ring. The pressure cover was machined out of Delrin plastic and the completed diode could be routinely evacuated to pressures below 5 microns. An output window made of layered Kapton and graphite was placed directly in front of discharge area as seen in Fig. 1. In operation, all components except for the pressure cover with an output window were immersed in transformer oil.

79

Operation and Performance

In operation, the Blumleins were resonantly pulse charged with a source capable of bringing the 16 nF total capacitance of the system to a selected voltage in the range 3-75 kV in 100 μs.[11] The middle conductors were charged to a positive high voltage. For the performances described here, commutation was effected by a three-stage EG&G 5353 hydrogen thyratron mounted in a grounded cathode configuration.

Both the voltages launched on individual lines and the voltage pulse appearing across the series stack at the head were measured with tapped water resistors as shown in Fig. 5. They were connected to a Tektronix 7912AD transient digitizer. A comparison of pulses launched and received at the stack for both open and loaded circuits is shown in Fig. 6. As can be seen, the output voltage into a matched load approached four times the charging voltage of each line.
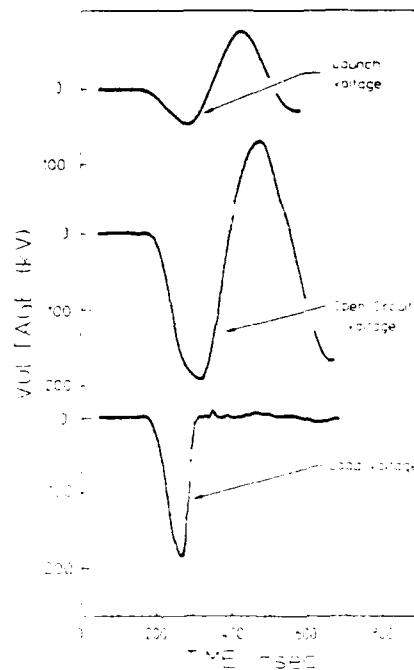

Figure 6: *Voltages measured across the individual lines and across the series stack with and without load as a function of time. The top pulse is typical of the voltage launched down each line by commuting the thyratron. These particular data correspond to a charging voltage of 50 kV.*
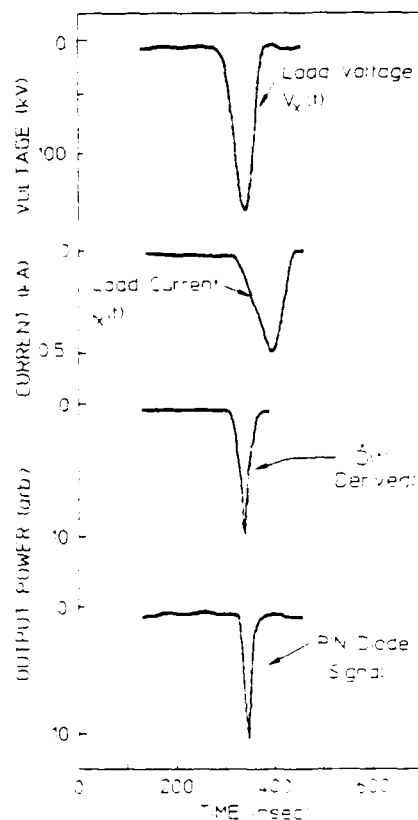
Figure 7: *Typical relationship between the load voltage, load current.*
and x-ray output emmitted from the tungsten anode. These particular data
correspond to a charging voltage of 60 kV. The derived x-ray output in
this figure was obtained from the data as described in the text.

The temporal evolution of the x-ray output from the diode is shown
in Fig. 7, together with the time dependence of the voltage and current
at the diode. For this measurement, the x-rays were detected with a PIN
diode directly coupled to the Tektronix 7912AD. Electrical performance
was recorded with the integral diagnostics described above. Synchroniza-
tion was readily maintained between records of voltages and PIN diode
signals, but the current monitor required a different grounding arrange-
ment which disturbed the triggering. The relative phase of the current
ulse on the time scale of Fig. 6 had to be determined from the relation-
ship[2] between instantaneous power and the corresponding time derivative
of the x-ray dose, D,

$$D(t) = K_c I(t) V^2(t) + K_L I(t) [V(t) - V_K]^{1.7}$$ (1)

81

where I(t) and V(t) denote the instantaneous values of current and voltage, respectively, at the x-ray diode and V_K is the potential of the K edge for the material of the anode. The first term of Eq. (1) describes the energy emitted as bremsstrahlung continuum, while the second describes emission of the characteristic lines of the anode. The constants K_c and K_L denote the relative efficiencies for the emission of continuum and line radiation, respectively.

For the purposes of synchronizing I(t) with V(t) it was assumed

$$K_c = 2.1 \ K_L \qquad , \qquad\qquad\qquad\qquad (2)$$

in general agreement with previous results. Then Eq. (1) was evaluated for values of load voltage V(t) input from Fig. 7 and for I(t+r) where I(t) was taken from the raw data and r was an adjustable phase shift. Shown in Fig. 7 is the D(t) computed for the particular value of r giving the current waveform plotted there for comparison. That D(t) represented the best agreement which could be obtained by this procedure. It seems to be reasonably phased with the voltage waveform since appreciable amounts of current are seen to start at the time V(t) begins to break from the form of the open circuit ringing.

The x-ray spectra emitted by this device were sampled with an imaging system formed with a pinhole. The output window was heavily masked with lead collimators, and the detector was similarly masked to admit only the image of the open aperture at the source. In this way the contribution from spurious Compton scattering was minimized. A test for the magnitude of the remaining Compton intensity not originating in the source itself was conducted by blocking only the open aperture at the source. No counts were detected on the scale used for the presentation of the spectra.

The detector used to observe the image of the source aperture was a NaI(Tl) crystal mounted to a photomultiplier whose output was connected to an ORTEC preamplifier/amplifier combination servicing a multi-channel analyzer. By adjusting the size of the imaging pinhole, the intensity at the scintillator could be reduced to the point at which one photoelectron was counted by the electronics on the average of every three discharges. In this way pulse pileup was avoided. The data obtained in this way comprised a pulse height spectrum which reasonably approximated the desired spectrum of intensity as a function of photon energy. Radioactive sources emitting lines at convenient energies were used to

82

calibrate the relationship between photon energy and detected pulse height. Since the deviation from simple proportionality was less than 4% over the range of energies of interest, a linear relationship was used in the final analysis of the spectral data.

The spectrum of the counting rate detected at each photon energy was multiplied by the ratio of $2\pi/\Omega$, where Ω was the measured solid angle of the pinhole. The resulting spectrum is shown in Fig. 8. Data at lower energies than those shown were rendered uncertain by levels of Compton scattering in the detector and so were not plotted in Fig. 8. Errors in the intensities accrued primarily from statistical uncertainties in the numbers of photons, n collected in each of the discrete windows in photon energies. A reasonable expectation is that the statistical error in intensity is $\sqrt{n}$. This can be estimated in Fig. 8 from the identification of the lowest intensity shown there with the accumulation of a single photon in the corresponding window in energy. Experimentally, this uncertainly is seen in the scatter of the data in Fig. 8.

With this first prototype device, x-ray pulse energies were found to remain largely constant as the pulse repetition rate was varied over the range from 1 to 100 Hz. Figure 9 shows this to be reflected in the measured values of average dose output in the x-ray pulses of 20 ns duration emitted from a tungsten anode.

Average x-ray powers at 100 Hz resulting from the operation of this device with a charging voltage of 50 kV showed that in less than 4 minutes, a dose of one kR could be delivered to a target sample. This would exceed the dose available in the bremsstrahlung from a shot of a large laser plasma or small e-beam machine.
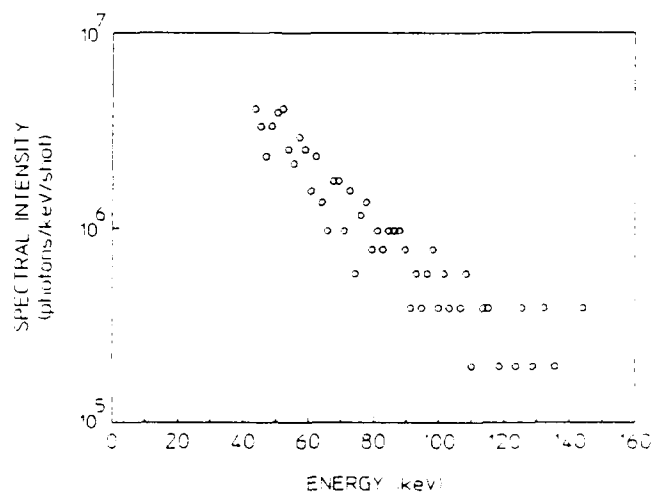
83

Figure 8: Typical spectral distribution of flux emitted from the tungsten anode at a charging voltage of 50 kV.
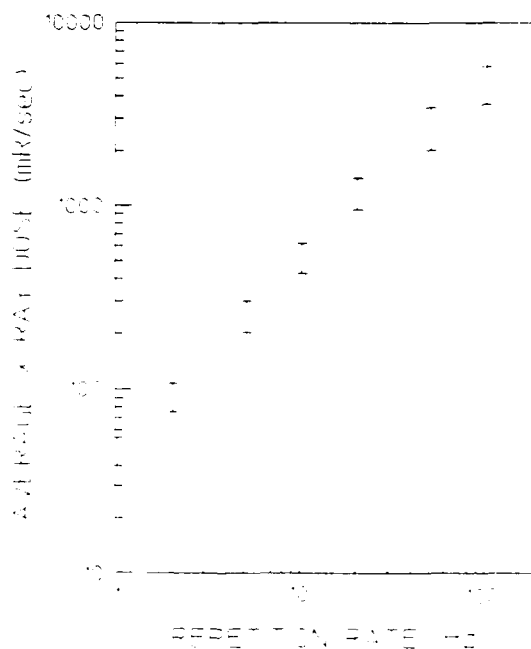

Figure 9: Average dose outputs emitted as x-rays near 1 A as a function of the pulse repetition rates for a charge voltage of 50 kV.

24

References

1. C. B. Collins, F. Davanloo, and T. S. Bowen, Rev. Sci. Instrum. 57, 863 (1986).

2. F. Davanloo, T. S. Bowen, and C. B. Collins, Rev. Sci. Instrum. 58, 2103 (1987).

3. F. Davanloo, T. S. Bowen, and C. B. Collins, in Advances in Laser Science-I, edited by W. C. Stwalley and M. Lapp (AIP Conference Proceedings No. 146, New York, 1986) pp. 60-61.

4. P. Krehl, SPIE Review 689, 26 (1986).

5. C. B. Collins, IEEE J. Quantum Electron. QE-20, 47 (1984).

6. R. Sadighi-Bonabi, F. W. Lee, and C. B. Collins, J. Appl. Phys. 53, 8508 (1982).

7. J. R. Smith, R. F. Schneider, M. J. Rhee, H. S. Uhm, and W. Namkung, J. Appl. Phys. 60, 4119 (1986).

8. M. T. Buttrom and G. J. Rohwein, IEEE Trans. Electron. Devices ED 26, 1503 (1979).

9. J. D. Ivers and J. A. Nation, Rev. Sci. Instrum. 54, 1509 (1983).

10. E. C. Booth and J. Brownson, Nuclear Physics A98, 529 (1967)

11. F. Davanloo, T. S. Bowen, J. J. Coogan, and C. B. Collins, in Center for Quantum Electronics Report No. GRL/8602, University of Texas at Dallas, 1987, pp. 47-70.

PRELIMINARY STUDY OF A LASER ION SOURCE FOR GROWING DIAMOND-LIKE CARBON FILMS

by C. B. Collins, F. Davanloo, E. M. Juengerman, W. R. Osborn, and D. R. Jander

General interest in diamond-like carbon (DLC) films is motivated by their unique combinations of physical hardness, electrical strength, high thermal conductivity and optical transparency. In the U.S., studies have been recently accelerated by prospects of commercial application for optics and semiconductors, but no single technique has yet produced films with uniform properties at practical rates of growth. Our own interests arise from the need for a crystalline host for nuclei being evaluated for use as gamma-ray laser media.

Four methods remain at the focus of current interests: ion-beam deposition,[1-4] chemical vapor deposition (CVD),[5-7] plasma enhanced CVD (PECVD),[8-11] and sputtered deposition.[12-15] Contamination is minimized in the first because only the ions of carbon are accelerated to selected energies and deposited on a substrate in a high vacuum environment. In such systems differential pumping and mass separation further reduce the level of the inclusion of impurities into the films. Layers of high quality can be obtained, but at the cost of very slow rates of growth.

In CVD and PECVD both ions and neutral atoms of carbon are produced by the dissociation of organic vapors, such as CH_4, C_2H_2, and CH_3OHCH_3, and deposited on substrates. The unwanted collateral products of dissociation provide ready sources of contamination. While growth rates reach practical levels, no one has yet reported the preparation in this way of DLC films of optical quality. The sputtering technique requires two ion-sources, one for sputtering carbon from a graphite source with enough velocity to reach the substrate and another for breaking the unwanted graphite bonds which may otherwise remain in the growing film. The two ion sources make the system cumbersome and the higher pressures (10^{-5} to 10^{-4} Torr) needed to support the sputtering process introduce problems of contamination that degrade the films to a level comparable to those encountered in CVD and PECVD. Lasers have been used[16] in a variant of the CVD process, but with similar results and problems.

While natural diamond is a well defined substance, the diamond-like films grown by these various methods are not. This has contributed much complexity to the evaluation of the merits of the different techniques

of preparation. In many cases different materials result from the different methods of deposition.

From a structural viewpoint, Spencer[2] has identified six allotropes of carbon, two for each of the numbers of dimensions through which the carbon atoms may bond. Linear sp bonds are expected to form carbynes and cumulene, hile planar sp^2 bonds give rise to hexagonal graphite and chaoite. Of most interest are the three dimensional sp^3 bondings which give not only diamond, but also the less familiar Lonsdaleite, a hexagonal form of diamond. However, it seems that no procedure for the deposition of thin film carbon gives just one of these products to the exclusion of all others.

Most thin film diamond is currently grown by one of the CVD variants from a hydrocarbon feed material. First to be deposited is an amorphic layer termed diamond-like carbon (DLC). This is known to contain 20 to 60% hydrogen and it conforms to none of the forms expected above. Depending upon the availability of nucleation sites, individual crystallites of diamond will begin to grow in the DLC base after a period of latency which can reach 10 hours at 900°C in the absence of artificial seeding of the material.

Once started, the crystallites can grow to densely fill the coated area forming a polycrystalline layer displaying most of the properties expected of a packed bed of small natural diamonds. Raman and energy loss spectra are generally identical to those obtained from natural diamond and identification is easy. Unfortunately, such layers are not single, smooth films but rather are conglomerates of individual particles.

Only the ion beam techniques produce a substantially different result giving a smooth transparent material with many of the properties of diamond, but lacking the characteristic Raman line. This material is termed dehydrogenated DLC and its composition is actually unknown. Speculations are that it may contain short-range mixtures of diamond or Lonsdaleite sp^3 bondings. However, with the ion beam methods growth rates are extremely slow and the material they produce has necessarily remained only a curiosity.

Here we continue[17] to report upon a hybrid method in which the modest rate of growth that characterizes the cleaner ion beam method is enhanced by the high fluence of carbon ions that can be separated from a

discharge plume excited by a laser beam focused upon a cold graphite source. The free expansion of the carbon plume into a UHV chamber operated at 10^{-6} Torr seems to rapidly attenuate the flux of neutrals impinging upon a substrate positioned at some distance, while the ions are guided more directly to the surface of the growing film. Since the laser is pulsed for 10 ns periods the peak growth rates are very high. The duty cycle is low but average growth rates can still reach 20 $\mu m/h$. Films show the characteristics of the dehydrogenated DLC materials, having a mirror smooth surface finish and a uniformity of an optical quality. Most surprising is that the growth of these films does not require any seeding of the substrate with debris from abrasive treatment with either diamond or any other particles. Areas of 10 cm^2 have been coated with uniform optical quality on a variety of substrates with only routine cleaning.

Our technique is shown schematically in Fig. 1. As seen there, the output from a Nd-glass laser was focused on a graphite target placed in a UHV environment. The gross effect of the laser beam was to eject a *plume of carbon* vapor and then to ionize a portion of it. The neutral
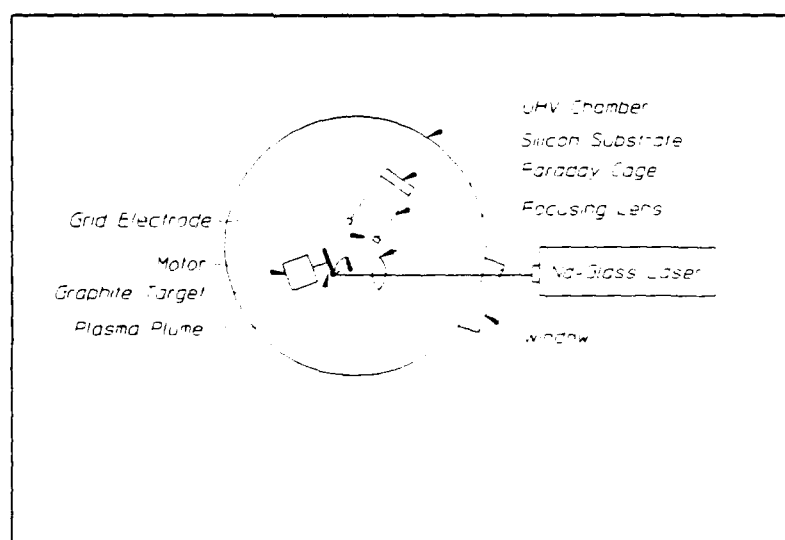

Figure 1: Schematic representation of the experimental apparatus.

cloud expanded isotropically, as evidenced by the pervasive coating of soot which developed in the UHV chamber while the ions were ejected into a cone of 45° centered about the outward normal to the graphite target.

Within the last two years in both the GDR[18] and Japan,[19] laser ablation has been evaluated as a potential source of feed material for diamond epitaxy. However, in neither investigation did the peak laser power exceed 10^9 W/cm^2 at the target and auxiliary discharges were not used. In contrast our technique has been operated with an intensity in the focus of greater than 10^{10} W/cm^2. Either the earlier efforts had missed the directed stream of ions or they had failed to produce them, because negative results were reported.[18,19]

Recently we described[17] a first success in using auxiliary electrodes to contribute to the extraction of the collimated stream of carbon ions and neutrals observed to be jetted from an illuminated block of graphite toward a substrate for deposition. Using a one Joule, Q-switched YAG laser we ablated the surface of a graphite target at the focal spot of a 10 cm lens in a UHV chamber. Process voltages of 1600 V were sufficient to insure that the proper types of diamond precursors were directed onto a 10 cm^2 substrate. Edges of the stream were well defined but within it fluences were remarkably uniform, depositing one monolayer per laser shot. Accumulations from successive shots were uniform to ±2% over such areas.

The deposited material generally appears smooth and transparent having an index of refraction of 2.0 to 3.0. Unrecognized variation of process variables sometimes produces a brownish coloration to the film. On Si(111), Ge, quartz, and glass electrical resistivity is high and the material seems to fall into the same poorly understood class of "dehydrogenated DLC" materials as are traditionally produced by the ion beam methods. No seeding or heating of the substrate is needed and substrate temperatures seem to remain at ambient room values during processing.

The role of the electrodes is curious. Originally thought to accelerate the ions of the ablated material,[17] subsequent study has rendered this role unlikely. Current operation depends upon a 250 mJ, Q-switched YAG capable of operation at 10Hz. Even under these lessened inputs, there is far too much material (~10^{15} particles) transferred from ablation plume to substrate to be moved as unshielded ions. The energetics require the transported material to be largely neutral,

90

either atoms or plasmas, and in this case electrostatic acceleration
would be very inefficient.

The current which was passed from electrode to the ablation plume
was measured with a Ragowski coil, electrically isolated from the
deposition system. A typical result is shown in Fig. 2 where it can be
seen that currents peak in the 1-10 A range in a pulse found to have
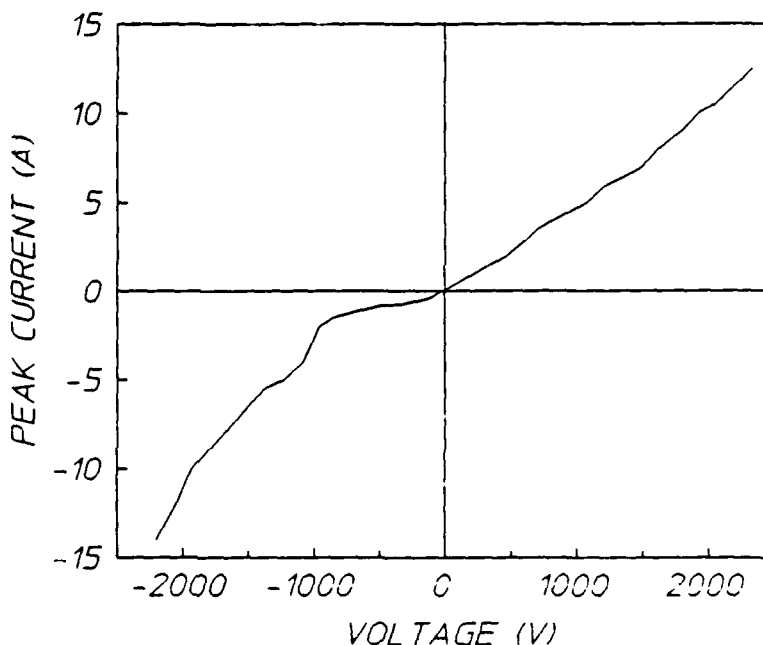FWHM of the order of 2 μsec. From the time-dependence of the current it

Figure 2: Plot of the current and voltage characteris-
tics of the diode formed by the graphite target and the
grid containing the conductive plasma ablated from the
graphite by the laser.

appears that current flows only when the ablated material is filling the
space between the point of ablation and the electrode, as would be
expected.

The V-I characteristics seen in Fig. 2 are typical for a gas-filled
diode with the "forward" direction for conduction being established when
the plume is negative and so able to function as a hot filament.
Voltages and currents in Fig. 2 are referred to the collecting electrode
so characteristics of "forward" conduction are found in the positive
(first) quadrant. In the "reverse" direction current is lessened until
the potential difference is sufficiently elevated to cause a glow

discharge. It is not yet clear whether such discharges contribute any important processing of the jetted material. The selection of either positive or negative voltages to give the same absolute values of current generally yield very similar depositions on Si(111) substrates.

It is our working hypothesis that it is the current itself which provides the essential contribution to the quality of the films being deposited and that the effect occurs entirely in the relatively small volume of the high temperature plume. This perception was strengthened by two additional tests not yet reported elsewhere.

First, the possibility was examined that the diamond precursors were processed or directed by the current in the drift space between plume and electrode. Arrangements of parallel plates and screens were placed so that the discharge current was largely confined to the space between them. The ablated material passed freely through the discharge space but failed to produce the smooth films with an optical quality. Little difference could be observed when the current was discontinued. Any small effects which were perceived under these conditions seemed to correlate only with the occurrence of accidental leakage currents from the discharge space to the ablation plume.

Building upon this indication that currents in the drift space were unimportant a second test was made to determine the significance of the electrode geometry and placement. There seemed to be none. Replacing the mesh electrode shown in Fig. 1 with a blunted rod made no detectable change in the characteristics of the deposited film. More surprising was the observation that the change of position of the tip of the anode rod from the center to the edge of the cone bounding the paths of the major flow of material from the point of ablation to the substrate had no discernible effect. Together with the first test, such a result suggests that the phenomenology is dominated by the parameters of the ablation, itself.

The predominance of DLC in the films was indicated by Raman spectra such as shown in Fig. 3. The particular signature of the DLC[14] is the broad triangular structure peaking at 1560 cm^{-1} with a base stretching from 1000 to 1600 cm^{-1}. The thickness of this film was only about 200 A and the DLC spectrum is well-developed for such a thin film, probably because of the optical quality. The same spectrum was obtained at different locations sampled on the film. The prominent lines in Fig. 3

92

were background contribututions from Si and air, as marked.   The Si
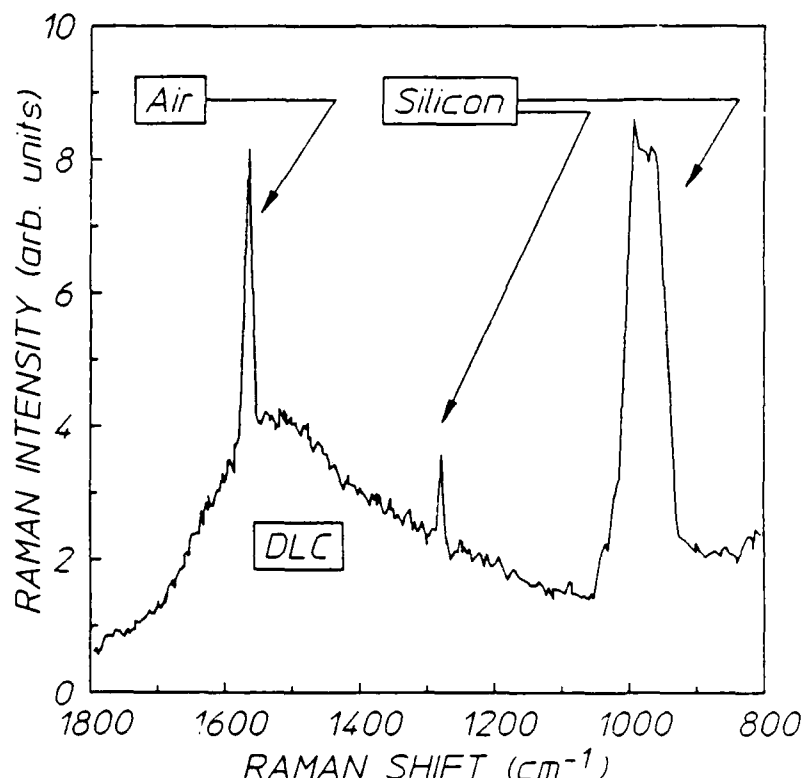lines were found to be much stronger than were produced by an uncoated

*Figure 3:   Spectrum of the Raman scattering of the
514.5 nm output of an argon ion laser from a 180 A
thick film of DLC grown on a Si(111) substrate from
carbon ions from the laser ion source.*

substrate.   This enhancement has been reported previously[15] and is
attributed to the partial matching of the indices of refraction by the
DLC coating.

Ellipsometry measurements showed the index of refraction to be
uniform across a single film, but to be dependent upon the applied
voltage that had been used to deposit the DLC. Several films were grown
with different voltages, each chosen to produce a DLC with a different
index of refraction lying within the range 1.5 - 2.15.   The ellipsometry
measurements also confirmed that the thickness of the films corresponded
to a nominal deposition rate of 1 A/pulse of the laser for a substrate

93

placed 15 cm from the plasma plume. The particular sample characterized in Fig. 3 was found to have a thickness of 180 A with a surface roughness of only ± 1A.

Tests of chemical and physical parameters showed the films to be completely intact after immersion in boiling water for one hour and 10% HCl solution for one-half hour. The resistance measured on the surface between two test points one centimeter apart was found to vary from a value for freshly prepared films larger than could be measured with available methods, > 40 MΩ to less than 500 Ω in films annealed at 600°C. This agrees with previous observations[4] of the graphitization of DLC films.

The Q-switching of the YAG laser seems to be essential. In agreement with earlier work, we observed that poor quality films were deposited at lower values of peak power density in the ablation plume. Our tentative conclusions are that the high proportions of ions to neutrals at the highest plasma temperatures in the plasma jets formed by laser ablation are responsible for the uniform optical quality of the dehydrogenated DLC films grown by the technique we are reporting. In this way the advantages of the ion beam method for the deposition of dehydrogenated DLC are enhanced by the greater fluences available from laser plasma sources. At deposition rates currently realized of 1 A/pulse over tens of cm^2 a growth rate of DLC approaching 20 μm/h could be realized with commercially available lasers.

The authors wish to convey their sincere appreciation to colleagues who generously shared their diagnostic capabilities; in particular M. Green and T. D. Black of the Physics Department of the University of Texas at Arlington for the Raman spectroscopy and S. Lambert of Varo, Inc. for the ellipsometry.

94

References

1. S. Aisenberg and R. Chabot, J. Appl. Phys. 42, 2953 (1971).

2. E. G. Spencer, P. H. Schmidt, D. C. Joy, and F. J. Sansalone, Appl. Phys. Lett. 29, 118 (July 1976).

3. T. Mori and Y. Namba, J. Vac. Sci. Tech. Al, 23 (1983).

4. S. Kashi, H. Kang, and J. Wayne Rabalias, Phys. Rev. Lett. 59, 75 (July 1987).

5. B. V. Spitsyn, L. L. Bouilov, and B. V. Derjaguin, J. Cryst. Growth 52, 219 (1981).

6. S. Matsumato, Y. Sato, M. Kamo, and M. Sakata, Jpn. J. Appl. Phys. 21, (1982) L183.

7. A. Sawabe and T. Inuzaka, Appl. Phys. Lett. 46, 2 (1985).

8. L. Holland and S. M. Ojha, Thin Solid Films 58, 107 (1979).

9. J. Vora and T. J. Moravec, J. Appl. Phys. 52, 6151 (1981).

10. S. Matsumoto, M. Hino, and T. Kobayashi, Appl. Phys. Lett. 51, 737 (1987).

11. K. Kurihara, K. Sasaki, M. Motonobu, and N. Koshino, Appl. Phys. Lett. 52, 437 (1988).

12. C. Weissmantel, K. Bewilogua, D. Dietrich, H. J. Erler, H. J. Hinnerberg, S. Klose, W. Nowich, and G. Reisse, Thin Solid Films 72, 19 (1980).

13. T. Miyasato, Y. Kawakami, T. Kawano, and A. Miraki, Jpn. J. Appl. Phys. 23, (1984) L234.

14. M. Kitabatake and K. Wasa, J. Appl. Phys. 58, 1693 (1985).

15. M. Mirtich, Dan Nir, D. Swec, and B. Bank, unpublished.

16. K. Kitahama, K. Hirata, H. Nakamatsu, and S. Kawi, Appl. Phys. Lett. 49, 643 (1986).

17. S. S. Wagal, E. M. Juengerman and C. B. Collins. Appl. Phys. Lett.
     53, 187 (1988).

18. A. Richter, H. J. Scheibe, W. Pompe, K. W. Brzezinka, and I.
     Muhling, J. Non-Cryst. Solids 88, 131 (1986).

19. T. Sato, S. Furuno, S. Iguchi, and M. Hanabusa, Jpn. J. Appl. Phys.
     26, L1487 (1987).

LARGE SCALE EFFECTS OF THE MAGNETIC PHASE MODULATION
OF RECOILLESS GAMMA TRANSITIONS

by T. W. Sinor, P. W. Reittinger, and C. B. Collins

A recent Letter[1] reported variations in recoilless gamma-ray spectra produced by directly modulating the interaction energies arising from the couplings of the nuclear magnetic moments to the hyperfine fields. Described in terms of the phase modulation of the nuclear states involved in the transition, those results represent important realizations of some of the general possibilities for developing nuclear analogs[2,3] of coherent transient effects studied in quantum optics.

An example is found in the frequency domain in the excitation of sidebands on gamma-ray transitions, and precursive work[4,6] had treated that problem in a manner equivalent to an application of the phase modulation formalism.[3] For cases in which there is no static magnetic field[5] or in which the modulation is parallel to the static field,[6] the effect of the time varying component $H_0f(t)$ upon an eigenstate of the nucleus, $\Psi^{(o)}_{a,m}$, can be written,

$$\Psi_{\alpha,m} = e^{-i\phi_\alpha(t)} \, \psi^{(o)}_{\alpha,m} \qquad , \qquad (1)$$

where $\phi_\alpha(t)$ is the modulation angle of the phase,

$$\phi_\alpha(t) = m\omega_x \int_0^t f(t')dt' \qquad , \qquad (2)$$

and the Larmor frequency ω_α is,

$$\omega_\alpha = \mu_N g_\alpha H_0/\hbar \qquad , \qquad (3)$$

where μ_N is the nuclear magneton, g_α is the gyromagnetic ratio for the α-th excited or ground state of the nucleus, and m is the magnetic quantum number of the eigenstates.

In principle, the difference in phase modulation between the ground state, g, and an excited state, e, may be observed during an absorption transition because the Fourier components of $u_e(t)-u_g(t)$ will be manifested as sidebands. However, since the transition will have a width Γ associated with the time-dependent decay of the states, unless,

$$\hbar\omega_\alpha \geq \Gamma \quad , \tag{4}$$

the sidebands will be buried in the natural wings of the probing transition. Only the ingeneous use of the ultra-narrow, 93-keV line ^{67}Zn permitted the quantitative study of the coherent phase modulation effects recently described.[1] That benchmark achievement required field amplitudes reaching 13.4 mT for sinusoidal modulation at applied frequencies ω up to 10 kHz and effects were reported[1] to scale as (H_0/ω).[2] At the upper limit of frequency the condition of Eq. (4) would have been satisfied and the particular coherent effects reported would have been visible as sidebands in the frequency domain. However, the difficulties of this experiment seem to imply that such studies will not be extended to nuclear systems with greater transition widths through simple extensions of effort.

The conceptual key to orders-of-magnitude of enhancement of phase modulation effects has been reported[7-9] to lie in the use of smaller powers to manipulate the greater magnetic fields arising from the natural correlations of individual spins in ferromagnetic materials. However, the modulation $\partial M/\partial t$ of the magnetization M of a ferromagnetic material is rarely parallel to either the applied field H_0 or even to M, itself.[10] For such cases of nuclei in ferromagnetic media, the modulation angle of Eq. (2) takes a more complex form[7]; and one which causes a mixing of the eigenstates, $\Psi^{(0)}_{\alpha,m}$. Nevertheless, the principal parameter is still a Larmor frequency Ω_α which for magnetic environments becomes,

$$\Omega_\alpha = \mu_N g_\alpha M/\hbar \quad , \tag{5}$$

a value much larger than that found in Eq. (3) for nonmagnetic samples. Unfortunately, magnetic materials are almost invariably magnetostrictive and the concern has lingered that even the enhanced effects of phase modulation might always be overwhelmed by the periodic Doppler shifts produced by vibration in the lattices excited by magnetostriction.

The propagation of magnetoelastic waves is a complex problem which has been intensively studied since 1958.[11] For many magnetic media the dispersion equation for such waves displays several branches[12,13] which can be individually identified with spin waves, magnetostatic waves or elastic waves. Mixed waves coupling magnons and phonons occur principally when branches intersect, so that the frequencies and wavelengths for both are nearly equal.[11] Away from those values of parameters magnetic and acoustic waves can be separated. In principle this offers

98

a means to propagate only the former to a sample in which it is desired to magnetically modulate the phases of the states of the nuclei to be observed there without the concomitant introduction of acoustic noise.

The most convenient of the Mössbauer transitions for modulation experiments is the 14.4-keV transition of ^{57}Fe diluted in a thin metal foil. The propagation of magnetic waves in conductive foils presents a special problem because of eddy current losses; Kittel has given an approximation[11] which would limit the mean free path for a magnon to a few wavelengths for the frequencies of tens of MHz which would be interesting for use with ^{57}Fe. For this reason the preferred choices for the propagation of magnetization in such thin metallic foils are the magnetostatic waves characterized by long wavelengths and high group velocities[12,14] that are quite removed from intersections with acoustic branches. Wavelengths can readily reach the scale of millimeters, and it has been demonstrated that dispersion properties are little affected by raising the temperature of the foil above the Curie point[15] so that the material becomes paramagnetic.

The stainless steel used in these experiments was a nonmagnetic alloy, 310 which was expected[16] to have a susceptibility of about 4000 ($\times 10^{-6}$). When enriched in ^{57}Fe, it displayed a single absorption line at 14.4-keV. Relatively recently, it had been shown[17] how to communicate the large values of magnetization characteristic of ferromagnetic materials into thin foils of paramagnetic media, such as stainless at room temperature, by sandwiching it between ferromagnetic layers. Such an arrangement was used in the experiments reported here to launch a wave of oscillating magnetization into a stainless tape, enriched in ^{57}Fe so that nuclear phase modulation might be observed at a distance from the source of the disturbance that was greater than the range for the transport of acoustic phonons.

This experiment employed a conventional Mössbauer spectrometer with a 2mCi ^{57}Co source in a Pd matrix to obtain the ^{57}Fe resonance spectra in a transmission geometry. To detect the 14.4-keV gamma rays we used a high resolution EG&G high purity Ge detector. A Wavetek Model 3000 signal generator and a 50-db ENI-325LA linear radiofrequency (rf) amplifier provided the oscillating magnetic field.

To calibrate the contributions from ultrasonic and phase modulation effects two independent techniques of sideband generation were used. As

99

a basis for comparison, ultrasonic sidebands were excited on the unsplit absorption line of ^{57}Fe nuclei in a stainless steel foil by sinusodial vibrations injected with two different 25-MHz piezoelectric transducers. One was X-cut so that initial vibrations were launched into the stainless with displacements normal to the face of the transducer as shown in Fig. 1a. The other was AT-cut so that initial displacements were excited in the plane of the face of the transducer as shown in Fig. 1b.

As shown in Figs. 1a and 1b an 8 mm × 10 mm section of a larger ^{57}Fe-enriched stainless steel foil of 2.5-μm thickness was acoustically bonded to each of the transducers used in this experiment. The remaining length of the 10 mm × 20 mm stainless foil was gently curved, forming a 90 degree angle with the plane of the transducer. Mechanical support was provided for the transverse section of foil by mounting it between glass cover slides which were then fastened to the transducer cell.
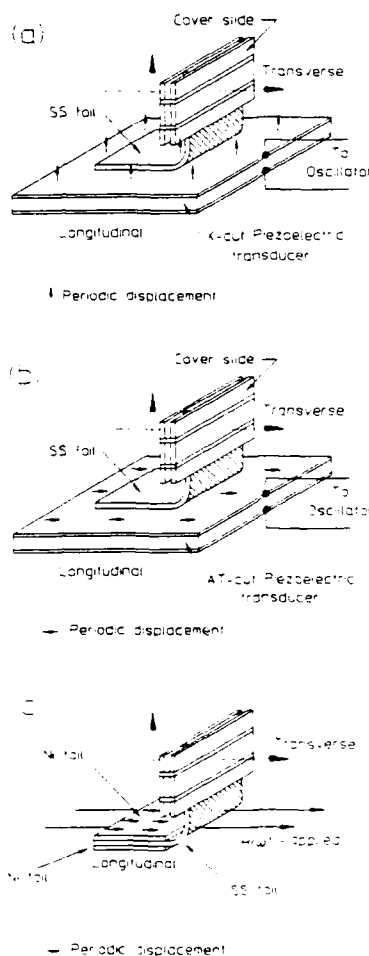
Figure 1. Schematic representation of the mounting arrangements used in the excitation of sidebands on the Mössbauer absorption line of ^{57}Fe in the 2.5 μm thick stainless steel (ss) foil shown as shaded. The optical path from gamma source to detector is shown by the dotted arrow for the orthogonal directions marked as longitudinal and transverse. Excitation is injected into the horizontal face of the ss-foil and the vertical face is mechanically stabilized by the 100 μm thick glass cover slides sandwiching the absorber foil.

a) Vibrational excitation injected by the X-cut quartz crystal transducer connected to a radiofrequency oscillator.

b) Vibrational excitation injected by the AT-cut crystal transducer connected to a radiofrequency oscillator.

c) Spin waves injected by the periodic oscillation of the Ni foils pressed onto the absorber foil by additional cover slides not shown and excited by the magnetic field in an inductor containing the Ni foils. The vertical section protrudes from the coil between windings.

101

In the usual longitudinal geometry for a transmission experiment, a convenient level of input power of 0.06 W to the X-cut crystal produced the reference level of sideband development seen in Fig. 2 in which the 4th order contained 34% of the intensity remaining in the parent transition. In the transverse geometry, the effect of phonons transported in the foil about 1 cm around a bend of 90 degrees could not be detected even with a tenfold increase in power above the reference level. Such an absence of phonons seems consistent with the difficulties expected in propagating transverse vibrations through a medium thin in comparison to a wavelength of sound. This experiment was performed with both X- and AT-cut quartz crystals for transducers as shown in Figs. 1a and 1b. Sidebands were not observed in the transverse geometry in either case and the AT-cut transducer required a larger input power of 2.9 W in the longitudinal geometry in order to obtain the same reference level of sideband development.

In the second experimental arrangement, the piezoelectric transducer was replaced with a pair of 2.5 μm foils of ferromagnetic Ni (8 mm × 10 mm) which were periodically magnetized as shown in Fig. 1c. The foils (Ni-SS-Ni) were held in rigid contact by sandwiching them between glass cover slides. The protruding section of the stainless foil was again bent at an angle of 90 degrees and enclosed between glass cover slides in the same way as before. Mechanical rigidity was provided to the absorber assembly by a plastic frame.

An rf magnetic field of 0.07 mT was applied to the absorber via a flattened induction coil of a tuned L-C circuit. For observation in the longitudinal geometry the rf power level was adjusted to give about the same reference level of sideband development as had been generated with the piezoelectric transducer, thus facilitating a direct comparison of the propagation of ultrasonic sidebands with those induced by phase modulations generated by magnetostatic waves.
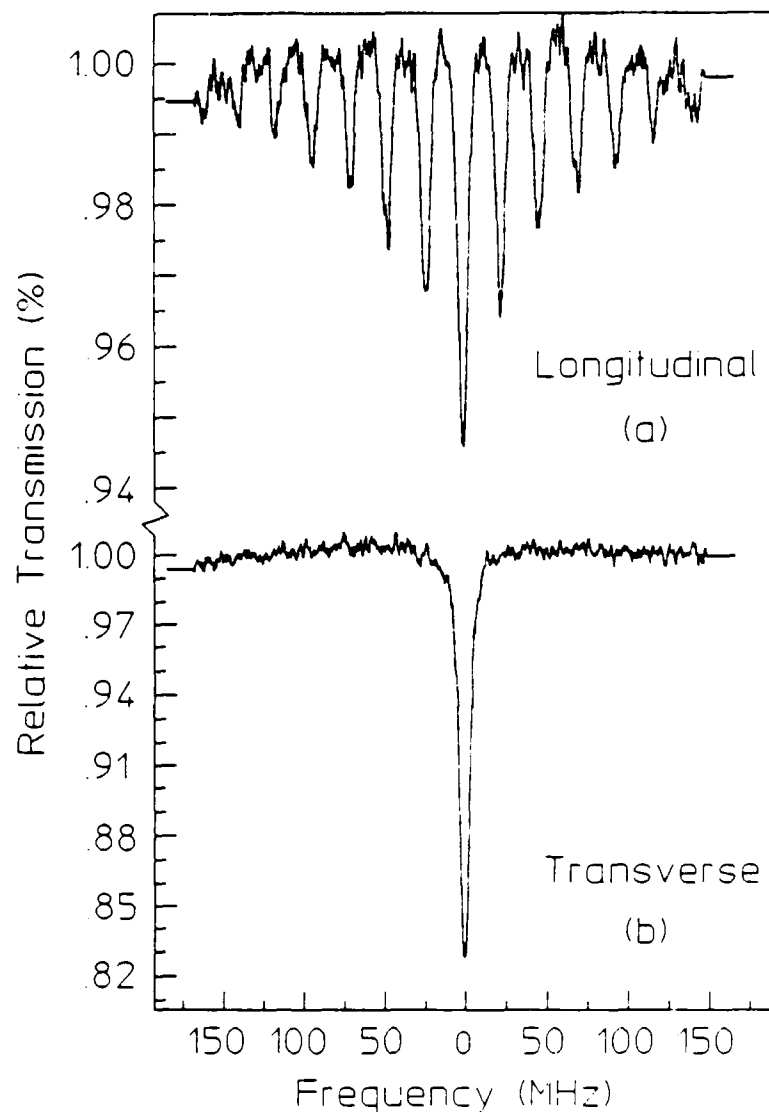
102

Figure 2: Absorption spectra of ^{57}Fe in stainless showing sidebands developed by phonons present in the sample foil.
a) reference spectrum observed in the longitudinal geometry at a level of excitation of 0.06 Ẅ in the piezoelectric crystal.
b) Spectrum observed in the transverse geometry of Fig. 1a for an excitation level of 0.7 Ẅ. Only the unsplit parent line is seen.

103

The spectra obtained in the longitudinal and transverse geometries of Fig. 1c are shown in Fig. 3. In the transverse geometry at this same level of input power, first order sidebands containing about 22 percent of the intensity of the parent line developed. This represents a level 10 times the threshold for detection and hence 100 times any component contributed by acoustic phonons as determined from the data of Fig. 2 obtained with the experimental arrangement of Fig. 1a. It seems that these experiments have shown that an oscillating alignment of spins can be propagated through such a stainless foil better than mechanical vibrations can be transported under the same conditions.

Excited on one end by the oscillating magnetization of a strip of ferromagnetic Ni, the absorber foil showed the strong development of sidebands at the other end where mechanical vibrations were shown to contribute less than 1% of the signal. In these experiments the driving amplitude H_o in the Ni was only 0.07 mT while the frequency was 23.74 MHz. Without the excitation of spin waves the effect should have been smaller by at least the ratios of the scaling parameters, $(B_o/\omega)^2$, a factor of 10^{11} for this case. Even with some attenuation of the spin waves during transport, the great enhancement in the effects of coherent modulation which they produced in this arrangement makes possible the examination of many predicted coherent phenomena over practical ranges of tuning at accessible levels of input powers.
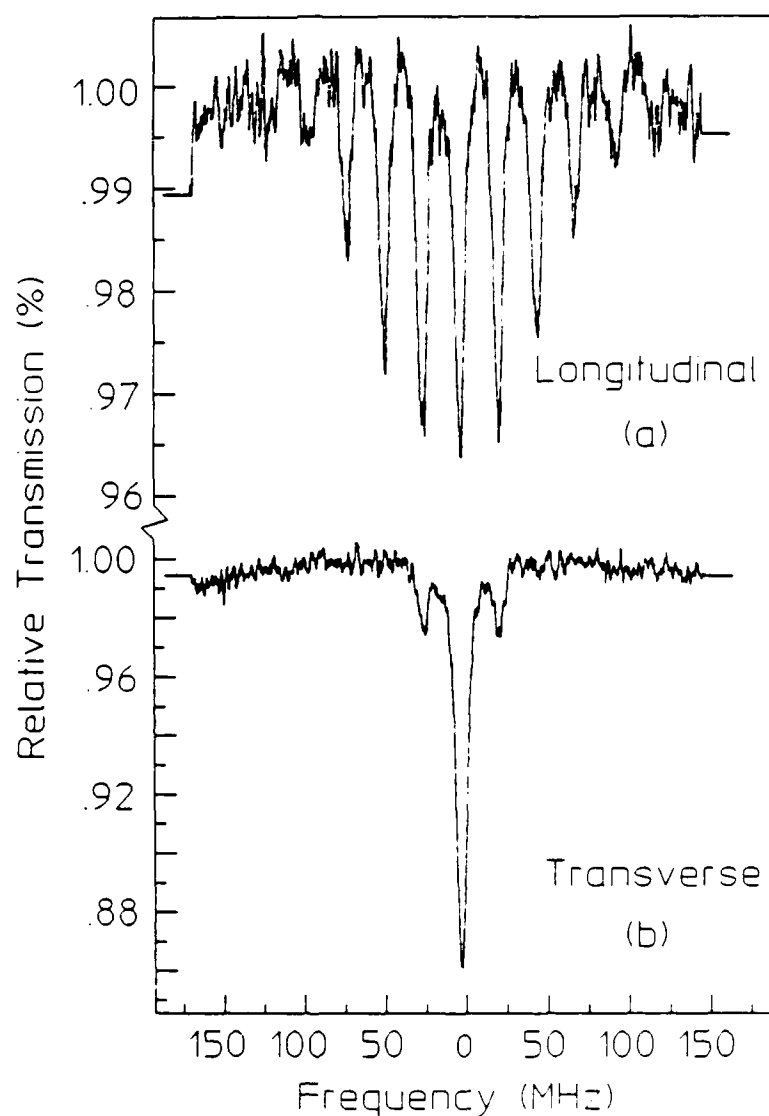
Figure 3: Absorption spectra of ^{57}Fe in stainless showing sidebands resulting from the modulation of nuclear phases by spin waves present in the sample foil.
a) Reference level of excitation observed in the longitudinal geometry of Fig. 1b at a field amplitude of 0.07 mT.
b) Sidebands observed in the transverse geometry for the same driving field of 0.07 mT.

References

1. E. Ikonen, P. Helisto, J. Hietaniemi and T. Katila, Phys. Rev. Lett. 60, 643 (1988).

2. P. Helisto, E. Ikonen, T. Katila and K. Riski, Phys. Rev. Lett. 49, 1209 (1982).

3. E. Ikonen, P. Helisto, T. Katila and K. Riski, Phys. Rev. A 32, 2298 (1985).

4. A. V. Mitin, Sov. Phys. JETP. 25, 1062 (1967).

5. P. J. West and E. Matthias, Z. Phys. A 228, 369 (1978).

6. S. Olariu, I. Popescu and C. B. Collins, Phys. Rev. C 23, 1007 (1981).

7. C. B. Collins and B. D. DePaola, Optics Lett. 10, 25 (1985).

8. B. D. DePaola and C. B. Collins, J. Opt. Soc. Am. B1, 812 (1984).

9. B. D. DePaloa, S. S. Wagal, and C. B. Collins, J. Opt. Soc. Am. B2, 541 (1985).

10. T. H. O'Dell, Ferromagnetodynamics (J. Wiley, N.Y., 1981) Ch. 2.

11. C. Kittel, Phys. Rev. 110, 836 (1958).

12. P. C. Fletcher and C. Kittel, Phys. Rev. 120, 2004 (1960).

13. E. Schlömann, J. Appl. Phys. 31, 1647 (1960).

14. R. W. Damon and J. R. Eshback, J. Appl. Phys. Supp. 31, 1045 (1960).

15. H. A. Mook, J. W. Lynn, and R. M. Nicklow, Phys. Rev. Lett. 30, 556 (1973).

16. T. Lyman, Metals Handbook, 8th ed. (Am. Soc. for Metals, Ohio, 1961), Vol. I, p. 793.

17. P. Grünberg, J. Appl. Phys. 51, 4338 (1980).

MAJOR MILESTONE REPORT

Strengthening the Feasibility of the Tuning
and Stimulation of Nuclear Radiation

June 1, 1988

C. B. Collins, Center for Quantum Electronics, University of Texas at Dallas

Achievement

Tunable sidebands have been produced on gamma-ray transitions by directly modulating the phases of nuclear states at levels far exceeding any noise contributed by magnetoacoustic effects.

Technical Background

The approach to the gamma-ray laser with the greatest potential efficiency depends upon the mixing of nearly resonant nuclear states with interaction energies developed by the external modulation of the hyperfine fields. In this way stored isomeric populations could be dumped into freely radiating states.

The first milestone would be a demonstration that significant interaction energies can be developed at the nuclear level by externally applied fields. Overseas efforts have shown that a magnetic field oscillating at radiofrequencies can directly modulate the phase of a nuclear state by coupling to its magnetic moment. In the frequency domain such modulation is observed as sidebands on gamma-ray transitions originating on the state, but the effect is very small at all reasonable levels of applied power.

The conceptual key to thousandfold enhancements lies in the use of small fields to manipulate the greater magnetic fields arising from the natural correlations of individual magnons in ferromagnetic materials. For several years we have observed the production of sidebands to Mössbauer transitions on such a large scale in ferromagnetic materials, but the concern has lingered that the dominant effect might have actually arisen from periodic Doppler shifts produced by vibrations in the host lattice driven by magnetostriction.

Report

As a basis for comparison, sidebands were excited on the unsplit absorption transition of ^{57}Fe nuclei at 14.4 keV in a stainless steel foil by sinusoidal vibrations injected with a piezoelectric source as shown in Fig. 1a. In the usual longitudinal geometry for a transmission experiment a convenient level of input power produced a reference level of sideband development in which the 4th order contained 20% of the intensity remaining in the parent line. In the transverse geometry the effect of phonons transported in the foil about 1 cm around a bend of 90 degrees could not be detected, even with a tenfold increase in power above the reference level.
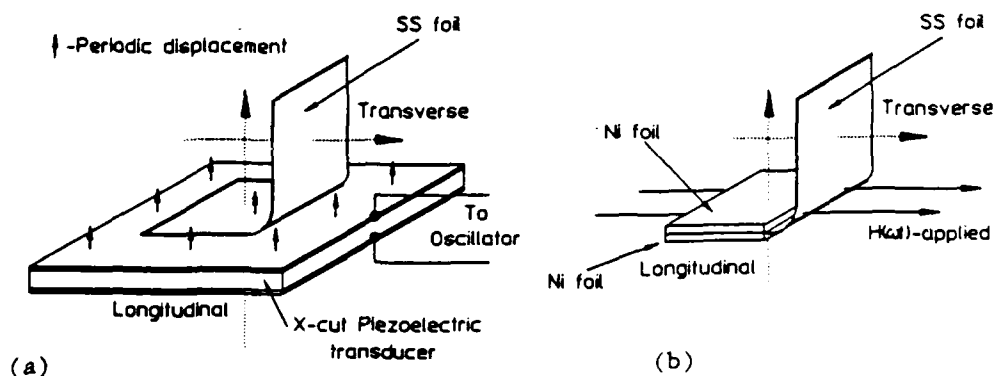
Figure 1: Schematic representation of the mounting of the enriched stainless steel foil 2.5 μm thick used in these transmission experiments. The vectors of the propagation of the gammas from sources to detectors are shown by the dotted arrows for the longitudinal and transverse arrangements shown.
a) (left) Sidebands driven by phonons from an X-cut quartz crystal.
b) (right) Sidebands driven by the oscillating magnetization of the two Ni foils immersed in the applied H field shown.

Replacing the piezoelectric source with a pair of 2.5 μm foils of ferromagnetic Ni sinusoidally magnetized as shown in Fig. 1b, gave the opportunity to launch what we believe are large amplitude spin waves into the magnon fluid in the paramagnetic stainless foil. Boundary effects known as flux refractions favor the transfer of ferromagnetic magnetization of the Ni across the interface where it can serve as a source term for local alignment of the magnons in the stainless foil. The longitudinal geometry was used to set the same reference level of sideband development at the source. In the transverse geometry at this same level of input power, the first order sidebands were found to have 20% of the intensity of the parent line, a level 10 times the threshold for detection and hence, 100 times any component contributed by acoustic phonons.

Significance

There is a twofold significance to this major milestone experiment.

1) In stainless steel spin waves can be transported more efficiently than phonons, thus providing a means for studying the direct modulation of nuclear states in an environment free from acoustic noise.

2) Even with transport the intensities of magnetic sidebands are greatly enhanced by ferromagnetic sources meaning that relatively large interaction energies can be developed at the nuclear level with modest applied powers.

108

ACKNOWLEDGEMENT